

On the Extended Finite Element Method for the Elasto-Plastic Deformation of Heterogeneous Materials

vom Fachbereich Maschinenbau und Verfahrenstechnik
der Technischen Universität Kaiserslautern
zur Verleihung des akademischen Grades
Doktor-Ingenieur (Dr.-Ing.)
genehmigte Dissertation

von
Herrn
M.Sc. Tobias Zangmeister
aus Seeheim-Jugenheim

Hauptreferent: Prof. Dr.-Ing. Ralf Müller
Korreferenten: Priv.-Doz. Dr. Heiko Andrä
Prof. Dr.-Ing. Stefan Diebels
Vorsitzender: Prof. Dr.-Ing. Eberhard Kerscher
Dekan: Prof. Dr.-Ing. Christian Schindler

Tag der Einreichung: 28.04.2014
Tag der mündlichen Prüfung: 01.12.2014

Kaiserslautern, 2015

Herausgeber

Lehrstuhl für Technische Mechanik
Technische Universität Kaiserslautern
Gottlieb-Daimler-Straße
Postfach 3049
67653 Kaiserslautern

© Tobias Zangmeister

Ich danke der „Prof. Dr. Hans Georg und Liselotte Hahn Stiftung“ für die finanzielle Unterstützung bei der Drucklegung.

Druck

Technische Universität Kaiserslautern
ZTB – Abteilung Foto-Repro-Druck

Alle Rechte vorbehalten, auch das des auszugsweisen Nachdrucks, der auszugsweisen oder vollständigen Wiedergabe (Photographie, Mikroskopie), der Speicherung in Datenverarbeitungsanlagen und das der Übersetzung.

ISBN 978-3-942695-08-4

Abstract

In the context of simulating the micromechanical behavior of multi-phased heterogeneous materials the finite element method (FEM) is a standard discretization method (cf. [Hughes, 1987]). The extended finite element method (XFEM, introduced by [Belytschko and Black, 1999] and [Moës et al., 1999], cf. [Fries and Belytschko, 2010]) enriches the polynomial approximation space of the FEM in order to model discontinuities within the solution at the cost of additional degrees of freedom. The major advantage of XFEM over FEM is the possibility to model non-smooth solutions independent from the underlying finite element mesh (cf. [Fries and Belytschko, 2010]).

The focus of this work lies on analyses of the numerical properties of the two methods. A detailed error analysis for FEM in comparison to XFEM is presented in section 4.3, where a classical ESHELBY problem is considered (cf. [Eshelby, 1957]) with an infinitely extended material that has a single spherical inclusion.

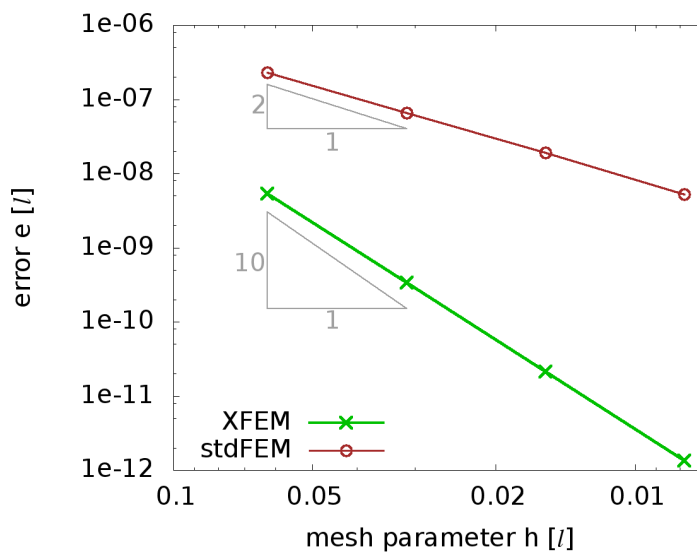


Figure 1: Error in displacement for different mesh discretizations.

In Fig. 1 a log-log-plot of the error of the two methods over mesh parameter h introduced in 4.53 can be seen. It strikes that the total error with XFEM on the coarsest grid with mesh parameter h_1 is only slightly larger than the total error in the standard FEM on the finest grid analyzed. The numerical convergence rate of the XFEM is drastically better than for standard FEM,

as well. The order of convergence for the standard FEM is quadratic whereas the XFEM converges significantly faster.

From a multitude of fields of applications of the XFEM, this work restricts itself to the simulation of the elasto-plastic deformation of heterogeneous materials. In this context, a commonly known problem of the XFEM are nodal level set values close to zero (cf. [Fries and Belytschko, 2010]) which results in almost linear dependence of the approximation space spanned by the basis functions in the extended approximations (see section 3.2). Surprisingly, no publications are available that are analyzing the exact influence of a nodal level set value close to zero on the condition of the problem.

A one-dimensional example is used in this work to analyze the dependence of the problem condition of the minimal distance between a node and the interface. It is discovered that the problem becomes ill-posed with quadratic order depending on parameter \hat{h} describing the minimal distance between a node and the interface.

A trivial three-dimensional problem of specific example situations is analyzed in detail as well and the results strongly suggest the same quadratic relation of the ill-posedness depending on parameter \hat{h} .

Based on this finding, the existing methods of stabilizing the XFEM are re-evaluated and a novel stabilization algorithm is created. It combines a shifting of nodes that are close to the interface away from the same with mesh regularization techniques.

Table 1 depicts the influence of this algorithm on the condition of a trivial three-dimensional example of the deformation of a layered material (cf. section 4.4.1 for the details of this example).

| \hat{h} | κ without mesh optimization | κ with mesh optimization |
|-----------|------------------------------------|---------------------------------|
| 0.55 | $9.43 \cdot 10^4$ | $7.94 \cdot 10^4$ |
| 0.505 | $1.64 \cdot 10^6$ | $9.80 \cdot 10^4$ |
| 0.5005 | $1.57 \cdot 10^8$ | $1.34 \cdot 10^5$ |

Table 1: Condition κ of the global stiffness matrix for different parameters \hat{h} with and without mesh optimization.

It strikes that for the original meshes, the condition numbers differ by two magnitudes each. In contrast to that, in all three examples with mesh optimization, the magnitude of the condition of the global stiffness matrix is more or less equal to the one of the original mesh with parameter $\hat{h} = 0.05$. It is emphasized that $\hat{h} = 0.05$ describes the best possible situation for XFEM when not preprocessing the mesh in this specific example.

Obviously, other stabilization methods are able to produce similar results, but the mesh optimization algorithm has a major advantage over traditional methods for stabilizing the XFEM:

The algorithm is able to reduce unphysical stress peaks as well as stress oscillations in the region of material interfaces.

In section 4.4.2 the example of a spherical inclusion is analyzed in detail. Unsurprisingly, the maximal occurring values of the VON MISES equivalent stress values σ_v^{\max} depend on the mesh discretization. A finer mesh reduces unphysical stress peaks as the discretization error is reduced. When applying the mesh optimization algorithm first, the stress peaks are reduced as well, as Table 2 shows.

| mesh discretization | σ_v^{\max} original | σ_v^{\max} optimized mesh | red. factor |
|--------------------------------|----------------------------|----------------------------------|-------------|
| $10 \times 10 \times 10$ voxel | 0.935 MPa | 0.763 MPa | 81.64% |
| $16 \times 16 \times 16$ voxel | 0.835 MPa | 0.763 MPa | 91.38% |
| $32 \times 32 \times 32$ voxel | 0.683 MPa | 0.624 MPa | 91.31% |
| $64 \times 64 \times 64$ voxel | 0.527 MPa | 0.510 MPa | 96.63% |

Table 2: Reduction of stress peaks with mesh optimization algorithm 4.2.

Summarizing the different discretization examples, it strikes that the node moving algorithm has the potential to reduce unphysical stress peaks significantly, especially when the underlying finite element discretization is done on a coarse mesh. For finer grids the potential of reducing stress peaks is not as good, due to fact that for finer discretizations the stress peaks are already naturally reduced in the original mesh.

It is emphasized that for the remeshed results presented here, different parameter sets for the node moving algorithm 4.2 have been used. In some rare cases some combinations of algorithmic parameters even lead to an increased maximal VON MISES equivalent stress in the mesh, even though the total amount of elements with a large stress value had been reduced. Overall, it becomes obvious that more research in the fine tuning of the algorithm seems worthwhile. Nevertheless, a good potential of the algorithm in reducing unphysical stress peaks has been demonstrated even though it has been specifically designed for a reduction of the condition of the global stiffness matrix without introducing additional geometrical errors.

As an example application for the XFEM, adhesive joints in concrete are analyzed. The advantage of the XFEM being able to analyze geometries independent of the underlying finite element mesh is demonstrated in detail.

This is done by carrying out a parameter study concerning the joint geometry without having to adopt the underlying mesh.

Furthermore, this work presents a complex framework for simulating mechanical properties of the metal matrix composite AMC225xe. First, a statistically validated stochastic XFEM model for the particle geometry is created. Second, the material parameters of the model are fitted with a huge parameter study according to experimental uniaxial loading tests. Combining the results of the geometry model with the solution of the inverse problem of finding correct material parameters, a ready to use framework is created for analyzing the metal matrix composite in further detail.

Kurzfassung

Im Kontext der Simulation von mikromechanischen Eigenschaften von mehrphasigen heterogenen Materialien hat sich in den letzten Jahrzehnten die Finite-Elemente-Methode (FEM) als eine Standarddiskretisierungsmethode etabliert (siehe [Hughes, 1987]). Die erweiterte Finite-Elemente-Methode (XFEM, erstmals in [Belytschko and Black, 1999] und [Moës et al., 1999], siehe auch [Fries and Belytschko, 2010]) reichert den polynomialen Approximationsraum der FEM mit zusätzlichen Freiheitsgraden an, um Diskontinuitäten in der Lösung unabhängig des zu Grunde liegenden Netzes modellieren zu können.

Der Schwerpunkt dieser Arbeit liegt bei einer Analyse der numerischen Eigenschaften der XFEM. Eine detaillierte Fehleranalyse der Simulationsergebnisse von FEM im Vergleich zu XFEM bei einem klassischen ESHELBY-Problem eines kugelförmigen Einschlusses in einer unendlich ausgedehnten Matrix (siehe [Eshelby, 1957]) wird in Kapitel 4.3 präsentiert.

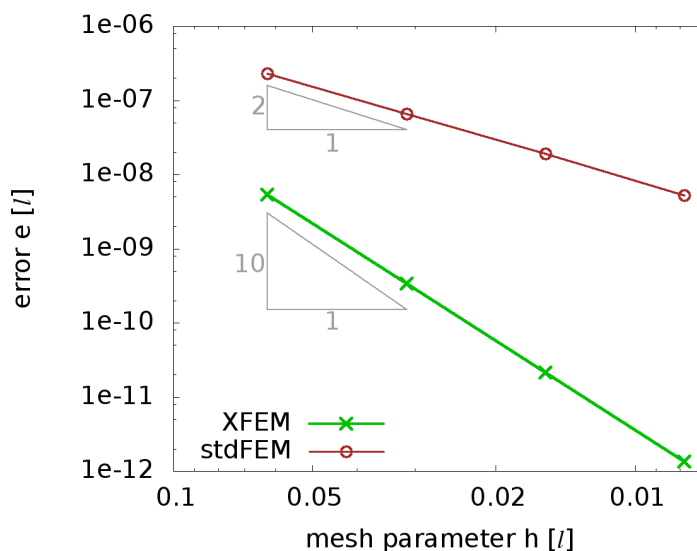


Figure 2: Fehler im Verschiebungsfeld in Abhängigkeit der zu Grunde liegenden Netzfeinheit.

In Bild 2 ist der doppelt-logarithmische Graph des L_2 -Fehlers des Verschiebungsfeldes in Abhängigkeit des Netzparameters h (eingeführt in 4.53) zu sehen. Es fällt auf, dass der Fehler bei XFEM generell signifikant kleiner ist als bei FEM. Selbst bei einer sehr groben Vernetzung ist der XFEM-

Fehler in etwa genau so groß wie der FEM-Fehler auf der feinsten Vernetzung, die in der Untersuchung analysiert wurde. Ebenfalls auffällig ist, dass die Konvergenzordnung bei FEM quadratisch ist und XFEM in diesem Beispiel signifikant schneller konvergiert.

Die XFEM hat eine Vielzahl von Anwendungsgebieten. Diese Arbeit beschränkt sich auf die Berechnung von elasto-plastischen Verformungen von heterogenen Materialien. Ein in diesem Kontext bekanntes Problem der XFEM sind Knoten-Levelset-Werte nahe Null in dem zu Grunde liegenden Netz, denn diese führen zu fast linearen Abhängigkeiten der Basisfunktionen des XFEM Lösungsraums (siehe Kapitel 3.2 und [Fries and Belytschko, 2010]) und somit zu einem linearen System mit fast singulärer Matrix. Überraschenderweise hat selbst eine umfangreiche Literaturstudie keine wissenschaftliche Publikation zu Tage gefördert, die den genauen Zusammenhang zwischen den auftretenden Knoten-Levelset-Werten nahe Null und der Kondition des Problems analysiert.

Ein eindimensionales Beispiel wird in dieser Arbeit genutzt, um den Zusammenhang zwischen dem Netzparameter \hat{h} , der den am nächsten an Null gelegenen Knoten-Levelset-Wert beschreibt, sowie der Kondition der globalen Steifigkeitsmatrix im Detail zu analysieren. Es ergibt sich, dass eine reziproke Proportionalität zwischen der Kondition des Problems und dem Quadrat des Parameters \hat{h} vorliegt.

Eine detaillierte Analyse eines trivialen dreidimensionalen Beispiels legt nahe, dass der gleiche Zusammenhang vorliegt. Die Kondition des Problems ist auch bei dreidimensionalen Netzen umgekehrt proportional zu \hat{h}^2 ist.

Basierend auf diesen Feststellungen reevaluiert diese Arbeit die bestehenden XFEM-Stabilisierungstechniken und stellt einen neuen Stabilisierungsalgorithmus vor. Dieser verbindet Knotenverschiebungen von Knoten, deren Levelset-Wert nahe Null ist, mit einem Netzregularisierungsalgorithmus. Tabelle 3 zeigt den Einfluss des Netzoptimierungsalgorithmus auf die Kondition eines trivialen dreidimensionalen Problems, bei dem ein geschichtetes Material uniaxial gedehnt wird (siehe Kapitel 4.4.1 bzgl. der Details dieses Beispiels).

Es ist auffällig, dass bei dem Originalnetz die Konditionen des Problems sich jeweils um zwei Größenordnungen unterscheiden. Im Gegensatz hierzu ist die Kondition bei den optimierten Netzen in allen drei Fällen nahezu gleich und zwar von der Größenordnung wie im Originalnetz bei Parameter $\hat{h} = 0.05$. Dies ist bei diesem Beispiel der bestmögliche Fall für XFEM, da das Beispiel so konstruiert ist, dass bei $\hat{h} = 0.05$ das Interface exakt in der Mitte zwischen zwei Schichten von Knoten liegt und dass es somit nicht möglich ist, bei dem vorgegebenen Netz ein größeres \hat{h} zu erhalten.

Offensichtlich sind auch andere XFEM Stabilisierungstechniken in der Lage,

| \hat{h} | κ ohne Netzoptimierung | κ mit Netzoptimierung |
|-----------|-------------------------------|------------------------------|
| 0.55 | $9.43 \cdot 10^4$ | $7.94 \cdot 10^4$ |
| 0.505 | $1.64 \cdot 10^6$ | $9.80 \cdot 10^4$ |
| 0.5005 | $1.57 \cdot 10^8$ | $1.34 \cdot 10^5$ |

Table 3: Kondition κ der globalen Steifigkeitsmatrix für verschiedene Parameter \hat{h} einmal mit und einmal ohne Netzoptimierungsalgorithmus.

ähnliche Ergebnisse zu erzielen, jedoch bietet dieser neue Algorithmus einen entscheidenden Vorteil:

Der Algorithmus ist in der Lage, nicht physikalische Spannungsspitzen sowie Spannungssoszillationen in der Nähe der Materialgrenzen zu reduzieren.

In Kapitel 4.4.2 wird das dreidimensionale Beispiel eines kugelförmigen Einschlusses im Detail analysiert. Erwartungsgemäß hängt der maximal auftretende Wert der VON-MISES-Vergleichsspannung σ_v^{\max} von der Netzdiskretisierung ab. Je feiner das Netz, desto niedriger ist der Wert von σ_v^{\max} . Wie bereits angedeutet, ist jedoch auch der Netzoptimierungsalgorithmus in der Lage, bei gleich bleibender Netzfeinheit σ_v^{\max} zu reduzieren, wie auch in Tabelle 4 zu sehen ist.

| Netzfeinheit | σ_v^{\max} orig. | σ_v^{\max} optimiertes Netz | red. Faktor |
|--------------------------------|-------------------------|------------------------------------|-------------|
| $10 \times 10 \times 10$ Voxel | 0.935 MPa | 0.763 MPa | 81.64% |
| $16 \times 16 \times 16$ Voxel | 0.835 MPa | 0.763 MPa | 91.38% |
| $32 \times 32 \times 32$ Voxel | 0.683 MPa | 0.624 MPa | 91.31% |
| $64 \times 64 \times 64$ Voxel | 0.527 MPa | 0.510 MPa | 96.63% |

Table 4: Reduktion nicht physikalischer Spannungsspitzen durch den Netzoptimierungsalgorithmus 4.2.

Zusammenfassend fällt auf, dass der Netzoptimierungsalgorithmus in allen präsentierten Beispielen die nicht physikalischen Spannungsspitzen reduzieren kann. Insbesondere bei groben Vernetzungen ist dies der Fall. Bei feineren Vernetzungen ist durch die eingangs erwähnte bessere Ausgangssituation das Verbesserungspotential des Algorithmus reduziert.

Es ist an dieser Stelle wichtig zu betonen, dass bei den hier vorgestellten Ergebnissen die Parameter des Netzoptimierungsalgorithmus leicht variieren. Obwohl der Algorithmus für alle analysierten Parameterkombinationen Spannungsspitzen generell reduziert hat, ist in einigen wenigen Fällen der maxi-

male Wert sogar größer gewesen als der ursprüngliche Wert von σ_v^{\max} . Offensichtlich ist eine tiefer gehende Analyse der Steuerparameter des Algorithmus wünschenswert. Nichtsdestotrotz zeigt der Algorithmus sein Potential darin, nicht physikalische Spannungsspitzen zu reduzieren, obwohl er ursprünglich speziell für die Stabilisierung der Kondition der Steifigkeitsmatrix geschaffen wurde.

Als ein Anwendungsbeispiel für die XFEM werden in dieser Arbeit Klebefugen zwischen Hochleistungsbetonplatten untersucht. Der Vorteil der XFEM gegenüber der FEM, dass Geometrien unabhängig von der zugrunde liegenden Vernetzung analysiert werden können, kommt hier voll zum Tragen. In einer Geometrieparameterstudie wird die Fugengeometrie hinsichtlich einer uniaxialen Zugbelastung optimiert, ohne für die einzelnen Simulationen die Vernetzung anpassen zu müssen.

Zusätzlich wird in dieser Arbeit ein komplexes Simulationsframework vorgestellt, mit dem die mechanischen Eigenschaften des Metallmatrix-Komposits AMC225xe simuliert werden können. Hierzu wird zunächst ein statistisch validiertes XFEM Partikelgeometriemodell erzeugt. Des Weiteren werden in einer Parameterstudie die Materialparameter an experimentelle Belastungsdaten angepasst. Durch die Kombination des geometrischen Modells mit dem Ergebnis des inversen Problems die Materialparameter an experimentelle Daten anzupassen, ist eine Möglichkeit zur weitergehenden Analyse des Metallmatrix-Komposits geschaffen.

Contents

| | | |
|----------|--|-----------|
| 1 | Introduction | 1 |
| 1.1 | Motivation | 1 |
| 1.2 | State of the art | 2 |
| 1.3 | Outline | 3 |
| 2 | Governing equations | 5 |
| 2.1 | Kinematic relations | 5 |
| 2.1.1 | Deformation gradient | 7 |
| 2.1.2 | Strain measure | 8 |
| 2.2 | Material law | 10 |
| 2.2.1 | Isotropic linear elasticity | 10 |
| 2.2.2 | Linear elasticity with thermal strains | 11 |
| 2.2.3 | Elastoplasticity model | 12 |
| 2.2.4 | Elastoplasticity model with thermal strains | 14 |
| 2.3 | Discontinuities | 15 |
| 2.3.1 | Description of discontinuities | 15 |
| 2.3.2 | Level sets: Implicit functions | 16 |
| 2.3.3 | Level sets: Signed distance functions | 18 |
| 2.4 | Balance equations | 19 |
| 2.4.1 | Conservation of mass | 19 |
| 2.4.2 | Balance of momentum | 20 |
| 2.5 | Initial boundary value problem | 21 |
| 2.6 | Weak formulation of the BVP | 23 |
| 3 | The finite element discretization | 25 |
| 3.1 | Discretization of the weak forms | 25 |
| 3.2 | Discretization with the XFEM | 30 |
| 4 | Numerical behavior and properties | 39 |
| 4.1 | One-dimensional model problem | 39 |
| 4.1.1 | Exact XFEM element for the model problem | 40 |
| 4.1.2 | Eigenvalue analysis | 46 |
| 4.2 | Eigenvalue analysis for XFEM in 3D | 51 |
| 4.3 | Comparison XFEM vs FEM - spherical inclusion | 58 |
| 4.3.1 | Analytical solution | 58 |
| 4.3.2 | Simulation results | 62 |
| 4.4 | Stabilizing ill-conditioned XFEM problems | 68 |
| 4.4.1 | Mesh optimization for enhancing XFEM | 72 |

| | | |
|----------|--|------------|
| 4.4.2 | Reducing non-physical stress peaks | 78 |
| 5 | Applications | 87 |
| 5.1 | Adhesive joints in concrete | 87 |
| 5.2 | Metal matrix composite AMC225xe | 92 |
| 5.2.1 | Geometric microstructure model | 92 |
| 5.2.2 | Experimental data | 94 |
| 5.2.3 | Parameter study - solving the inverse problem | 96 |
| 5.2.4 | Simulation on complex microstructure | 100 |
| 6 | Conclusions | 103 |
| 6.1 | Future work | 104 |
| A | Appendix | 107 |
| A.1 | Higher order terms in XFEM approximation | 107 |
| A.2 | Function spaces | 112 |
| A.3 | Continuum mechanical trivia | 114 |
| A.3.1 | Contraction of tensors | 114 |
| A.3.2 | Rigid body motion | 114 |
| A.3.3 | Derivative of the norm of stress tensor deviator | 115 |
| A.3.4 | Derivation of the weak formulation of the BVP | 115 |
| A.4 | Parameters used for mesh smoothing | 117 |
| | List of Symbols | 119 |

Chapter 1

Introduction

1.1 Motivation

Compounds of multiple materials have found a large propagation in the last decades. These materials are typically superior to single-phased materials in terms of the specifications of the application at hand. For example, metal matrix composites (MMC), where typically ceramic particles are mixed into a metal matrix, usually have a significantly higher strength to weight ratio than any pure metal (cf. [Chawla and Chawla, 2004]).

In order to understand the macroscopic behavior of such composites, the material's behavior on the microscopic level has to be understood first, as many macroscopic effects like material failure emerge from the microscopic scale. It is a well-known fact (cf. for example [Sato et al., 1991] and [Hoffmann, 2012]) that these effects typically begin at the interface of the different materials within the composite, as often stress concentrations appear close to material interfaces and cause the nonlinear effects like damage or plastic yielding. Therefore, a precise knowledge of the occurring stresses at interfaces is desirable when modeling the material behavior on the microscopic scale. Analytical solutions of such bimaterial problems are only possible for trivial geometries (cf. [Eshelby, 1957]). Hence, numerical approximation schemes are required for simulating the material behavior.

However, the jumps in material parameters at these interfaces lead to non-smooth solutions (i.e. kinks in the displacements and jumps in the stresses and strains), which reduce the accuracy of standard discretization methods including the finite element method (FEM). The discretization error of the FEM depends, roughly speaking, on both the approximation error of the finite element shape functions and the numerical quadrature error (cf. [Hughes, 1987]). Usually, the latter depends mainly on deviations of the finite element boundaries from exact domain boundaries, or on material interfaces because the domain of integration is only approximately captured (cf. [Guldberg et al., 1998]).

There are two principal possibilities of capturing non-smooth solutions when using FEM. The first is adopting the mesh accordingly. The isogeometric FEM or local mesh refinement reduces this part of the discretization error (cf. [Vuong and Simeon, 2012]). Nevertheless, in many applications with non-

smooth boundaries and material interfaces isogeometric finite elements or at least piecewise linear approximations of all boundaries and interfaces lead to an undesired work-intensive mesh generation. For these cases the extended finite element method (XFEM) (introduced by [Belytschko and Black, 1999] and [Moës et al., 1999], cf. [Fries and Belytschko, 2010]) is well-suited as it is able to include discontinuities into the finite element shape functions with the help of additional degrees of freedom. Therefore, XFEM allows to capture kinks in the unknown displacements and jumps in the derivatives of the unknowns within the interior of finite elements. There is no need of interface aligned meshes anymore, and advantages of regular meshes can be exploited. Immersed interface and immersed boundary methods belong to the same class of methods (cf. [Rutka et al., 2006]) but will not be discussed in this work.

1.2 State of the art

Derived from the partition of unity method (cf. [Babuska and Melenk, 1995]), the XFEM was first introduced by [Belytschko and Black, 1999] and [Moës et al., 1999]. In the last 15 years since then it has found a vast field of applications. It has, for example, been applied to inclusions in solids and holes in solids in [Sukumar et al., 2001]. The modeling of grain boundaries with the XFEM can be found in [Simone et al., 2006]. XFEM has been used in the field of solidification and phase transitions in [Chessa et al., 2002]. Also bio-mechanical applications of the XFEM can be found, for example in [Duddu et al., 2008]. It is also used for modeling virtual cuts with surgical simulators (c.f. [Vigneron et al., 2004]), two-phase flows (c.f. [Chessa and Belytschko, 2003]), two-phase flows with surface-tension (c.f. [Groß and Reusken, 2007]), fluid structure interactions (c.f. [Legay et al., 2006]) and degenerated structures in fluid structure interactions (c.f. [Zilian and Legay, 2008]). Nevertheless, the broadest spectrum of applications of the XFEM can be found in the context of cracks, dislocations and shear bands (cf. [Belytschko and Black, 1999, Moës et al., 1999, Sukumar et al., 2000, Stolarska et al., 2001] to name only a few).

This work restricts itself to bimaterial problems. In this context, a commonly known problem of the XFEM are nodal level set values close to zero (cf. [Fries and Belytschko, 2010]), which results in almost linear dependence of the approximation space spanned by the basis functions in the extended approximations (see section 3.2). Surprisingly, even an extensive literature study did not bring up a single publication analyzing the exact influence of a nodal level set value close to zero on the condition of the problem. Never-

theless there exist some strategies of tackling this problem of nearly singular stiffness matrices or even ill-posed problems. In [Béchet et al., 2005] a preconditioner is introduced that uses a local CHOLESKY based decomposition. It is able to improve the condition of the stiffness matrix if the problem is not ill-posed, that is, no nodal level set value is equal to zero. In [Menk and Bordas, 2011] a preconditioner is established that is based on the domain decomposition method FETI introduced in [Farhat and Roux, 1991]. The algorithm introduced by MENK uses CHOLESKY decompositions on decomposed domains together with additional continuity constraints. Numerical examples presented in [Menk, 2011] show that this preconditioner is able to reduce the condition of the stiffness matrix to a value close to the condition of a corresponding standard FEM stiffness matrix. To the author's knowledge this method has not yet been generalized to the three-dimensional case. Additionally, it has the drawback that it requires special solution algorithms. A recent work of LÖHNERT (cf. [Löhnert, 2014]) introduces a novel approach to handle this problem. In a preprocessing step, the physically meaningful zero eigenvalues of the local element stiffness matrices are computed. Physically meaningful in this context signifies the zero eigenmodes induced by the six rigid body eigenmodes and other specific boundary conditions. Elements that are barely intersected by an interface typically produce additional (numerically) zero eigenmodes. An orthogonal basis of the eigenvectors of these not physically meaningful zero eigenmodes is then used for stabilizing the element stiffness matrices. The results of this stabilization scheme are very promising in two dimensions as well as in three dimensions.

1.3 Outline

The field of application of this work is the stress analysis of microstructures of two-phase materials with high contrast in the material parameters between the phases, including nonlinear effects.

Chapter 2 defines the mathematical model of the considered bimaterial problems. In chapter 3 the FEM discretization is introduced. The XFEM discretization is also introduced in chapter 3.

The focus of this work lies on chapter 4 which analyzes the numerical behavior and properties of the XFEM. First, substantial analyses of the resulting eigenvalues for certain problem formulations are made and therewith the condition of the problem is analyzed in the one-dimensional case (cf. section 4.1) as well as in three-dimensional cases (cf. section 4.2). The well-known fact (cf. for example [Fries and Belytschko, 2010]) of the problem becoming ill-posed when nodal level set values are too close to zero is analyzed

in detail. New findings on the quantification of the ill-posedness of certain situations are presented in this work. Second, a detailed comparison of an error analysis of XFEM compared to FEM in a three-dimensional case is documented. Third, after presenting the state of the art of handling the previously mentioned unfavorable XFEM cases, a novel algorithm of circumventing this problem is created. It is shown that this developed algorithm is also capable of reducing unphysical stress peaks that typically occur when using the FEM or XFEM for solving bimaterial problems.

Chapter 5 presents some applications of the methodology. In section 5.1 an analysis of glue joints in concrete is presented where the advantages of the independence from the underlying mesh of XFEM compared to FEM becomes particularly evident. Section 5.2 presents a complex process chain that has been created in order to be able to simulate the macroscopic material behavior of a certain metal matrix composite (AMC225xe) that also makes use of the new findings of chapter 4. First, a stochastic model of the microstructure of the material is created and fitted to real-world data from electron micrographs. Then experimental data of uniaxial loading tests with the metal matrix composite is shown. Thereafter, the solution of the inverse problem of fitting the computer model to the experimental data on a simplified microstructure geometry is presented. Finally, an example computation using the previously obtained material parameters on a complex microstructure is presented.

Chapter 2

Governing equations

There exists a multitude of textbooks on the subject of classical continuum mechanics, for example [Gurtin, 1982], [Holzapfel, 2000] and [Wriggers, 2001]. For the sake of a consistent notation, the following recapitulation of continuum mechanical basic issues is based on [Wriggers, 2001] and [Han and Reddy, 2013].

2.1 Kinematic relations

This work is focused on analyses of microscopic behavior of macroscopic bodies. These macroscopic bodies are considered to consist of a material that is distributed continuously. That is, such a body occupies a region in the three-dimensional EUCLIDEAN space, denoted by \mathbb{R}^3 . Formally, the body then can be described as the set of all points in \mathbb{R}^3 that cover the body, hence it is a subset of \mathbb{R}^3 . Obviously, when considering motion and deformation of this body, the region varies in time as the body deforms. In order to keep track of such a motion or deformation it is convenient to locate any point of the body over time. This is done by locating its position vector $\mathbf{X} \in \mathbb{R}^3$ with respect to a previously chosen origin $\mathbf{0}$, at a given time t . Unless stated otherwise it is assumed from now on that at reference time $t = 0$ the body is undeformed and unstressed. At this reference time, the region occupied by the body is denoted by Ω and is called reference configuration, see Fig. 2.1. It is assumed that Ω is a LIPSCHITZ domain (cf. [Han and Reddy, 2013]), as otherwise certain smoothness assumptions about the boundary for the solvability for the later defined boundary value problem can not be guaranteed.

A configuration of a body Ω is a bijective function $\varphi : \Omega \subset \mathbb{R}^3 \rightarrow \Omega_t \subset \mathbb{R}^3$ that deforms the body in some Ω_t , being a subset of \mathbb{R}^3 . Here, every point \mathbf{X} in the reference configuration Ω is mapped to a unique point $\mathbf{x} = \varphi(\mathbf{X})$ in the current configuration. Then $\varphi(\Omega) = \{\varphi(\mathbf{X}) | \mathbf{X} \in \Omega\}$ describes the motion of the body Ω in \mathbb{R}^3 and is called current configuration. The motion of body Ω may be described by a series of configurations $\varphi_t : \Omega \rightarrow \mathbb{R}^3$, where for any point \mathbf{X} of the reference configuration the position at time $t \in \mathbb{R}^+$ is defined by

$$\mathbf{x} = \varphi_t(\mathbf{X}) = \varphi(\mathbf{X}, t). \quad (2.1)$$

This equation describes the curve in \mathbb{R}^3 , which denotes the path of a material particle \mathbf{X} of the reference configuration to the corresponding point \mathbf{x} in the current configuration. Fig. 2.1 depicts a sample reference configuration Ω as well as a current configuration $\varphi_t(\Omega)$. For a single point \mathbf{X} of the reference configuration, its current position $\mathbf{x}(\mathbf{X}, t)$ is displayed.

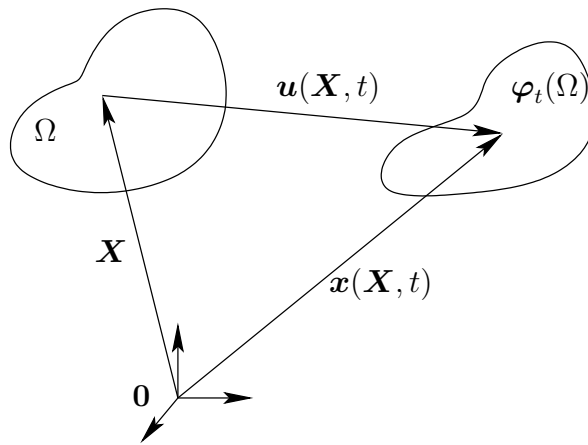


Figure 2.1: Motion of the body Ω .

The displacement vector $\mathbf{u}(\mathbf{X}, t)$ is introduced as the difference between the position vectors of the current configuration \mathbf{x} and reference configuration \mathbf{X} .

$$\mathbf{u}(\mathbf{X}, t) = \varphi(\mathbf{X}, t) - \mathbf{X} = \mathbf{x} - \mathbf{X}. \quad (2.2)$$

Obviously, it is possible to formulate all elements of \mathbb{R}^3 , such as \mathbf{X} , with respect to any given basis, especially when using different basis vectors for the reference configuration and the current configuration. In the following capital indices refer to components of the reference configuration, whereas lower case indices are related to the current configuration. For the sake of simplicity, an orthonormal basis in the reference configuration with origin $\mathbf{0}$ is assumed. The index notation of (2.1) reads

$$x_i = \varphi_i(X_A, t). \quad (2.3)$$

2.1.1 Deformation gradient

To describe the deformation process in the neighborhood of a point \mathbf{x} , the deformation gradient \mathbf{F} is defined by (cf. for example [Wriggers, 2001]),

$$\mathbf{F} = \text{Grad } \boldsymbol{\varphi}(\mathbf{X}, t) = \frac{\partial \mathbf{x}}{\partial \mathbf{X}} = \frac{\partial x_i}{\partial X_A} \mathbf{e}_i \otimes \mathbf{E}_A = F_{iA} \mathbf{e}_i \otimes \mathbf{E}_A, \quad (2.4)$$

where $\{\mathbf{E}_A\}_{A=1,\dots,3}$ denotes the basis of the reference configuration and the basis of the current configuration is denoted by $\{\mathbf{e}_i\}_{i=1,\dots,3}$. It must be stated that (2.4) assumes sufficient smoothness of the deformation field $\boldsymbol{\varphi}$. The individual components of \mathbf{F} are then given in index notation by

$$F_{iA} = \frac{\partial x_i}{\partial X_A}. \quad (2.5)$$

The deformation gradient \mathbf{F} can be interpreted as the mapping of a line segment of the reference configuration $d\mathbf{X} = \mathbf{X} - \mathbf{Y}$ with $\mathbf{X}, \mathbf{Y} \in \Omega$ to the corresponding line segment in the current configuration $d\mathbf{x} = \boldsymbol{\varphi}(\mathbf{X}) - \boldsymbol{\varphi}(\mathbf{Y})$ with $\boldsymbol{\varphi}(\mathbf{X}), \boldsymbol{\varphi}(\mathbf{Y}) \in \boldsymbol{\varphi}(\Omega)$

$$d\mathbf{x} = \mathbf{F}d\mathbf{X}. \quad (2.6)$$

As the deformation gradient \mathbf{F} is a linear operator, the local transformation in (2.4) is linear as well. The determinant J of the deformation gradient describes the change of the volume element dv of the current configuration and dV of the reference configuration

$$J = \det \mathbf{F} = \frac{dv}{dV}. \quad (2.7)$$

To avoid a deformation resulting in negative volumina and self-penetration as well as to keep the connectivity of Ω during the deformation

$$J > 0 \quad (2.8)$$

must hold. Additionally, this ensures that the deformation map is bijective. The equation (2.8) leads directly to the existence of an inverse operator \mathbf{F}^{-1} , see for example [Bronstein et al., 2001], which maps

$$d\mathbf{X} = \mathbf{F}^{-1}d\mathbf{x}. \quad (2.9)$$

Similar to (2.4), the components of \mathbf{F}^{-1} can be computed with the help of the inverse motion $\mathbf{X} = \boldsymbol{\varphi}^{-1}(\mathbf{x})$ via

$$F_{Ai}^{-1} = \frac{\partial X_A}{\partial x_i}. \quad (2.10)$$

The existence of the inverse motion is guaranteed due to the deformation function being bijective. With the help of (2.4) to (2.9) the transformation of area elements from dA in Ω to da in $\boldsymbol{\varphi}(\Omega)$ is possible with the formula of NANSON (cf. [Wriggers, 2001])

$$d\mathbf{a} = \mathbf{n}da = J\mathbf{F}^{-T}\mathbf{N}dA = J\mathbf{F}^{-T}d\mathbf{A}, \quad (2.11)$$

where \mathbf{N} denotes the normal vector to the area element in Ω and \mathbf{n} denotes the normal vector of the corresponding area element in $\boldsymbol{\varphi}(\Omega)$. For further details the reader is referred to [Ogden, 1997]. The transformations of the differential quantities are sketched in Fig. 2.2.

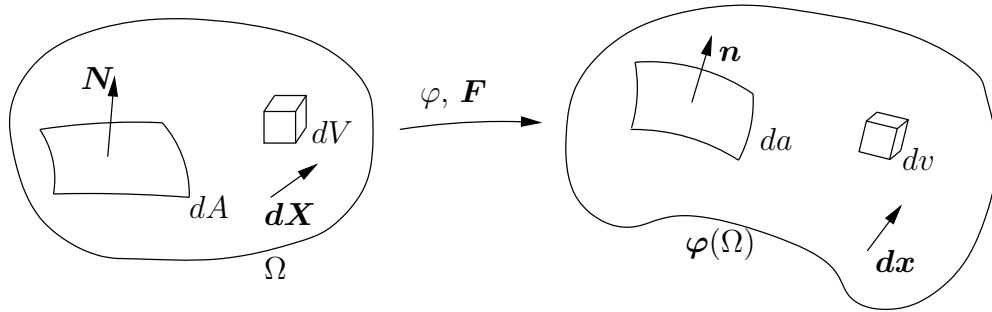


Figure 2.2: Transformation of differential quantities.

Inserting (2.2) into (2.4), \mathbf{F} can be expressed as a function of the displacement vector \mathbf{u}

$$\mathbf{F} = \text{Grad}(\mathbf{X} + \mathbf{u}(\mathbf{X}, t)) = \mathbf{I} + \text{Grad} \mathbf{u}, \quad (2.12)$$

where \mathbf{I} represents the second order identity tensor.

2.1.2 Strain measure

There exist a multitude of strain measures. For the sake of compactness only the GREEN-LAGRANGE strain measure

$$\mathbf{E} = \frac{1}{2}(\mathbf{F}^T\mathbf{F} - \mathbf{I}), \quad (2.13)$$

will be considered here. For the definition of other strain measures the reader is referred to [Holzapfel, 2000]. It is emphasized that strain tensor \mathbf{E} is defined in the reference configuration Ω . With the help of (2.12), the strain tensor \mathbf{E} can be written as

$$\mathbf{E} = \frac{1}{2} (\text{Grad } \mathbf{u} + (\text{Grad } \mathbf{u})^T + (\text{Grad } \mathbf{u})^T \text{Grad } \mathbf{u}). \quad (2.14)$$

The quadratic term $(\text{Grad } \mathbf{u})^T \text{Grad } \mathbf{u}$ establishes the nonlinear character of the GREEN-LAGRANGE strain tensor.

A body is said to undergo small deformations, if

$$z(t) = \sup_{\mathbf{X} \in \Omega, \tilde{t} \in [0, t]} \|\text{Grad } \mathbf{u}(\mathbf{X}, \tilde{t})\| \ll 1 \quad (2.15)$$

and

$$\frac{\|\mathbf{u}(\mathbf{X}, t) - \mathbf{u}_R(\mathbf{X}, t)\|}{l_0} \ll 1 \quad (2.16)$$

hold for \mathbf{u}_R denoting the corresponding rigid body motion (cf. section A.3.2) and l_0 representing a characteristic length of the body. The following asymptotic relations are then obtained (cf. [Schrade, 2011] for example):

$$\mathbf{F} = \mathbf{I} + \text{Grad } \mathbf{u} + \mathcal{O}(z), \quad (2.17)$$

$$\mathbf{F}^{-1} = \mathbf{I} - \text{Grad } \mathbf{u} + \mathcal{O}(z^2), \quad (2.18)$$

$$\det \mathbf{F} = 1 + \text{tr}(\text{Grad } \mathbf{u}) + \mathcal{O}(z^2), \quad (2.19)$$

$$\mathbf{E} = \frac{1}{2} (\text{Grad } \mathbf{u} + (\text{Grad } \mathbf{u})^T) + \mathcal{O}(z^2) \quad (2.20)$$

with trace operator tr . The linearized strain tensor $\boldsymbol{\varepsilon}$ is given by the symmetric part of the displacement gradient

$$\boldsymbol{\varepsilon} = \frac{1}{2} (\text{Grad } \mathbf{u} + (\text{Grad } \mathbf{u})^T). \quad (2.21)$$

From now on, numerical analysis is restricted to small deformations only. Thus, the following simplifications hold:

- It is not distinguished between current configuration and reference configuration, e.g. $\text{grad}(\cdot) = \text{Grad}(\cdot)$, $\partial_x(\cdot) = \partial_{\mathbf{X}}(\cdot)$.
- Linearized strains are employed $\mathbf{E} \approx \boldsymbol{\varepsilon}$.

2.2 Material law

In a mechanical context the constitutive equations describe the relation between stress $\boldsymbol{\sigma}$ and strain $\boldsymbol{\varepsilon}$. The interested reader is referred to [Han and Reddy, 2013] or [Wriggers, 2001] for a broader overview. This section introduces constitutive models for elastic, thermo-elastic, plastic and thermo-plastic material behavior. The elastic material law is used to show some basic findings on the implemented numerical methods. However, to model the complex material behavior of reinforced aluminum AMC225xe a plastic constitutive law including thermal strains is necessary. The material is introduced in more details in chapter 5.

2.2.1 Isotropic linear elasticity

In the case of linear elasticity the relation between stress $\boldsymbol{\sigma}$ and strain $\boldsymbol{\varepsilon}$ is given by HOOKE's law (cf. for example [Wriggers, 2001])

$$\boldsymbol{\sigma} = \mathbb{C} : \boldsymbol{\varepsilon}, \quad (2.22)$$

where \mathbb{C} denotes the fourth order elasticity tensor and “:” describes the double contraction of two tensors (see section A.3.1). A few general properties of the elasticity tensor \mathbb{C} are summarized here. In index notation it has the following symmetries (cf. [Wriggers, 2001])

$$\mathbb{C}_{ijkl} = \mathbb{C}_{jikl} = \mathbb{C}_{ijlk} = \mathbb{C}_{klij}. \quad (2.23)$$

The elasticity tensor \mathbb{C} is called *positive definite* (see [Han and Reddy, 2013]) if

$$\boldsymbol{\varepsilon} : \mathbb{C} : \boldsymbol{\varepsilon} > 0 \quad \forall \text{ nonzero symmetric second-order tensors } \boldsymbol{\varepsilon}. \quad (2.24)$$

Furthermore, the elasticity tensor \mathbb{C} is called *stable* (cf. [Marsden and Hughes, 1983] and [Wang and Truesdell, 1973]) if

$$\exists \alpha \in \mathbb{R}, \alpha > 0 \text{ with } \boldsymbol{\varepsilon} : \mathbb{C} : \boldsymbol{\varepsilon} \geq \alpha \|\boldsymbol{\varepsilon}\|^2 \quad \forall \text{ symmetric second order tensors } \boldsymbol{\varepsilon}, \quad (2.25)$$

where the norm of a second order tensor in this context is defined as

$$\|\boldsymbol{\varepsilon}\| = \sqrt{\varepsilon_{ij}\varepsilon_{ij}}. \quad (2.26)$$

In the case that the material is isotropic, the elasticity tensor can be expressed in terms of the LAMÉ constants $\lambda \in \mathbb{R}$ and $\mu > 0$, which are characteristic

constants of the material. The elasticity tensor then can be computed via

$$\mathbb{C}_{ijkl} = \lambda \delta_{ij} \delta_{kl} + \mu (\delta_{ik} \delta_{jl} + \delta_{il} \delta_{jk}), \quad (2.27)$$

with the KRONECKER delta δ_{ij} . With the help of (2.27), the stress strain relation (2.22) can be expressed as

$$\boldsymbol{\sigma} = \lambda \operatorname{tr}(\boldsymbol{\varepsilon}) \mathbf{I} + 2\mu \boldsymbol{\varepsilon}. \quad (2.28)$$

In engineering applications it is more common to use YOUNG's modulus

$$E = \frac{\mu(2\mu + 3\lambda)}{\mu + \lambda} \quad (2.29)$$

and POISSON's ratio

$$\nu = \frac{\lambda}{2(\mu + \lambda)}. \quad (2.30)$$

The interrelation between different elasticity constants can be found in [Becker and Gross, 2002]. With these constants the inverse relation of (2.22) is obtained by

$$\boldsymbol{\varepsilon} = \frac{1}{E} ((1 - \nu)\boldsymbol{\sigma} - \nu \operatorname{tr}(\boldsymbol{\sigma})\mathbf{I}). \quad (2.31)$$

When stability is required as in (2.25), the admissible ranges for the material constants are constrained. It can be shown (cf. for example [Marsden and Hughes, 1983]) that an isotropic linearly elastic material is stable if and only if $E > 0$ and $-1 < \nu < 1/2$.

2.2.2 Linear elasticity with thermal strains

If thermal strains are considered, the strain tensor $\boldsymbol{\varepsilon}$ is decomposed into an elastic part $\boldsymbol{\varepsilon}^{\text{el}}$ and a thermal part $\boldsymbol{\varepsilon}^{\text{th}}$

$$\boldsymbol{\varepsilon} = \boldsymbol{\varepsilon}^{\text{el}} + \boldsymbol{\varepsilon}^{\text{th}}. \quad (2.32)$$

The total strain $\boldsymbol{\varepsilon}$ is still as in (2.21)

$$\boldsymbol{\varepsilon} = \frac{1}{2} (\operatorname{Grad} \mathbf{u} + (\operatorname{Grad} \mathbf{u})^T). \quad (2.33)$$

For a given temperature difference $\Delta\vartheta$, an isotropic thermal strain is computed via

$$\boldsymbol{\varepsilon}^{\text{th}} = \alpha \Delta\vartheta \mathbf{I}. \quad (2.34)$$

The stress strain relation then reads according to a modified HOOKE'S law (cf. for example [Wriggers, 2001])

$$\boldsymbol{\sigma} = \mathbb{C} : \boldsymbol{\varepsilon}^{\text{el}} = \mathbb{C} : (\boldsymbol{\varepsilon} - \boldsymbol{\varepsilon}^{\text{th}}). \quad (2.35)$$

2.2.3 Elastoplasticity model

This section introduces a material model that covers elastic-plastic material behavior. The approach presented here follows the representation in [Han and Reddy, 2013]. So far isothermal conditions are assumed and thermal strains are not considered. Similar to the last section, the strain tensor $\boldsymbol{\varepsilon}$ is decomposed into an elastic part $\boldsymbol{\varepsilon}^{\text{el}}$ and a plastic part $\boldsymbol{\varepsilon}^{\text{pl}}$:

$$\boldsymbol{\varepsilon} = \boldsymbol{\varepsilon}^{\text{el}} + \boldsymbol{\varepsilon}^{\text{pl}}. \quad (2.36)$$

The latter describes the inelastic and irreversible material deformations due to plastic yield. The physical processes behind the two different types of deformations are very different on the crystalline level. Without going into any details, it is mentioned that on the microstructural level elastic behavior arises from the deformation of crystal lattices. In contrast, plastic deformation behavior (of metals) is typically characterized by dislocation motion (cf. [Han and Reddy, 2013]). It has been experimentally observed, that the plastic deformation of metals is nearly incompressible (cf. [Bridgman, 1970]). This observation leads to the assumption

$$\text{tr}(\boldsymbol{\varepsilon}^{\text{pl}}) = 0. \quad (2.37)$$

Similar to the last section $\boldsymbol{\varepsilon}$ is computed as in (2.21). Thus, the stress strain relation reads

$$\boldsymbol{\sigma} = \mathbb{C} : \boldsymbol{\varepsilon}^{\text{el}} = \mathbb{C} : (\boldsymbol{\varepsilon} - \boldsymbol{\varepsilon}^{\text{pl}}). \quad (2.38)$$

In contrast to thermal strains, the modeling of the plastic strains is more involved, further assumptions are necessary.

A frequent one is that the material response is rate-independent, i.e. only static situations are modeled.

For a given load situation a distinction has to be made between a plastic response and an elastic response. Whenever unloading occurs it is assumed to be of elastic nature. Hence, a scalar valued yield function f is introduced to distinguish elastic and plastic deformation.

$$\begin{aligned} f(\boldsymbol{\sigma}, \boldsymbol{\chi}) < 0 &: \text{elastic deformation only,} \\ f(\boldsymbol{\sigma}, \boldsymbol{\chi}) = 0 &: \text{plastic deformation and elastic deformation.} \end{aligned} \quad (2.39)$$

In this model, the yield function depends on the stress $\boldsymbol{\sigma}$ and a set of internal variable(s) $\boldsymbol{\chi}$. The internal variables take changes in the yield surface $f = 0$ into account. Typically the internal variables are associated with isotropic hardening and/or kinematic hardening. Depending on the physical meaning, $\boldsymbol{\chi}$ can be a scalar and/or a second order tensor.

Assuming an associated flow rule (cf. [Han and Reddy, 2013]), there exists a scalar valued $\gamma \geq 0$, called plastic rate parameter such that

$$\dot{\boldsymbol{\epsilon}}^{\text{pl}} = \gamma \frac{\partial f(\boldsymbol{\sigma}, \boldsymbol{\chi})}{\partial \boldsymbol{\sigma}}. \quad (2.40)$$

The KUHN-TUCKER conditions (cf. [Simo and Hughes, 1998]) formulate the loading-unloading relations

$$\gamma \geq 0, \quad f \leq 0, \quad \gamma f = 0. \quad (2.41)$$

If purely elastic loading occurs ($f < 0$), then it follows from the KUHN-TUCKER conditions that $\gamma = 0$. In case of the yield criterion being fulfilled ($f = 0$), a closer examination is necessary. Differentiating the third expression in (2.41) with respect to time yields

$$\dot{\gamma} f + \gamma \dot{f} = 0. \quad (2.42)$$

For the case of plastic deformation ($f = 0$) this reduces to

$$\gamma \dot{f} = 0, \quad (2.43)$$

which leads to the three cases

$$\begin{aligned} \dot{f} < 0 &\Rightarrow \gamma = 0 && \text{elastic unloading,} \\ \dot{f} = 0 &\wedge \gamma = 0 && \text{neutral loading,} \\ \dot{f} = 0 &\wedge \gamma > 0 && \text{plastic flow.} \end{aligned} \quad (2.44)$$

In this work the VON MISES yield criterion is used. It is motivated by the assumption that the threshold of elastic behavior is determined by the elastic distortion energy density (see [Han and Reddy, 2013] for further details). In the VON MISES yield criterion it is assumed that no plastic volume changes occur, hence the yield function depends on the stress deviator via

$$f(\boldsymbol{\sigma}, \boldsymbol{\chi}) = f(\boldsymbol{\sigma}, \pi) = \|\text{dev}(\boldsymbol{\sigma})\| - K(\pi), \quad (2.45)$$

where the stress deviator is defined as

$$\text{dev}(\boldsymbol{\sigma}) = \boldsymbol{\sigma} - \frac{\text{tr } \boldsymbol{\sigma}}{3} \mathbf{I}. \quad (2.46)$$

The function K describes the hardening depending on the accumulated equivalent plastic strain

$$\pi(t) = \sqrt{\frac{2}{3}} \int_0^t \|\dot{\boldsymbol{\epsilon}}^{\text{pl}}(\tau)\| d\tau. \quad (2.47)$$

Hence, beside the plastic strain $\boldsymbol{\epsilon}^{\text{pl}}$ the only internal variable necessary is the scalar valued accumulated plastic strain (cf. [Han and Reddy, 2013]). This constitutes isotropic hardening. The hardening rule considered in this work is given by the following power law

$$K(\pi) = \sqrt{\frac{2}{3}} \left(\sigma_y + \tilde{h} \pi^m \right). \quad (2.48)$$

The value σ_y is the initial yield strength and the material parameters \tilde{h} and m describe the hardening. As a consequence of the VON MISES yield criterion and the flow rule in (2.40), it follows that

$$\|\dot{\boldsymbol{\epsilon}}^{\text{pl}}\| = \left\| \gamma \frac{\partial f}{\partial \boldsymbol{\sigma}} \right\| = |\gamma| \left\| \frac{\text{dev } \boldsymbol{\sigma}}{\|\text{dev } \boldsymbol{\sigma}\|} \right\| = |\gamma| = \gamma. \quad (2.49)$$

For details see A.3.3. This and the consistency condition in (2.42) allow to compute $\gamma = \|\dot{\boldsymbol{\epsilon}}^{\text{pl}}\|$ implicitly and therewith the internal variable π from (2.47) can be obtained. As the hardening rule described in (2.48) is nonlinear (in case $m \neq 1 \wedge m \neq 0$), this implicit form is nonlinear. Its solution is found in this work via an iterative return mapping algorithm, introduced in [Simo and Taylor, 1986]. The resulting consistent elastoplastic tangent moduli are computed via a radial return algorithm for nonlinear isotropic hardening following [Simo and Hughes, 1998].

2.2.4 Elastoplasticity model with thermal strains

The combination of thermal strains with the elastoplastic material model is straight forward. Similar to the sections before, the strain tensor $\boldsymbol{\epsilon}$ needs to be decomposed. This time it is decomposed into the elastic part $\boldsymbol{\epsilon}^{\text{el}}$, the thermal part $\boldsymbol{\epsilon}^{\text{th}}$ and the plastic part $\boldsymbol{\epsilon}^{\text{pl}}$

$$\boldsymbol{\epsilon} = \boldsymbol{\epsilon}^{\text{el}} + \boldsymbol{\epsilon}^{\text{th}} + \boldsymbol{\epsilon}^{\text{pl}}. \quad (2.50)$$

Obviously, the assumption of isothermal behavior is dropped at this point. Instead the temperature is assumed to be constant in space, that is, no flow of heat is modeled. With this simplification, the stress-strain relation reads

$$\boldsymbol{\sigma} = \mathbb{C} : \boldsymbol{\varepsilon}^{\text{el}} = \mathbb{C} : (\boldsymbol{\varepsilon} - \boldsymbol{\varepsilon}^{\text{th}} - \boldsymbol{\varepsilon}^{\text{pl}}) \quad (2.51)$$

with the strain tensors as above. The resulting consistent elastoplastic tangent moduli are again computed via a radial return algorithm for nonlinear isotropic hardening following [Simo and Hughes, 1998].

2.3 Discontinuities

The focus of this work lies on bimaterial problems, i.e. the macroscopic bodies under consideration consist of different materials with some interface Γ separating the two. Fig. 2.3 illustrates such a body Ω , consisting of Ω_I and Ω_M and its separating surface Γ as well as the definition of the unit surface normal \boldsymbol{n} .

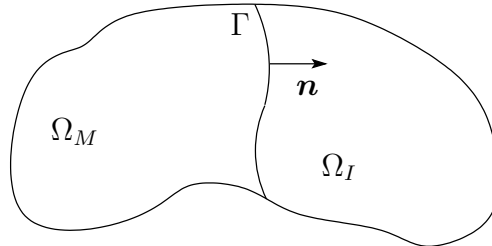


Figure 2.3: Interface Γ separating Ω_I and Ω_M .

In order to describe such interfaces appropriately, the so-called level set functions are introduced (cf. [Osher and Sethian, 1988] and [Sethian, 1999]). The advantages of using this method for describing the interface is discussed in 2.3.2. The interested reader is referred to [Osher and Fedkiw, 2003] for further details on level set methods. A more rigorous way of introducing jump conditions can be found in [Chadwick, 1999].

2.3.1 Description of discontinuities

For handling discontinuities, a jump operator $[[\cdot]]$ is introduced for a function f defined on all points \boldsymbol{x}_0 on the interface Γ separating body Ω into Ω_I and

Ω_M as depicted in Fig. 2.3

$$\llbracket f(\mathbf{x}_0) \rrbracket = \lim_{\substack{\mathbf{x} \rightarrow \mathbf{x}_0 \\ \mathbf{x} \in \Omega_I}} f(\mathbf{x}) - \lim_{\substack{\mathbf{x} \rightarrow \mathbf{x}_0 \\ \mathbf{x} \in \Omega_M}} f(\mathbf{x}). \quad (2.52)$$

This work does not consider material failure like debonding. Hence, when analyzing bimaterial problems, it is reasonable to assume a continuous displacement field along and across the interface which reads in terms of (2.52) for any given time t :

$$\llbracket \mathbf{u}(\mathbf{x}_0, t) \rrbracket = \mathbf{0} \quad \forall \mathbf{x}_0 \in \Gamma. \quad (2.53)$$

The requirement (2.53) describes a displacement jump condition that ensures a coherent interface and thereby rules out the possibility of cracks, interpenetration and tangential sliding. Nevertheless, if the different materials have varying properties like a different stiffness, the displacement field will have a kink at the interface. For the gradient of the displacement field this yields

$$\llbracket \text{grad } \mathbf{u}(\mathbf{x}_0, t) \rrbracket \neq \mathbf{0} \quad \text{for } \mathbf{x}_0 \in \Gamma \text{ in general.} \quad (2.54)$$

This leads directly to a jump in the strain field $\boldsymbol{\varepsilon}$ at the interface Γ .

$$\llbracket \boldsymbol{\varepsilon}(\mathbf{x}_0, t) \rrbracket \neq \mathbf{0} \quad \text{for } \mathbf{x}_0 \in \Gamma \text{ in general.} \quad (2.55)$$

Additionally, by the HADAMARD kinematic compatibility conditions (c.f. [Wilmanski, 2008]) the existence of a vector $\boldsymbol{\beta}_0$ can be derived from (2.53) together with

$$\forall \mathbf{x}_0 \in \Gamma \exists \boldsymbol{\beta}_0 \in \mathbb{R}^3 : \llbracket \text{grad } \mathbf{u}(\mathbf{x}_0, t) \rrbracket = \boldsymbol{\beta}_0 \otimes \mathbf{n}, \quad (2.56)$$

where \mathbf{n} denotes the unit normal vector of Γ at \mathbf{x}_0 . As a direct consequence the jump in the strain tensor can be computed via

$$\llbracket \boldsymbol{\varepsilon}(\mathbf{x}_0, t) \rrbracket = \frac{1}{2} (\boldsymbol{\beta}_0 \otimes \mathbf{n} + \mathbf{n} \otimes \boldsymbol{\beta}_0). \quad (2.57)$$

Referring to [Wilmanski, 2008] again, the jump condition for the stress tensor corresponding to (2.53) reads

$$\llbracket \boldsymbol{\sigma}(\mathbf{x}_0, t) \rrbracket \cdot \mathbf{n} = \mathbf{0} \quad \forall \mathbf{x}_0 \in \Gamma. \quad (2.58)$$

2.3.2 Level sets: Implicit functions

As mentioned in section 2.3.1 the interface is of special interest when dealing with bimaterial problems. Therefore, a technical approach on how to handle

and represent such an interface is given in this section.

Assume some volume $\Omega \subset \mathbb{R}^3$ can be disjointly divided into two subdomains $\Omega_I \subset \Omega$ and $\Omega_M \subset \Omega$ with

$$\Omega = \Omega_I \cup \Omega_M \wedge \Omega_I \cap \Omega_M = \emptyset. \quad (2.59)$$

Similar to the preceding sections, Ω_I and Ω_M are assumed to be LIPSCHITZ domains. The interface $\Gamma \subset \mathbb{R}^2$ that is separating the two is defined as the intersection of the closure of the two sets.

$$\Gamma = \overline{\Omega_I} \cap \overline{\Omega_M} \quad (2.60)$$

A proper description of Γ can be either explicitly or implicitly. In the former case one has to give the set of all points that lie on the surface $\{\mathbf{x} \in \mathbb{R}^3 \mid \mathbf{x} \in \Gamma\}$ explicitly. Alternatively, it is possible to define such an interface implicitly as the isocontour of some function $\phi(\mathbf{x}) : \Omega \subset \mathbb{R}^3 \rightarrow \mathbb{R}$, for example the iso-zero

$$\phi(\mathbf{x}) \equiv 0. \quad (2.61)$$

As for the scope of applications in this work the value of the isocontour under consideration is of no importance, from now on it will be referred to as the iso-zero whenever an isocontour is mentioned.

Obviously, when using this implicit representation, values for each point $\mathbf{x} \in \Omega$, or a discretization of the same, have to be stored. This is a numerical overhead comparing to the explicit representation, which only has to store values for $\mathbf{x} \in \Gamma$. Instead of a two-dimensional structure, a three-dimensional structure has to be resolved. Nevertheless, in the context of this work the possible gains of this approach outweigh this disadvantage.

From now on only such interfaces that have sufficiently smooth surfaces with clearly defined interior and exterior regions are considered. Thus, the function $\phi(\mathbf{x})$ provides the possibility to describe for every $\mathbf{x} \in \Omega$ whether it is part of Ω_I or Ω_M . This is done according to the following specification

$$\phi : \Omega \subset \mathbb{R}^3 \rightarrow \mathbb{R} ; \phi(\mathbf{x}) \begin{cases} > 0, & \mathbf{x} \in \Omega_M \\ = 0, & \mathbf{x} \in \Gamma \\ < 0, & \mathbf{x} \in \Omega_I \end{cases} . \quad (2.62)$$

In principal any implicit function fulfilling (2.62) may be used for describing the subdivisions of Ω properly and from now on these are referred to as level set functions. If ϕ is smooth enough, that is, it is pointwise differentiable,

i.e. $\phi \in C^1(\Omega)$, the gradient of the level set function

$$\text{grad } \phi(\mathbf{x}) = \nabla \phi(\mathbf{x}) = \left(\frac{\partial \phi(\mathbf{x})}{\partial x}, \frac{\partial \phi(\mathbf{x})}{\partial y}, \frac{\partial \phi(\mathbf{x})}{\partial z} \right) \quad (2.63)$$

exists everywhere on Ω . The gradient $\nabla \phi$ then is perpendicular to the isocontours of ϕ and obviously points in the direction of increasing ϕ . Hence, for all $\mathbf{x}_0 \in \Gamma$ the unit outward normal is defined via

$$\mathbf{N}(\mathbf{x}_0) = \frac{\nabla \phi(\mathbf{x}_0)}{|\nabla \phi(\mathbf{x}_0)|}, \quad \forall \mathbf{x}_0 \in \Gamma. \quad (2.64)$$

With (2.64) it is possible to describe further properties of the interface, in case ϕ is at least twice pointwise differentiable, i.e. $\phi \in C^2(\Omega)$. For example the curvature κ of the interface at a given point $\mathbf{x}_0 \in \Gamma$ is defined as the divergence of the unit outer normal $\mathbf{N}(\mathbf{x}_0) = (n_1(\mathbf{x}_0), n_2(\mathbf{x}_0), n_3(\mathbf{x}_0))$

$$\mathcal{K}(\mathbf{x}_0) = \nabla \cdot \mathbf{N}(\mathbf{x}_0) = \frac{\partial n_1(\mathbf{x}_0)}{\partial x} + \frac{\partial n_2(\mathbf{x}_0)}{\partial y} + \frac{\partial n_3(\mathbf{x}_0)}{\partial z}. \quad (2.65)$$

This now can be formulated with the help of the function ϕ as

$$\mathcal{K}(\mathbf{x}_0) = \nabla \cdot \left(\frac{\nabla \phi(\mathbf{x}_0)}{|\nabla \phi(\mathbf{x}_0)|} \right). \quad (2.66)$$

As sharp edges of the interface lead to singularities in the stress field of a material, the curvature provides an easy option to identify critical points at the interface of a material.

2.3.3 Level sets: Signed distance functions

A special type of the previously introduced level set functions for describing interfaces are the signed distance functions. They are defined as shown in (2.67) for Ω as in section 2.3.2.

$$\Phi : \Omega \subset \mathbb{R}^3 \rightarrow \mathbb{R}; \quad \Phi(\mathbf{x}) = \begin{cases} \min_{\mathbf{y} \in \Gamma} \|\mathbf{x} - \mathbf{y}\|, & \mathbf{x} \in \Omega_M \\ 0, & \mathbf{x} \in \Gamma \\ -\min_{\mathbf{y} \in \Gamma} \|\mathbf{x} - \mathbf{y}\|, & \mathbf{x} \in \Omega_I \end{cases}, \quad (2.67)$$

with $\|\cdot\|$ denoting the Euclidean distance in \mathbb{R}^3 . This leads directly to

$$|\nabla \Phi(\mathbf{x})| = 1, \text{ f.a.a. } \mathbf{x} \in \Omega. \quad (2.68)$$

The restriction has to be made as for a point $\mathbf{x}_0 \in \Omega$ that is equidistant to multiple points on the interface, (2.68) does not necessarily hold anymore. This is because at such a point the signed distance function has a kink and hence the gradient is not well-defined anymore, cf. [Osher and Fedkiw, 2003]. With (2.68) the computation of the curvature, cf. (2.66), simplifies to

$$\mathcal{K}(\mathbf{x}_0) = \nabla \cdot \left(\frac{\nabla \Phi(\mathbf{x}_0)}{|\nabla \Phi(\mathbf{x}_0)|} \right) = \nabla \cdot \nabla \Phi(\mathbf{x}_0) = \Delta \Phi(\mathbf{x}_0). \quad (2.69)$$

where Δ denotes the Laplace operator.

Another important property of the signed distance function is shown in (2.70). For any given point $\mathbf{x}_0 \in \Omega$ the closest point on the interface \mathbf{x}_Γ can be computed directly, i.e.,

$$\mathbf{x}_\Gamma = \mathbf{x}_0 - \Phi(\mathbf{x}_0) \frac{\nabla \Phi(\mathbf{x}_0)}{|\nabla \Phi(\mathbf{x}_0)|}. \quad (2.70)$$

Obviously, this equation has to be understood as a definition in a general sense, as again for points \mathbf{x}_0 that are equidistant to multiple points on the interface this equation does not necessarily hold anymore.

2.4 Balance equations

In this section the balance equations for the thermodynamical quantities are stated. The primary sources for this section are [Wriggers, 2001], [Altenbach et al., 1996] and [Truesdell and Noll, 2004]. For a more complete overview the interested reader is also referred to [Truesdell and Toupin, 1960], [Malvern, 1969] and [Becker and Bürger, 1975].

2.4.1 Conservation of mass

Denote the local density ρ_0 in the reference configuration and ρ in the current configuration. The global conservation of mass then is guaranteed if and only if the following equation holds

$$\int_{\varphi(\Omega)} \rho \, dv = \int_{\Omega} \rho_0 \, dV. \quad (2.71)$$

From (2.7) the relation $dv = J \, dV$ between volume elements in the reference configuration dV and in the current configuration dv is already known. This

leads directly to the local conservation of mass, which is guaranteed by

$$\rho_0 = J\rho. \quad (2.72)$$

2.4.2 Balance of momentum

The vector \mathbf{L} is introduced as a measure for the momentum, it is defined by

$$\mathbf{L} = \int_{\Omega} \rho_0 \mathbf{v} dV = \int_{\varphi(\Omega)} \rho \mathbf{v} dv, \quad (2.73)$$

where \mathbf{v} denotes the local velocity. It is known as the law of balance of momentum that the rate of change of the momentum \mathbf{L} of a body Ω is equal to the sum of all external forces applied on Ω at all times. This law is implied by NEWTON's laws of motion, see for example [Feynman et al., 1963].

Introducing volume forces \mathbf{b} (such as gravity) and surface tractions \mathbf{t} , the balance of momentum reads

$$\dot{\mathbf{L}} = \int_{\varphi(\Omega)} \rho \mathbf{b} dv + \int_{\varphi(\partial\Omega)} \mathbf{t} dv, \quad (2.74)$$

where $\partial\Omega$ describes the boundary of Ω . The CAUCHY stress tensor is introduced in the CAUCHY theorem, where the relation between a second order tensor $\boldsymbol{\sigma}$, the surface traction vector \mathbf{t} and the outer unit normal vector on the surface \mathbf{n} is given by

$$\mathbf{t} = \boldsymbol{\sigma}^T \cdot \mathbf{n} \quad (2.75)$$

where “ \cdot ” describes the contraction (cf. A.3.1). For a proof of existence of such a second order tensor field, the interested reader is referred to [Antman, 2005] or [Gurtin, 1982].

Using (2.75) and the divergence theorem (cf. for example [Bronstein et al., 2001]), the local form of (2.74) can be derived (cf. [Wriggers, 2001])

$$\operatorname{div} \boldsymbol{\sigma} + \rho \mathbf{b} = \rho \dot{\mathbf{v}}. \quad (2.76)$$

The right-hand side of (2.76) represents the inertia force and will be neglected from now on, as this work deals with quasistatic problems only. Thus, the equation of motion (2.76) degenerates to the equilibrium condition

$$\operatorname{div} \boldsymbol{\sigma} + \rho \mathbf{b} = 0. \quad (2.77)$$

2.5 Initial boundary value problem

It is now possible to formulate the initial boundary value problem. In order to do so, a solid body Ω is considered, with the surface $\partial\Omega = \partial\Omega^u \cup \partial\Omega^t$ with the so-called traction boundary $\partial\Omega^t$ and displacement boundary $\partial\Omega^u$, respectively. It is assumed that $\partial\Omega^u \cap \partial\Omega^t = \emptyset$. The quasistatic initial boundary value problem then reads:

$$\text{For a given time } T, \text{ find } \mathbf{u}(\mathbf{x}, t) : \Omega \times \mathbb{R} \rightarrow \mathbb{R}^3 \text{ such that:} \quad (2.78)$$

$$\operatorname{div} \boldsymbol{\sigma} + \rho \mathbf{b} = \mathbf{0} \quad \text{in } \Omega \times (0, T], \quad (2.79)$$

$$\mathbf{u}(\cdot, 0) = \mathbf{u}_0 \quad \text{in } \Omega, \quad (2.80)$$

$$\boldsymbol{\varepsilon} = \frac{1}{2} (\operatorname{grad} \mathbf{u} + (\operatorname{grad} \mathbf{u})^T) \quad \text{in } \Omega \times (0, T], \quad (2.81)$$

$$\boldsymbol{\sigma} \cdot \mathbf{n} = \bar{\mathbf{t}} \quad \text{on } \partial\Omega^t \times (0, T], \quad (2.82)$$

$$\mathbf{u} = \bar{\mathbf{u}} \quad \text{on } \partial\Omega^u \times (0, T]. \quad (2.83)$$

The equation (2.79) describes the strong form of the equilibrium condition. Equation (2.80) contains the initial conditions. In (2.81) the linearized strain tensor is introduced. Equation (2.82) implies the NEUMANN type traction boundary conditions and (2.83) shows the DIRICHLET type boundary conditions, where $\bar{\mathbf{u}}$ and $\bar{\mathbf{t}}$ denote the given displacement load and the given surface traction load, respectively. Fig. 2.4 illustrates the quantities in the initial boundary value problem.

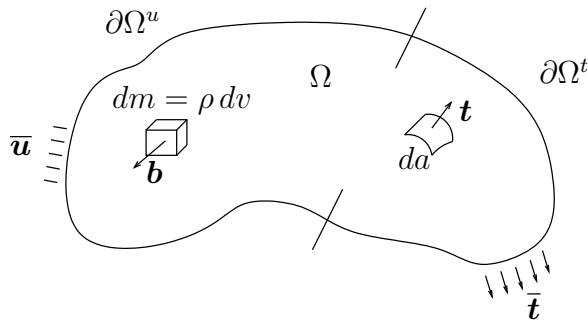


Figure 2.4: Boundary value problem with mixed boundary conditions.

To close the system, an appropriate material law has to be chosen which gives a relation between the Cauchy stress tensor $\boldsymbol{\sigma}$ and the linearized strain $\boldsymbol{\varepsilon}$. In case of linear elasticity (cf. section 2.2.1) the initial boundary value

problem then reads:

| | |
|--|---------------------------------------|
| For a given time T , find $\mathbf{u}(\mathbf{x}, t) : \Omega \times \mathbb{R} \rightarrow \mathbb{R}^3$ such that: | |
| $\operatorname{div} \boldsymbol{\sigma} + \rho \mathbf{b} = \mathbf{0}$ | in $\Omega \times (0, T]$, |
| $\mathbf{u}(\cdot, 0) = \mathbf{u}_0$ | in Ω , |
| $\boldsymbol{\varepsilon} = \frac{1}{2} (\operatorname{grad} \mathbf{u} + (\operatorname{grad} \mathbf{u})^T)$ | in $\Omega \times (0, T]$, |
| $\boldsymbol{\sigma} = \mathbf{C} : \boldsymbol{\varepsilon}$ | in $\Omega \times (0, T]$, |
| $\boldsymbol{\sigma} \cdot \mathbf{n} = \bar{\mathbf{t}}$ | on $\partial\Omega^t \times (0, T]$, |
| $\mathbf{u} = \bar{\mathbf{u}}$ | on $\partial\Omega^u \times (0, T]$, |
| for given parameters $\rho, \mathbf{b}, \mathbf{C}, \bar{\mathbf{u}}$ and $\bar{\mathbf{t}}$, | (2.84) |

with the fourth order material stiffness tensor \mathbf{C} .

As already stated in section 2.2 the second material law of interest in this work is an elastoplastic material model that considers thermal strains and has been introduced in sections 2.2.3 and 2.2.4. With this material model the initial boundary value problem reads:

| | |
|---|---------------------------------------|
| For a given time T , find $\mathbf{u}(\mathbf{x}, t) : \Omega \times \mathbb{R} \rightarrow \mathbb{R}^3$ such that: | |
| $\operatorname{div} \boldsymbol{\sigma} + \rho \mathbf{b} = \mathbf{0}$ | in $\Omega \times (0, T]$, |
| $\mathbf{u}(\cdot, 0) = \mathbf{u}_0$ | in Ω , |
| $\boldsymbol{\varepsilon} = \frac{1}{2} (\operatorname{grad} \mathbf{u} + (\operatorname{grad} \mathbf{u})^T)$ | in $\Omega \times (0, T]$, |
| $\boldsymbol{\varepsilon} = \boldsymbol{\varepsilon}^{\text{el}} + \boldsymbol{\varepsilon}^{\text{pl}} + \boldsymbol{\varepsilon}^{\text{th}}$ | in $\Omega \times (0, T]$, |
| $\boldsymbol{\sigma} = \mathbf{C} \boldsymbol{\varepsilon}^{\text{el}}$ | in $\Omega \times (0, T]$, |
| $\boldsymbol{\varepsilon}^{\text{th}} = \mathbf{I} \alpha \Delta \theta$ | in $\Omega \times (0, T]$, |
| $f(\boldsymbol{\sigma}, \pi) = \ \operatorname{dev}(\boldsymbol{\sigma})\ - \sqrt{\frac{2}{3}} (\sigma_y + h\pi^m) \leq 0$ | in $\Omega \times (0, T]$, |
| $\dot{\boldsymbol{\varepsilon}}^{\text{pl}} = \gamma \frac{\partial f(\boldsymbol{\sigma}, \pi)}{\partial \boldsymbol{\sigma}}$ | in $\Omega \times (0, T]$, |
| $\gamma \geq 0, f \leq 0, \gamma f = 0$ | in $\Omega \times (0, T]$, |
| $\boldsymbol{\sigma} \cdot \mathbf{n} = \bar{\mathbf{t}}$ | on $\partial\Omega^t \times (0, T]$, |
| $\mathbf{u} = \bar{\mathbf{u}}$ | on $\partial\Omega^u \times (0, T]$, |
| for given parameters $\rho, \mathbf{b}, \mathbf{C}, \alpha, h, m, \bar{\mathbf{u}}$ and $\bar{\mathbf{t}}$, | (2.85) |

with the material law depending parameters and functions as introduced in sections 2.2.3 and 2.2.4.

Throughout this work a displacement formulation of the problem has been chosen. That is, the problem is formulated such that (besides internal variables) the displacement is the only unknown in the system of equations. In general it is not possible to solve this type of problem analytically. An approximated solution via for example the finite element method is therefore necessary. The classical solution of the initial boundary value problem requires the solution to be twice differentiable (cf. for example Axelsson and Barker [1984]). In general this is not the case when using the finite element method (cf. Zienkiewicz and Taylor [2000]). Weak formulations of partial differential equations do not require the same strict smoothness conditions on the solution (cf. Braess [2007]). This is achieved by using weak derivatives (see A.2) instead of the normal partial derivatives and selecting an appropriate solution space (again compare with A.2). Hence, before describing the finite element method, the weak formulation of the given boundary value problem is introduced.

2.6 Weak formulation of the BVP

The displacement solution at time t is considered in the function space

$$\mathcal{S}_t = \{ \mathbf{u}(\cdot, t) \in [H^1(\Omega)]^3 \mid \mathbf{u}(\mathbf{x}, t) |_{\partial\Omega^u} = \bar{\mathbf{u}}(\mathbf{x}) \}. \quad (2.86)$$

The function spaces are introduced more thoroughly in appendix A.2. The function space of admissible test functions is

$$\mathcal{V}_t = \{ \mathbf{u}(\cdot, t) \in [H^1(\Omega)]^3 \mid \mathbf{u}(\mathbf{x}, t) |_{\partial\Omega^u} = \mathbf{0} \}. \quad (2.87)$$

Taking a so-called virtual displacement $\boldsymbol{\eta} \in \mathcal{V}$, multiplying it with (2.79) and integrating the equation over Ω leads to

$$g(\mathbf{u}, \boldsymbol{\eta}) = \int_{\Omega} (\operatorname{div} \boldsymbol{\sigma}) \cdot \boldsymbol{\eta} \, dx + \int_{\Omega} \rho \mathbf{b} \cdot \boldsymbol{\eta} \, dx = 0. \quad (2.88)$$

With the help of the divergence theorem (see for example [Bronstein et al., 2001]) as well as the fact that $\boldsymbol{\eta} = \mathbf{0}$ on $\partial\Omega^u$ and the traction boundary condition from (2.82), $g(\mathbf{u}, \boldsymbol{\eta})$ can be transformed to

$$g(\mathbf{u}, \boldsymbol{\eta}) = - \underbrace{\int_{\Omega} \boldsymbol{\sigma} : \operatorname{grad}_s \boldsymbol{\eta} \, dx}_{=a(\mathbf{u}, \boldsymbol{\eta})} + \underbrace{\int_{\partial\Omega^t} \bar{\mathbf{t}} \cdot \boldsymbol{\eta} \, dx + \int_{\Omega} \rho \mathbf{b} \cdot \boldsymbol{\eta} \, dx}_{=f(\boldsymbol{\eta})} = 0, \quad (2.89)$$

with grad_s denoting the symmetric part of the gradient operator (for details see appendix A.3.4). The weak form now reads:

$$\text{Find } u \in \mathcal{S}_t : a(\mathbf{u}, \boldsymbol{\eta}) = f(\boldsymbol{\eta}), \forall \boldsymbol{\eta} \in \mathcal{V}_t \quad (2.90)$$

for the bilinear form a and continuous linear form f introduced in (2.89). It is known (cf. for example [Bronstein et al., 2001]) that any $\mathbf{u} \in \mathcal{S}_t$ that fulfills the strong form of the initial boundary value problem (2.79) – (2.83) also fulfills (2.90). The advantage of the weak form over the initial boundary value problem is that in (2.79) the stress tensor $\boldsymbol{\sigma}$ has to be differentiable, whereas in (2.90) no such restrictions are made.

In this work the nonlinear boundary value problem (2.85) is solved with a NEWTON-RAPHSON algorithm (cf. [Simo and Hughes, 1998]) where in each iteration step the formulation is linearized by using the consistent elasto-plastic tangent moduli. Hence, a weak formulation of the boundary value problem (2.85) is not required. Nevertheless, the interested reader is referred to [Han and Reddy, 2013] for a rigorous derivation of the same.

Chapter 3

The finite element discretization

The weak form (2.90) of the initial boundary value problems defined in box (2.84) and box (2.85) are solved in this work by a finite element discretization. This chapter gives a brief introduction to the basic concepts of the finite element approach with special emphasis on details related to the specific material models of interest as well as the special handling of geometrically induced discontinuities. The chapter is based on the work of [Hughes, 1987] and [Wriggers, 2001]. For further details on the finite element method, the interested reader is also referred to [Zienkiewicz and Taylor, 2000]. For numerical procedures for solving FEM type equation systems the interested reader is referred to [Axelsson and Barker, 1984].

3.1 Discretization of the weak forms

The solution of the weak form of the initial boundary value problem given in (2.90) is a function of the infinite dimensional SOBOLEV space \mathcal{V} . An exact definition of the function spaces referenced in this section can be found in appendix A.2. The main idea behind the finite element approach is to approximate the solution in a finite dimensional subspace spanned by basis functions with local support, denoted by $\mathcal{V}^h \subset \mathcal{V}$. In the context of the finite element method this is done by subdividing the body $\Omega \subset \mathbb{R}^3$ into finitely many non-overlapping sub-elements Ω^e with the property

$$\Omega \approx \Omega^h = \bigcup_{e=1}^{n_e} \Omega^e \quad (3.1)$$

with n_e denoting the number of sub-elements. For the sake of simplicity in this work only tetrahedral decompositions are under consideration. Let \mathcal{T}_h be a quasi-uniform triangulation of Ω with some mesh parameter h . Let $\bar{\Sigma}_h$ be the set of vertices of \mathcal{T}_h contained in the closure of Ω . Additionally, let $\bar{\mathcal{N}}_h$ denote the corresponding index set of nodes in $\bar{\Sigma}_h$, where

$$n_p = |\bar{\mathcal{N}}_h| \quad (3.2)$$

denotes the number of grid points in $\bar{\Sigma}_h$. The set of all continuous piecewise linear vector-valued functions on \mathcal{T}_h , with

$$\varphi^{j,h} : \bar{\Omega} \rightarrow \mathbb{R} : \forall \mathbf{x}^i \in \bar{\Sigma}_h, j \in \bar{\mathcal{N}}_h : \varphi^{j,h}(\mathbf{x}^i) = \delta_{ij} \quad (3.3)$$

with KRONECKER delta δ_{ij} , is called a partition of unity if

$$\sum_{j \in \bar{\mathcal{N}}_h} \varphi^{j,h}(\mathbf{x}) = 1 \quad \forall \mathbf{x} \in \bar{\Omega}. \quad (3.4)$$

The approximation space \mathcal{V}^h is formed from these so-called nodal shape functions and

$$\mathcal{V}^h = \text{span} \{ \varphi^{j,h} \}_{j \in \bar{\mathcal{N}}_h} \times \text{span} \{ \varphi^{j,h} \}_{j \in \bar{\mathcal{N}}_h} \times \text{span} \{ \varphi^{j,h} \}_{j \in \bar{\mathcal{N}}_h} \quad (3.5)$$

denotes the approximation space for problem formulations in three spatial dimensions. The focus of this work lies on three-dimensional problems, where the translations in all three directions of the space are of interest, whereas rotational degrees of freedom are not considered. This results in $n_d = 3n_p$ for the total number of degrees of freedom which is equal to the dimension of \mathcal{V}^h . For later use the components of elements of \mathcal{V}^h are denoted with

$$\boldsymbol{\varphi}^{j,h} = \left(\varphi_1^{j,h}, \varphi_2^{j,h}, \varphi_3^{j,h} \right). \quad (3.6)$$

The discrete analogies of the solution spaces introduced in (2.86) and (2.87) then read

$$\mathcal{V}_t^h(\mathbf{x}) = \{ \mathbf{v}^h \in \mathcal{V}^h : v^h = 0 \text{ on } \partial\Omega \}, \quad (3.7)$$

$$\mathcal{S}_t^h(\mathbf{x}) = \{ \mathbf{v}^h \in \mathcal{V}^h : v^h = \bar{\mathbf{u}} \text{ on } \partial\Omega^u \}. \quad (3.8)$$

Instead of finding a continuous function $\mathbf{u} \in \mathcal{V}$ that gives the displacement solution for each point $\mathbf{x} \in \Omega$, the target is to find a discretized $\mathbf{u}^h \in \mathcal{S}_t^h$, where $\mathbf{u}^h = \mathbf{v}^h + \mathbf{s}^h$, with $\mathbf{v}^h \in \mathcal{V}_t^h$ and $\mathbf{s}^h \in \mathcal{S}_t^h$ defined by

$$u_k^h(\mathbf{x}) = \sum_{j=1}^{n_p} u_{(j,k)} \varphi_k^{j,h}(\mathbf{x}), \quad (3.9)$$

for spatial degree of freedom $k \in \{1, 2, 3\}$, with the unknowns $u_{(j,k)}$ such that

$$g(\mathbf{v}^h, \boldsymbol{\eta}) = g(\mathbf{u}, \boldsymbol{\eta}) - g(\mathbf{s}^h, \boldsymbol{\eta}) \quad \forall \boldsymbol{\eta} \in \mathcal{V}_t^h \quad (3.10)$$

where \mathbf{u} denotes the solution of the weak form in (2.90) and $g(\cdot, \cdot)$ is defined as in (2.89).

For the sake of simplicity the VOIGT notation is introduced. The second order stress tensor $\boldsymbol{\sigma}$ is expressed in vector form $\underline{\boldsymbol{\sigma}} = \{\sigma_{11}, \sigma_{22}, \sigma_{33}, \sigma_{23}, \sigma_{13}, \sigma_{12}\}^T$, the second order strain tensor $\boldsymbol{\varepsilon}$ as well is expressed in the vector form $\underline{\boldsymbol{\varepsilon}} = \{\varepsilon_{11}, \varepsilon_{22}, \varepsilon_{33}, 2 \cdot \varepsilon_{23}, 2 \cdot \varepsilon_{13}, 2 \cdot \varepsilon_{12}\}^T$ in both cases using the symmetry of the tensors so that only 6 different components have to be stored. Analogously the fourth order tensor \mathbf{C} is expressed in the form of a 6×6 matrix $\underline{\mathbf{C}}$

$$\mathbf{C} = [\mathbf{C}_{ijkl}] \Rightarrow [\mathbf{C}_{\alpha\beta}] = \underline{\mathbf{C}} = \begin{bmatrix} C_{11} & C_{12} & C_{13} & C_{14} & C_{15} & C_{16} \\ C_{21} & C_{22} & C_{23} & C_{24} & C_{25} & C_{26} \\ C_{31} & C_{32} & C_{33} & C_{34} & C_{35} & C_{36} \\ C_{41} & C_{42} & C_{43} & C_{44} & C_{45} & C_{46} \\ C_{51} & C_{52} & C_{53} & C_{54} & C_{55} & C_{56} \\ C_{61} & C_{62} & C_{63} & C_{64} & C_{65} & C_{66} \end{bmatrix} \quad (3.11)$$

with index shifting operator

$$\text{shift}(i, j) = \begin{cases} 1, & i = 1, j = 1 \\ 2, & i = 2, j = 2 \\ 3, & i = 3, j = 3 \\ 4, & i = 2, j = 3 \vee i = 3, j = 2 \\ 5, & i = 1, j = 3 \vee i = 3, j = 1 \\ 6, & i = 1, j = 2 \vee i = 2, j = 1 \end{cases} \quad (3.12)$$

and $\alpha = \text{shift}(i, j)$ and $\beta = \text{shift}(k, l)$, making use of the small symmetry and big symmetry of \mathbf{C} . In case of a nonlinear material model the matrix $\underline{\mathbf{C}}$ describes the VOIGT notation of the material stiffness tangent modulus introduced in section 2.2.

Let $\boldsymbol{\eta}$ be an arbitrary function in \mathcal{V}^h with

$$\boldsymbol{\eta}(\mathbf{x}) = \sum_{j=1}^{n_p} \begin{bmatrix} \eta_{1j} \varphi_1^{j,h}(\mathbf{x}) \\ \eta_{2j} \varphi_2^{j,h}(\mathbf{x}) \\ \eta_{3j} \varphi_3^{j,h}(\mathbf{x}) \end{bmatrix} \quad (3.13)$$

for some η_{ij} . Additionally, introducing the operator

$$\mathbf{S} = \begin{bmatrix} \partial_x & 0 & 0 \\ 0 & \partial_y & 0 \\ 0 & 0 & \partial_z \\ 0 & \partial_z & \partial_y \\ \partial_z & 0 & \partial_x \\ \partial_y & \partial_x & 0 \end{bmatrix} \quad (3.14)$$

the symmetric gradient operator of this function $\boldsymbol{\eta}$ then can be expressed vector-wise via

$$\text{grad}_s \boldsymbol{\eta} = \sum_{j=1}^{n_p} \mathbf{S} \varphi^{j,h}(\mathbf{x}) \begin{bmatrix} \eta_1 \\ \eta_2 \\ \eta_3 \end{bmatrix}_j =: \sum_{j=1}^{n_p} \mathbf{B}_j(\mathbf{x}) \boldsymbol{\eta}_j \quad (3.15)$$

and it reads

$$\mathbf{B}_j(\mathbf{x}) = \begin{bmatrix} \frac{\partial \varphi_1^{j,h}}{\partial x}(\mathbf{x}) & 0 & 0 \\ 0 & \frac{\partial \varphi_2^{j,h}}{\partial y}(\mathbf{x}) & 0 \\ 0 & 0 & \frac{\partial \varphi_3^{j,h}}{\partial z}(\mathbf{x}) \\ 0 & \frac{\partial \varphi_2^{j,h}}{\partial z}(\mathbf{x}) & \frac{\partial \varphi_3^{j,h}}{\partial y}(\mathbf{x}) \\ \frac{\partial \varphi_1^{j,h}}{\partial z}(\mathbf{x}) & 0 & \frac{\partial \varphi_3^{j,h}}{\partial x}(\mathbf{x}) \\ \frac{\partial \varphi_1^{j,h}}{\partial y}(\mathbf{x}) & \frac{\partial \varphi_2^{j,h}}{\partial x}(\mathbf{x}) & 0 \end{bmatrix}. \quad (3.16)$$

In this work the discretization is done with tetrahedrons, using linear shape functions. Using the isoparametric concept (cf. for example [Belytschko et al., 2000]), all integrations are performed on the isoparametrical reference tetrahedron Ω^{ref} , persisting of the four nodes

$$\left\{ (0, 0, 0)^T, (1, 0, 0)^T, (0, 1, 0)^T, (0, 0, 1)^T \right\}. \quad (3.17)$$

The corresponding shape functions on the reference tetrahedron then are

$$N_1 = 1 - x - y - z, \quad (3.18)$$

$$N_2 = x, \quad (3.19)$$

$$N_3 = y, \quad (3.20)$$

$$N_4 = z, \quad (3.21)$$

where the letter N is used instead of φ to emphasize the coordinate transformation from any given element Ω^e to Ω^{ref} . It can be seen easily that these

shape functions form a partition of unity as

$$\sum_{i=1}^4 N_i(\mathbf{x}) = 1 \quad \forall \mathbf{x} \in \Omega^{\text{ref}}. \quad (3.22)$$

Additionally, let J^e denote the functional determinant of the coordinate transformation from a given element Ω^e to Ω^{ref} .

With all these preambles it is now possible to formulate the discretized linear increment Δa of the weak form from (2.90) depending on the increment $\Delta \mathbf{u}$ of the displacement vector \mathbf{u} . It reads

$$\Delta a = \int_{\Omega} \text{grad}_s \boldsymbol{\eta} : \frac{\partial \boldsymbol{\sigma}}{\partial \boldsymbol{\varepsilon}} \text{grad}_s \Delta \mathbf{u} \, dv \quad (3.23)$$

$$\approx \bigcup_{e=1}^{n_e} \int_{\Omega^e} \text{grad}_s \boldsymbol{\eta} : \frac{\partial \boldsymbol{\sigma}}{\partial \boldsymbol{\varepsilon}} \text{grad}_s \Delta \mathbf{u} \, dv \quad (3.24)$$

$$\approx \bigcup_{e=1}^{n_e} \int_{\Omega^{\text{ref}}} \left(\sum_{j=1}^{n_p} \mathbf{B}_j(\mathbf{x}) \boldsymbol{\eta}_j \right)^T \mathbf{C} \left(\sum_{k=1}^{n_p} \mathbf{B}_k(\mathbf{x}) \Delta \mathbf{u}_k \right) J^e \, dv \quad (3.25)$$

$$= \bigcup_{e=1}^{n_e} \sum_{j=1}^{n_p} \sum_{k=1}^{n_p} \boldsymbol{\eta}_j^T \int_{\Omega^{\text{ref}}} \underbrace{\mathbf{B}_j^T \mathbf{C} \mathbf{B}_k}_{=K_{jk}^e} J^e \, dv \cdot \Delta \mathbf{u}_k \quad (3.26)$$

with the assembling operator \bigcup (cf. [Hughes, 1987] for example). Analogously the assembling of the linear form f reads

$$f(\boldsymbol{\eta}) = \int_{\partial \Omega^t} \bar{\mathbf{t}} \cdot \boldsymbol{\eta} \, dx + \int_{\Omega} \rho \mathbf{b} \cdot \boldsymbol{\eta} \, dx \quad (3.27)$$

$$\approx \bigcup_{e=1}^{n_e} \sum_{j=1}^{n_p} \boldsymbol{\eta}_j^T \int_{\Omega^{\text{ref}}} \underbrace{(1_{\Omega^t}(\mathbf{x}) \bar{\mathbf{t}} + \rho \mathbf{b})}_{=F_j^e} \, dx \quad (3.28)$$

with the characteristic function

$$1_{\Omega^t}(\mathbf{x}) = \begin{cases} 1, & \mathbf{x} \in \Omega^t \\ 0, & \mathbf{x} \notin \Omega^t \end{cases}. \quad (3.29)$$

As the weak form $a(\mathbf{u}, \boldsymbol{\eta}) = f(\boldsymbol{\eta})$ must hold for any function $\boldsymbol{\eta} \in \mathcal{V}_t^h$, it is

valid especially for its basis functions $\left\{ \varphi_k^{1,h}, \dots, \varphi_k^{n_p,h} \right\}_{k=1,\dots,3}$. Each of these n_d different equations are forming a single row of a matrix vector multiplicative equation and hence can be expressed as

$$\mathbf{K} \Delta \mathbf{u} = \mathbf{F} \quad (3.30)$$

with the sparse stiffness matrix \mathbf{K} . The matrix \mathbf{K} has nonzero entries only at row i and column j if there exists an element Ω^e that contains the node corresponding to the global degrees of freedom i as well as the one corresponding to the global degree of freedom j .

3.2 Discretization with the XFEM

As described in section 2.3.1, the displacement field $\mathbf{u}(\cdot)$ has kinks at the interface. The definition of \mathcal{S}_t^h in (3.7) and (3.8) implies that the piecewise linear solution field can only have kinks exactly at the interface between some connecting sub-elements Ω^{e_1} and Ω^{e_2} . Hence, whenever the corresponding mesh is not adapted to the interface in a proper way, a systematic error in the solution is introduced.

A possible way to overcome this methodological drawback is to use the extended finite element method (XFEM) introduced by [Belytschko and Black, 1999] and [Moës et al., 1999] (the interested reader is as well referred to [Sukumar et al., 2000], [Sukumar et al., 2001] and [Dolbow, 1999]). The XFEM makes use of the a priori knowledge that at the material interface there are kinks in the displacement field and jumps in the strain field without the need of adopting the mesh to the geometrical information of the interface. This is achieved by enlarging the solution space \mathcal{V}^h accordingly. Besides the existing basis functions $\varphi_k^{j,h}$ from (3.3) further basis functions are introduced that are able to produce an arbitrary kink at a predefined position. The solution approximated with XFEM reads

$$\mathbf{u}_h^{\text{xfem}}(\mathbf{x}) = \left(\underbrace{\sum_{i \in \bar{\mathcal{N}}_h} \varphi^{i,h}(\mathbf{x}) \mathbf{u}_i}_{\text{classical FEM ansatz}} + \underbrace{\sum_{i \in \bar{\mathcal{N}}_h^*} \varphi^{i,h}(\mathbf{x}) F(\mathbf{x}) \mathbf{a}_i}_{\text{enrichment term}} \right) \in \tilde{\mathcal{V}}^h, \quad (3.31)$$

where $\bar{\mathcal{N}}_h^* \subset \bar{\mathcal{N}}_h$ denotes the set of enriched nodes. The variable \mathbf{u}_i describes the unknown displacement of node i . The function $F(\mathbf{x})$ characterizes the enrichment function which specifies the type and position of the discontinuity

within the element of interest. The variable \mathbf{a}_i represents additional enrichment unknowns which describe the exact value, slope etc. of the discontinuity. The enriched basis of the solution space $\tilde{\mathcal{V}}^h$ is given by

$$\{\varphi^{j,h}\}_{j \in \bar{\mathcal{N}}_h} \cup \{\varphi^{j,h} F\}_{j \in \bar{\mathcal{N}}_h^*}. \quad (3.32)$$

The exact choice of $\bar{\mathcal{N}}_h^*$ and $F(\mathbf{x})$ depends on the type of enrichment. The origin of this method lies in the work of [Babuska and Melenk, 1995] and [Melenk and Babuška, 1996] where a global enrichment is introduced and $\bar{\mathcal{N}}_h^* = \bar{\mathcal{N}}_h$. Later in [Belytschko and Black, 1999] and [Moës et al., 1999] a local enrichment function is used that leads to a significant reduction of the number of nodes that need an enrichment and therewith the computation costs are reduced significantly. There exists a multitude of different possible types of enrichments, depending on the exact type of discontinuity of the problem at hand. For a good overview, the interested reader is referred to [Fries and Belytschko, 2010]. The most common approach is to make use of the level set method introduced in 2.3.2 to generate an enrichment function. The XFEM was first combined with the level set method by [Belytschko et al., 2001] and [Stolarska et al., 2001]. This work considers bimaterial problems only, for which the so-called “modified abs enrichment” introduced in [Moës et al., 2003] is common (cf. [Fries and Belytschko, 2010]). It is able to reproduce kinks in the displacement field and as it is shown later, it has in comparison to other possible enrichment functions a minimal set of $\bar{\mathcal{N}}_h^*$. The modified abs enrichment makes use of a discretized version of the signed distance function, introduced in section 2.3.3, by employing the shape functions of the underlying finite element mesh. For any given point $\mathbf{x} \in \Omega$ the value of the signed distance function is approximated via

$$\Phi(\mathbf{x}) \approx \sum_{i \in K(\mathbf{x})} \varphi^{i,h}(\mathbf{x}) \Phi(\mathbf{x}^i), \quad (3.33)$$

where the index set $K(\mathbf{x})$ represents the set of all nodes of the element that contains point \mathbf{x} and \mathbf{x}^i denotes the corresponding coordinates of node i . With (3.33) a synergy between the existing finite element mesh and the exact geometrical description of the body Ω is utilized at the cost of introducing a small geometrical error. This error typically can be neglected. In chapter 4 a more detailed error analysis can be found. With the approximation from

(3.33) the modified abs enrichment reads

$$F(\mathbf{x}) = \sum_{i \in K(\mathbf{x})} \varphi^{i,h}(\mathbf{x}) |\Phi(\mathbf{x}^i)| - \left| \sum_{i \in K(\mathbf{x})} \varphi^{i,h}(\mathbf{x}) \Phi(\mathbf{x}^i) \right|. \quad (3.34)$$

In case of \mathbf{x} being in an element where the level set function of all of the elements nodes has the same sign, i.e.

$$\text{sign}(\Phi(\mathbf{x}^i)) = \text{sign}(\Phi(\mathbf{x}^j)) \quad \forall i \neq j \in K(\mathbf{x}), \quad (3.35)$$

the enrichment function vanishes obviously and $F(\mathbf{x}) = 0$ holds. Hence, only the nodes of elements containing the interface have to be enriched and $\bar{\mathcal{N}}_h^*$ is equal to all the nodes of all of the elements containing the interface. As shown in [Fries, 2008], many other types of XFEM enrichment functions run into problems at the blending elements, that are elements which are not cut by the interface but are a neighbor element of a cut element. The origin of the problem is

$$F(\mathbf{x}^i) \neq 0 \quad \text{for some nodes } \mathbf{x}^i, \quad (3.36)$$

which leads to unwanted higher order terms in the displacement approximation in the blending elements. This problem usually is circumvented by enlarging $\bar{\mathcal{N}}_h^*$ to include the nodes of all blending elements as well and to introduce a special treatment of the blending elements (again cf. [Fries, 2008]). With the enhanced abs enrichment of (3.34) this is not necessary (cf. for example [Fries and Belytschko, 2010]) as for all nodes \mathbf{x}^i it holds that

$$\begin{aligned} F(\mathbf{x}^i) &= \sum_{j \in K(\mathbf{x}^i)} \varphi^{j,h}(\mathbf{x}^i) |\Phi(\mathbf{x}^j)| - \left| \sum_{j \in K(\mathbf{x}^i)} \varphi^{j,h}(\mathbf{x}^i) \Phi(\mathbf{x}^j) \right| \\ &= \sum_{j \in K(\mathbf{x}^i)} \delta_{ij} |\Phi(\mathbf{x}^j)| - \left| \sum_{j \in K(\mathbf{x}^i)} \delta_{ij} \Phi(\mathbf{x}^j) \right| \\ &= |\Phi(\mathbf{x}^i)| - |\Phi(\mathbf{x}^i)| \\ &= 0 \end{aligned} \quad (3.37)$$

with KRONECKER delta δ_{ij} . Up to now, no enrichment is known that is able to reproduce kinks in the displacement field exactly, that uses a smaller set of enriched nodes $\bar{\mathcal{N}}_h^*$ than the here suggested one (again cf. [Fries and Belytschko, 2010]).

Introducing the abbreviation $\Phi_i = \Phi(\mathbf{x}^i)$ for node \mathbf{x}^i , the XFEM discretization of the standard enhanced abs enrichment by Moës (cf. [Moës et al.,

2003]) reads

$$\begin{aligned}
 u_k^h(\mathbf{x}) &= \sum_{i \in \mathcal{N}_h} \varphi^{i,h}(\mathbf{x}) u_{(i,k)} \\
 &+ \sum_{i \in \mathcal{N}_h^*} \varphi^{i,h}(\mathbf{x}) \left(\sum_{j \in K(\mathbf{x})} |\Phi_j| \varphi^{j,h}(\mathbf{x}) - \left| \sum_{j \in K(\mathbf{x})} \Phi_j \varphi^{j,h}(\mathbf{x}) \right| \right) a_{(i,k)}.
 \end{aligned} \tag{3.38}$$

For the XFEM discretization of the weak form given in (2.90), analogously to subsection 3.1, the partial derivatives of the shape functions corresponding to the enriched degrees of freedom, namely

$$\tilde{\varphi}^{i,h}(\boldsymbol{\xi}(\mathbf{x})) = \varphi^{i,h}(\boldsymbol{\xi}(\mathbf{x})) \left(\sum_{j \in I_i} |\phi_j| \varphi^{j,h}(\boldsymbol{\xi}(\mathbf{x})) - \left| \sum_{j \in I_i} \phi_j \varphi^{j,h}(\boldsymbol{\xi}(\mathbf{x})) \right| \right) \tag{3.39}$$

are required with $\boldsymbol{\xi} : \mathbb{R}^3 \rightarrow \mathbb{R}^3$ denoting the transformation to the reference element. The partial derivatives in direction ξ_k are obtained as

$$\begin{aligned}
 \partial_{\xi_k} \tilde{\varphi}^{i,h}(\boldsymbol{\xi}) &= \left(\sum_{j \in I_i} |\phi_j| \varphi^{j,h}(\boldsymbol{\xi}) - \left| \sum_{j \in I_i} \phi_j \varphi^{j,h}(\boldsymbol{\xi}) \right| \right) \partial_{\xi_k} \varphi^{i,h}(\boldsymbol{\xi}) \\
 &+ \left(\sum_{j \in I_i} |\phi_j| \partial_{\xi_k} \varphi^{j,h}(\boldsymbol{\xi}) - \text{sign} \left(\sum_{j \in I_i} \phi_j \varphi^{j,h}(\boldsymbol{\xi}) \right) \sum_{j \in I_i} \phi_j \partial_{\xi_k} \varphi^{j,h}(\boldsymbol{\xi}) \right) \varphi^{i,h}(\boldsymbol{\xi}).
 \end{aligned} \tag{3.40}$$

The matrix \mathbf{B} can be obtained using operator \mathbf{S} from (3.14) via

$$\mathbf{B} = \mathbf{S}[\varphi^{1,h}, \dots, \varphi^{n_{el},h}, \tilde{\varphi}^{1,h}, \dots, \tilde{\varphi}^{n_{el}^*,h}] \tag{3.41}$$

with $\dim(\mathbf{B}) = 6 \times 3 \cdot (n_{el} + n_{el}^*)$ and n_{el} denoting the number of nodes of the reference element and n_{el}^* the number of enriched elements of the reference element, respectively. Of course in the case of the modified abs enrichment it always holds that

$$n_{el}^* = \begin{cases} 0, & \text{element not cut by interface,} \\ n_{el}, & \text{element cut by interface.} \end{cases} \tag{3.42}$$

The XFEM discretization of (2.90) then reads

$$\bigcup_{e=1}^{n_e} \int_{\Omega_e} \mathbf{B}^T \mathbf{C} \mathbf{B} d_e^h d\Omega_e = \tilde{\mathbf{F}} \tag{3.43}$$

with

$$\tilde{\mathbf{F}} = \left(F_1, \dots, F_{n_d}, \underbrace{0, \dots, 0}_{3|\mathcal{N}_h^*| \text{ values}} \right). \quad (3.44)$$

The vector \mathbf{d}_e^h contains the unknowns corresponding to the element Ω_e , right hand side entries F_i are similar to (3.27) and the assembling operator is again denoted by \cup (cf. [Hughes, 1987] for example). In case of an enriched tetrahedral element this results in 24 degrees of freedom as each of the 4 nodes has both a displacement unknown and an enrichment unknown for each of the three spatial dimensions and it reads

$$\mathbf{d}_e^h = (u_{1x}, u_{1y}, u_{1z}, \dots, u_{4x}, u_{4y}, u_{4z}, a_{1x}, a_{1y}, a_{1z}, \dots, a_{4x}, a_{4y}, a_{4z}). \quad (3.45)$$

Ordering of unknowns

When assembling the global stiffness matrix for the enriched system, there are two different principal possibilities of ordering the unknowns. The first possibility is called mixed ordering, where the displacement unknowns u_i and the enrichment unknowns a_i are ordered according to the node number, for example

$$\mathbf{d}^h = (u_{1x}, u_{1y}, u_{1z}, a_{1x}, a_{1y}, a_{1z}, \dots, u_{n_{el}x}, u_{n_{el}y}, u_{n_{el}z}, a_{n_{el}x}, a_{n_{el}y}, a_{n_{el}z}) \quad (3.46)$$

with obviously a_{ix}, a_{iy}, a_{iz} existing only if node i is enriched. It results in a bandwidth of the global stiffness matrix comparable to the one of the standard FEM. The disadvantage of this ordering is a more complicated implementation, because standard FEM elements need a new method for finding the correct index-vector for the assembling process.

The second possibility is called separate ordering where the unknowns are separated within the solution vector \mathbf{d}^h , for example

$$\mathbf{d}^h = (u_{1x}, u_{1y}, u_{1z}, \dots, u_{n_{el}x}, u_{n_{el}y}, u_{n_{el}z}, a_{1x}, a_{1y}, a_{1z}, \dots, a_{n_{el}^*x}, a_{n_{el}^*y}, a_{n_{el}^*z}). \quad (3.47)$$

This method has the advantage that it is easy to implement. Additionally, it is easy to validate as the upper left part of the global stiffness matrix is similar to the one using standard FEM in case the material properties are constant over each of the elements. The disadvantage of this method is a dramatically increased bandwidth of the global stiffness matrix compared to the standard FEM. This is due to the fact that K_{ij} for i corresponding to displacement unknown u_{i^*} and enrichment unknown a_{j^*} typically is nonzero if there exists an element containing both nodes i^* and j^* . Hence, a preconditioning of the

global stiffness matrix is mandatory when using separated ordering of the unknowns. Due to the better validation properties of this second ordering, in this work a separated ordering is chosen.

It is emphasized that the later analysis of eigenvalues of the global stiffness matrix is not influenced by the ordering of unknowns as a permutation of the indices of a matrix does not influence its eigenvalues (cf. [Bronstein et al., 2001] for example).

Numerical quadrature of enriched elements

For XFEM elements a new quadrature rule has to be implemented, as typically these elements are cut with the material interface. Hence, the material parameters are not constant in the volume and a special treatment of these cells is required. Special emphasis needs to be put on the fact that second order accuracy is required for an exact quadrature rule within XFEM elements when using the enhanced abs enrichment of (3.34) (see A.1 for further details). The easiest way to do a proper numerical quadrature of the enriched elements is to subdivide the cut element into subelements with constant material parameters and do a Gauß quadrature on the subelements. As an alternative the interested reader is referred to [Ventura, 2006] which circumvents subcell integration with the help of surface integrals.

In case of a tetrahedral element supposedly cut by an interface, only three different possibilities can occur. They are distinguished by the number of nodes that share the sign of the nodal level set value.

- (i) Level set values share the same sign at all nodes. Hence, the element is not cut by material interface and does not have to be enriched when using the enhanced abs enrichment. Thus, a standard quadrature rule for non-enriched elements can be used.
- (ii) A single node is cut from the rest of the element, that is three of the four nodal level set values share the sign. The volume cut away including the single node must again be a tetrahedron, the rest of the body can be divided into three more tetrahedrons. The quadrature of the whole element is then achieved by applying standard four point Gauß quadrature rule subelement-wise.
- (iii) The four nodes are separated in pairs of two sharing the sign of the nodal level set value. As each node is connected to every other node within a tetrahedron no further distinctions have to be made. Both volumes can be divided into three tetrahedrons each. Again the quadra-

ture of the whole element is then achieved by standard four point Gauß quadrature rule on each subelement.

Of course in the cases (ii) and (iii) the exact interface location within the element needs to be computed from the level set values at the nodes of the original tetrahedron. This is realized straight forward with (3.33). The location of the individual evaluation points for the numerical quadrature are then easily computed according to the exact coordinates of each sub-tetrahedron. As the volume of these sub-tetrahedrons is known as well, the weight for each evaluation point is then computed according to the chosen four point Gauß quadrature rule and the size of the sub-tetrahedron.

It is emphasized that a four point Gauß quadrature rule with all four evaluation points lying in the inner of the reference tetrahedron is strongly recommended. Otherwise, it is possible to end up with an integration point on the material interface, where it is not clear which material parameters to choose for the evaluation of the weak form.

For a better understanding a few examples of how to locate the evaluation points for the Gauß quadrature are visualized in Fig. 3.1 to Fig. 3.4.

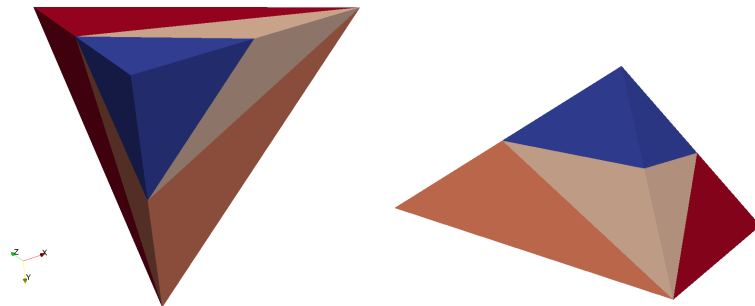


Figure 3.1: Cut case (ii): one node in blue phase is cut away from three nodes in red phase.

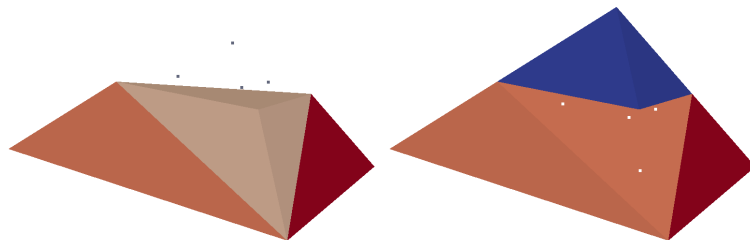


Figure 3.2: Cut case (ii): example locations of Gauß points.

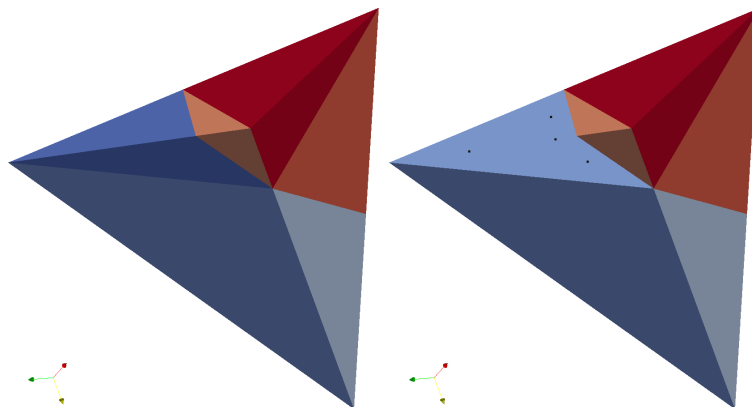


Figure 3.3: Cut case (iii): two nodes in blue phase are cut away from two nodes in red phase.

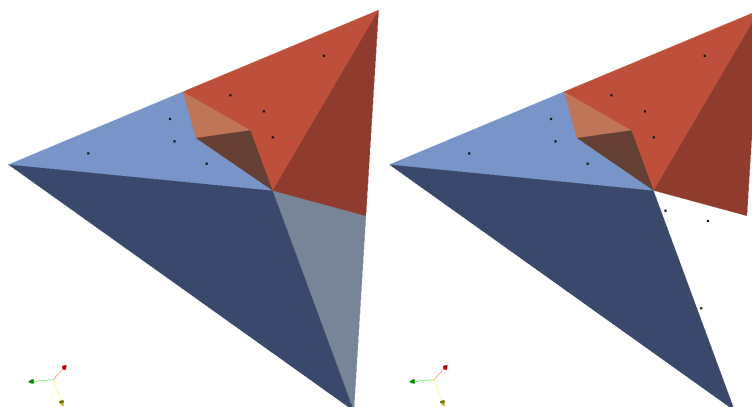


Figure 3.4: Cut case (iii): example locations of Gauß points.

Obviously, this procedure is a numerical overhead when comparing the XFEM to standard FEM. Nevertheless the computational costs are significantly smaller than standard FEM with local mesh refinement with a comparable accuracy (cf. for example Bordas et al. [2010]).

Linear dependence and ill-conditioning

A well-known fact from literature (cf. for example [Fries and Belytschko, 2010]) is that the enriched basis functions of the enhanced abs enrichment become linear dependent in case of a nodal level set value being equal to zero. This leads to a degenerated global stiffness matrix. It is also known (again cf. [Fries and Belytschko, 2010]) that the basis functions become almost linear

dependent in case of nodal level set values being close to zero. This results in an ill-conditioning of the global stiffness matrix. Only surprisingly few publications address this problem and it will be thoroughly analyzed in sections 4.1 and 4.2. Additionally, in section 4.4 the possible countermeasures are discussed and a novel approach of circumventing this problem is introduced.

Boundary conditions

It is emphasized that when implementing the XFEM some special consideration has to be put on correct boundary conditions. Especially when assuming *DIRICHLET* type boundary conditions, it often is necessary to block the corresponding enriched degrees of freedom for some boundary elements. Additionally, it is possible to impose *NEUMANN* type boundary conditions with kinks at the predefined level set isozero contour at the boundary. Of course the latter can also be achieved with standard FEM but again only if the underlying mesh is able to resolve the isozero contour which in general is not the case.

Chapter 4

Numerical behavior and properties

In this chapter some numerical analyses and algorithms are presented. The simulations described in the following have all been computed with FEELMATH (Finite Elements for Elastic MATERIALs and Homogenization), an in-house software project of the Fraunhofer Institute for Industrial Mathematics (ITWM) [FeelMath, 2014].

4.1 One-dimensional model problem

Consider a one-dimensional bar of length 1, having a discontinuous jump in its cross section at $s \in (0, 1)$, cf. Fig. 4.1 and a point force F at the right end of the bar.

For the sake of simplicity in this example the units of all parameters are ignored.

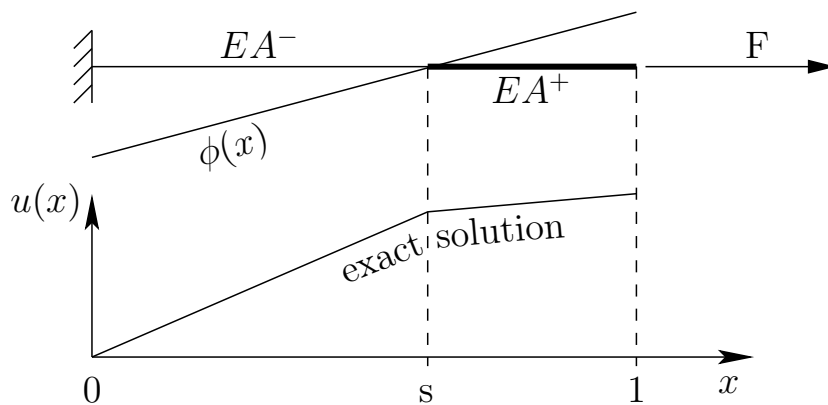


Figure 4.1: Problem statement and exact solution.

A constant YOUNG'S modulus E is assumed and the cross section is defined as

$$A(x) = \begin{cases} A^- \in \mathbb{R}, & 0 \leq x < s \\ A^+ \in \mathbb{R}, & s \leq x \leq 1. \end{cases} \quad (4.1)$$

The governing equation without a line force in strong form is

$$\frac{\partial}{\partial x} \left[EA(x) \frac{\partial u}{\partial x} \right] = 0 \quad (4.2)$$

and in weak form it reads

find $u(x)$ such that $\forall w \in: \mathcal{V}^h$

$$0 = \int_{x=0}^1 EA(x) \partial_x w(x) \partial_x u(x) dx - [EA w(x) \partial_x u(x)]_0^1 - F w(x)$$

$$= EA^- \int_{x=0}^s \partial_x w(x) \partial_x u(x) dx + EA^+ \int_{x=s}^1 \partial_x w(x) \partial_x u(x) dx - F w(x).$$

(4.3)

Introducing a DIRICHLET type boundary condition on the left side ($x = 0$) with $u(0) = 0$ and a NEUMANN type boundary condition on the right side ($x = 1$) with $F = EA(1) \partial_x u(1) = EA^+ \partial_x u(1)$, the exact solution then reads

$$u(x) = \begin{cases} \frac{F}{EA^-} x, & 0 \leq x < s \\ \frac{F}{EA^-} s + \frac{F}{EA^+} (x - s), & s \leq x \leq 1 \end{cases} \quad (4.4)$$

and is piecewise linear with a weak discontinuity at $x = s$, cf. Fig. 4.1.

4.1.1 Exact XFEM element for the model problem

The level set function defining the discontinuity position used in this example is the signed distance function

$$\Phi(x) = x - s. \quad (4.5)$$

The values of the level set function at the borders is then

$$\begin{aligned} \phi_1 &= \Phi(x = 0) = -s, \\ \phi_2 &= \Phi(x = 1) = 1 - s. \end{aligned} \quad (4.6)$$

The domain is discretized with a single element and enhanced abs enrichment is used. Linear shape functions are chosen for standard part and enrichment part of the FEM discretization. Analogously to section 3.2 this leads to

$$u^h(x) = N_1(x)u_1 + N_2(x)u_2 + M_1(x)a_1 + M_2(x)a_2, \quad (4.7)$$

with standard linear shape functions

$$\begin{aligned} N_1(x) &= x, \\ N_2(x) &= 1 - x \end{aligned} \tag{4.8}$$

as well as the standard enhanced abs enrichment shape functions by MOËS (cf. [Moës et al., 2003])

$$M_i(x) = N_i(x) \left(\sum_{j \in I_i} |\phi_j| N_j(x) - \left| \sum_{j \in I_i} \phi_j N_j(x) \right| \right). \tag{4.9}$$

In this example the enrichment shape functions then read

$$\begin{aligned} M_1(x) &= N_1(x) (|\phi_1| N_1(x) + |\phi_2| N_2(x) - |\phi_1 N_1(x) + \phi_2 N_2(x)|) \\ &= (1 - x) (s + x - 2sx - |x - s|), \\ M_2(x) &= N_2(x) (|\phi_1| N_1(x) + |\phi_2| N_2(x) - |\phi_1 N_1(x) + \phi_2 N_2(x)|) \\ &= x (s + x - 2sx - |x - s|). \end{aligned} \tag{4.10}$$

Splitting these up according to

$$M_i(x) = \begin{cases} M_i^-(x), & 0 \leq x < s \\ M_i^+(x), & s \leq x \leq 1 \end{cases}, \quad i = 1, 2, \tag{4.11}$$

the shape functions read

$$\begin{aligned} M_1^-(x) &= (1 - x) (s + x - 2sx - |x - s|) \\ &= (1 - x) (2x - 2sx), \end{aligned} \tag{4.12}$$

$$\begin{aligned} M_1^+(x) &= (1 - x) (s + x - 2sx - |x - s|) \\ &= (1 - x) (2s - 2sx), \end{aligned} \tag{4.13}$$

$$\begin{aligned} M_2^-(x) &= x (s + x - 2sx - |x - s|) \\ &= x (2x - 2sx), \end{aligned} \tag{4.14}$$

$$\begin{aligned} M_2^+(x) &= x (s + x - 2sx - |x - s|) \\ &= x (2s - 2sx). \end{aligned} \tag{4.15}$$

Fig. 4.2 shows for an example of the resulting shape functions with $s = 0.6$ for the position of the interface.

Already in section 3.2 possible problems in blending elements are mentioned for the case where the enrichment shape functions are nonzero at the nodal points. It is also proven in (3.37) that this is always the case for the mod-

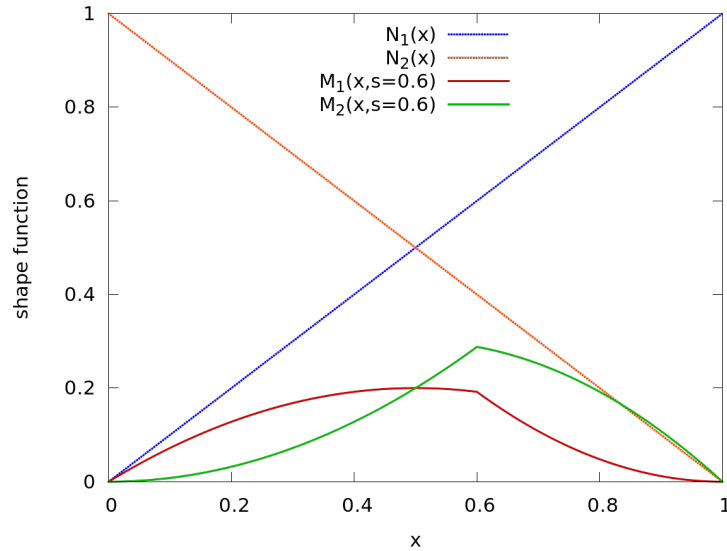


Figure 4.2: Example for shape functions.

ified abs enrichment from (3.34). In Fig. 4.3 multiple shape functions for different positions of the interface are plotted. It can be seen easily that the shape function value for the enrichments is always zero at the nodal points, independent of s . As expected, the symmetry can be observed between the shape functions for a certain parameter s and its counterpart $1 - s$.

At a first glance, it is surprising to see the nonlinear behavior of the shape functions as they were chosen specifically to model linear displacements with a kink. Fig. 4.4 shows the sum of the two shape functions, for the values of s as above.

Obviously, no quadratic terms influence the sum anymore. For the moment it is sufficient to state that if and only if $a_1 = a_2$ holds, the resulting function $u^h(x)$ is piecewise linear with a kink at position s . The interested reader is referred to appendix A.1 where a closer look on the higher order terms in the enhanced abs enrichment is thoroughly discussed.

Coming back to solving the problem with the XFEM. Obviously, the deriva-

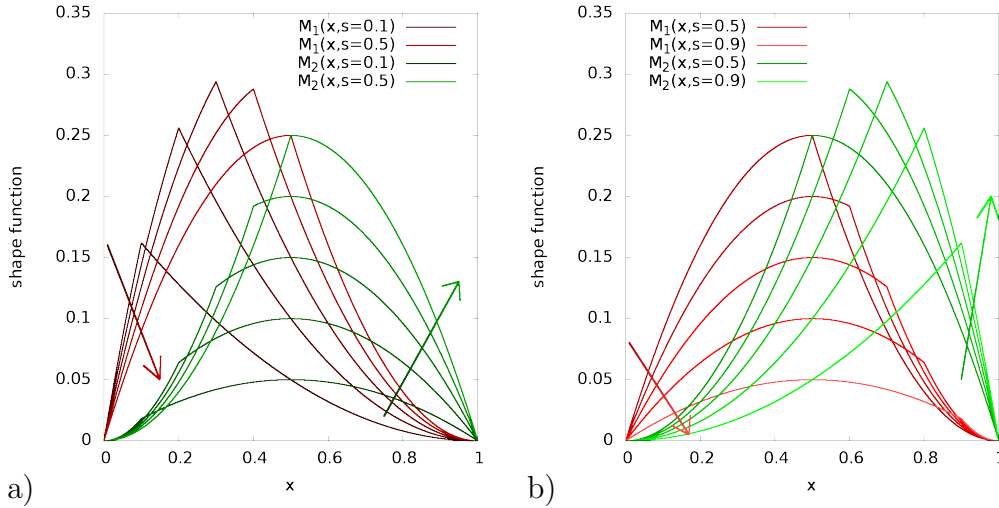


Figure 4.3: Enrichment shape functions (red for M_1 and green for M_2) for different parameters s ,
 a) the red arrow intersects the different shape functions M_1 corresponding to the parameter values $s = 0.1, s = 0.2, \dots, s = 0.5$, the green arrow intersecting the shape functions of M_2 accordingly,
 b) the red arrow intersects the different shape functions M_1 corresponding to $s = 0.5, s = 0.6, \dots, s = 0.9$, the green arrow interesting shape functions M_2 accordingly.

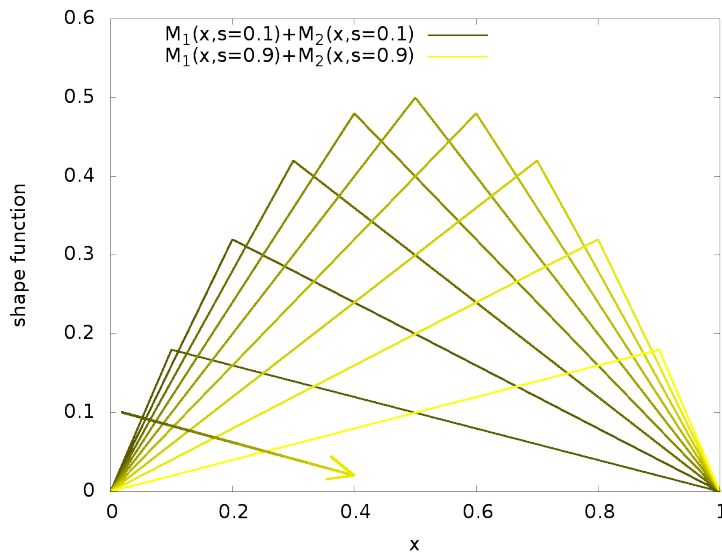


Figure 4.4: Sum of M_1 and M_2 shape functions for different parameter values of s . The arrow intersects the functions corresponding to $s = 0.1, s = 0.2, \dots, s = 0.9$.

tives of the shape functions are needed later, hence they are derived here

$$\begin{aligned}
\partial_x M_1^-(x) &= -2x + 2sx + (1-x)(2-2s) \\
&= (2-2s)(1-2x), \\
\partial_x M_1^+(x) &= -2s + 2sx + (1-x)(-2s) \\
&= -4s(1-x), \\
\partial_x M_2^-(x) &= (2x - 2sx) + x(2-2s) \\
&= 4x(1-s), \\
\partial_x M_2^+(x) &= (2s - 2sx) + x(-2s) \\
&= 2s - 4sx.
\end{aligned} \tag{4.16}$$

The stiffness matrix then is

$$\mathbf{K} = EA^- \int_0^s \partial_x \mathbf{N}^- \otimes \partial_x \mathbf{N}^- dx + EA^+ \int_s^1 \partial_x \mathbf{N}^+ \otimes \partial_x \mathbf{N}^+ dx \tag{4.17}$$

with

$$\partial_x \mathbf{N}^- = \begin{bmatrix} \partial_x N_1 \\ \partial_x N_2 \\ \partial_x M_1^- \\ \partial_x M_2^- \end{bmatrix} = \begin{bmatrix} -1 \\ 1 \\ (2-2s)(1-2x) \\ 4x(1-s) \end{bmatrix} \tag{4.18}$$

and

$$\partial_x \mathbf{N}^+ = \begin{bmatrix} \partial_x N_1 \\ \partial_x N_2 \\ \partial_x M_1^+ \\ \partial_x M_2^+ \end{bmatrix} = \begin{bmatrix} -1 \\ 1 \\ -4s(1-x) \\ 2s - 4sx \end{bmatrix} \tag{4.19}$$

accordingly. Evaluating \mathbf{K} yields for its individual components

$$\begin{aligned}
K_{11} &= K_{22} = sEA^- + (1-s)EA^+, \\
K_{21} &= K_{12} = (s-1)EA^+ - sEA^-, \\
K_{31} &= K_{42} = K_{13} = K_{24} = -2(s-1)^2 s EA^- + 2(s-1)s^2 EA^+, \\
K_{32} &= K_{41} = K_{23} = K_{14} = 2(s-1)s^2 EA^- - 2(s-1)s^2 EA^+, \\
K_{33} &= \frac{4}{3}(s-1)^2 s (4s^2 - 6s + 3) EA^- - \frac{16}{3}(s-1)^3 s^2 EA^+, \\
K_{34} &= K_{43} = -\frac{4}{3}(s-1)^2 s^2 (4s-3) EA^- + \frac{4}{3}(s-1)^2 s^2 (4s-1) EA^+, \\
K_{44} &= \frac{16}{3}(s-1)^2 s^3 EA^- + \frac{4}{3}s^2 (-4s^3 + 6s^2 - 3s + 1) EA^+.
\end{aligned} \tag{4.20}$$

Imposing the DIRICHLET type boundary condition at the left end of the bar

with $u(x = 0) = 0$ and the NEUMANN type boundary condition on the right end of the bar yields

$$\begin{bmatrix} 1 & 0 & 0 & 0 \\ 0 & K_{22} & K_{23} & K_{24} \\ 0 & K_{32} & K_{33} & K_{34} \\ 0 & K_{42} & K_{43} & K_{44} \end{bmatrix} \begin{bmatrix} u_1 \\ u_2 \\ a_1 \\ a_2 \end{bmatrix} = \begin{bmatrix} 0 \\ F \\ 0 \\ 0 \end{bmatrix}, \quad (4.21)$$

which can be written vectorized

$$\mathbf{K}\mathbf{u} = \mathbf{b}. \quad (4.22)$$

It is emphasized that the exact value inputed in K_{11} in order to implement the DIRICHLET type boundary condition $u_1 = 0$ is arbitrary. Any other nonzero value for K_{11} is suitable as well. The exact choice of this parameter changes the resulting eigenvalue and hence may have a negative influence on the condition of matrix \mathbf{K} . Nevertheless, in this trivial example this will not be discussed further.

The solution of (4.22) then reads

$$\mathbf{u} = \begin{bmatrix} u_1 \\ u_2 \\ a_1 \\ a_2 \end{bmatrix} = \begin{bmatrix} 0 \\ -\frac{(sEA^- - EA^- - sEA^+)F}{\frac{EA^-EA^+}{EA^+F - EA^-F} - \frac{2EA^-EA^+}{EA^+F - EA^-F}} \\ \frac{2EA^-EA^+}{EA^+F - EA^-F} \\ \frac{EA^-EA^+}{2EA^-EA^+} \end{bmatrix}. \quad (4.23)$$

As expected $a_1 = a_2$ holds in order to obtain a piecewise linear solution as stated before and explained in appendix A.1. Inserting this into the approximation of the displacement yields for $0 \leq x < s$

$$\begin{aligned} u^-(x) &= N_1(x)u_1 + N_2(x)u_2 + M_1^-(x)a_1 + M_2^-(x)a_2 \\ &= \frac{Fx}{EA^-} \end{aligned} \quad (4.24)$$

and for $s \leq x \leq 1$

$$\begin{aligned} u^+(x) &= N_1(x)u_1 + N_2(x)u_2 + M_1^+(x)a_1 + M_2^+(x)a_2 \\ &= \frac{F}{EA^-}s + \frac{F}{EA^+}(x - s) \end{aligned} \quad (4.25)$$

which coincides with the analytical solution.

4.1.2 Eigenvalue analysis

The same result as in the previous section can be obtained with the standard finite element method without enrichments, if and only if at least two linear elements are used to discretize this one-dimensional bar. In this case the two (or more) elements must separate the total volume precisely at position s , otherwise the analytical solution can not be reproduced exactly. Hence, the mesh must be fine enough to resolve the length parameter

$$\hat{h} = \min(s, 1 - s). \quad (4.26)$$

Without becoming specific, this parameter \hat{h} plays a similar role as mesh parameter h for a quasi-uniform mesh. It is known for quasi-uniform meshes (see for example [Brenner and Scott, 2008]) that the condition number κ of the global stiffness matrix is of order $\mathcal{O}(h^{-2})$. Hence, when the interface is close to a node, that is parameter s is either close to 1 or close to 0, the problem becomes ill-posed with quadratic order.

As pointed out in [Fries and Belytschko, 2010], the XFEM basis functions for the enrichments become “almost linear dependent” in case of nodal level set values close to zero. A more precise analysis of this relation between small absolute nodal level set values and the condition of the global stiffness matrix has - to the authors knowledge - not been published anywhere. Hence, a closer look on the influence of the exact value of the parameter s on the condition of the stiffness matrix \mathbf{K} in (4.22) follows.

As previously stated, one eigenvalue corresponds directly to the exact choice of implementing the DIRICHLET type boundary condition. The other three eigenvalues are the eigenvalues of the sub-matrix

$$\mathbf{K}_{\text{sub}} = \begin{bmatrix} K_{22} & K_{23} & K_{24} \\ K_{32} & K_{33} & K_{34} \\ K_{42} & K_{43} & K_{44} \end{bmatrix}. \quad (4.27)$$

In order to simplify this computation, EA^+ is expressed with the help of a parameter c describing the contrast between EA^- and EA^+

$$EA^+ = cEA^-. \quad (4.28)$$

Thus, \mathbf{K}_{sub} can then be simplified to

$$\mathbf{K}_{\text{sub}} = EA^- \begin{bmatrix} \tilde{K}_{22} & \tilde{K}_{23} & \tilde{K}_{24} \\ \tilde{K}_{32} & \tilde{K}_{33} & \tilde{K}_{34} \\ \tilde{K}_{42} & \tilde{K}_{43} & \tilde{K}_{44} \end{bmatrix} \quad (4.29)$$

with

$$\begin{aligned}
 \tilde{K}_{22} &= s + (1 - s)c, \\
 \tilde{K}_{32} = \tilde{K}_{42} = K_{23} = \tilde{K}_{24} &= (s^2 - s)(1 - c), \\
 \tilde{K}_{33} = \tilde{K}_{44} &= \left(\frac{4s^3}{3} - 2s^2 + s\right)(1 - c) + \frac{c}{3}, \\
 \tilde{K}_{34} = \tilde{K}_{43} &= \frac{2s^3}{3} - 2s^2 + s + \left(-\frac{2s^3}{3} + s - \frac{1}{3}\right)c.
 \end{aligned} \tag{4.30}$$

It becomes immediately apparent that all eigenvalues scale with EA^- and hence the condition of the matrix does not depend on the absolute values of the material parameters EA^- and EA^+ . Solely the contrast between the two has an influence on the condition, therefore $EA^- = 1$ is assumed. With the help of a computer algebra system, the resulting three eigenvalues, depending on the parameter s and contrast c can be computed.

All three roots of the characteristic polynomial are real numbers as the originating matrix \mathbf{K}_{sub} is symmetric and therefore has real eigenvalues (cf. for example [Bronstein et al., 2001]).

In the following, the eigenvalues $\lambda_i(s)$, $i = 1, 2, 3$ depending on the parameter s describing the position of the interface and the parameter c describing the contrast will be analyzed.

As already discussed in section 3.2, it is known from literature (cf. [Fries and Belytschko, 2010]) that XFEM is not able to handle cases where the level set value at a node of the finite element mesh is equal to zero when considering bimaterial problems. In this example, this occurs if the parameter s equals either 0 or 1. Looking at the eigenvalues for these two cases

$$\lambda_1(0, c) = 0, \tag{4.31}$$

$$\lambda_1(1, c) = 0, \tag{4.32}$$

$$\lambda_2(0, c) = 0, \tag{4.33}$$

$$\lambda_2(1, c) = 0, \tag{4.34}$$

$$\lambda_3(0, c) = 1, \tag{4.35}$$

$$\lambda_3(1, c) = c, \tag{4.36}$$

confirms this problem. As expected the stiffness matrix \mathbf{K} is singular in both cases. To get a better impression of the eigenvalues, Fig. 4.5 – Fig. 4.7 show the influence of the contrast on the three eigenvalues as a function of parameter s .

Obviously, for all three eigenvalues the contrast influences the shape of the curves, especially the maximum values vary significantly with the contrast. Nevertheless, it does not influence the minimum values of the curves. It

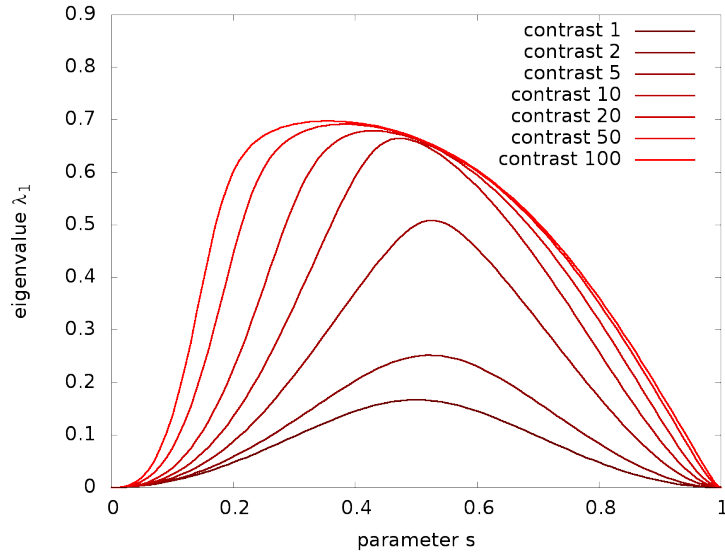


Figure 4.5: Eigenvalue λ_1 over parameter s for different contrasts.

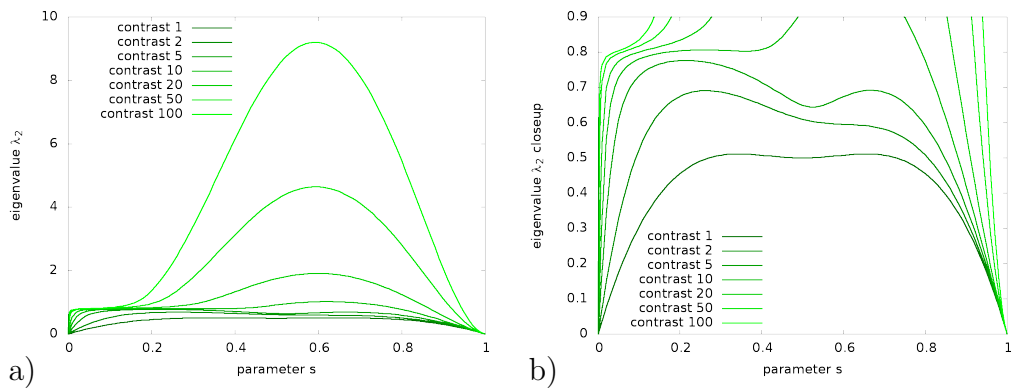


Figure 4.6: Eigenvalue λ_2 over parameter s for different contrasts c , where b) shows a closeup of a).

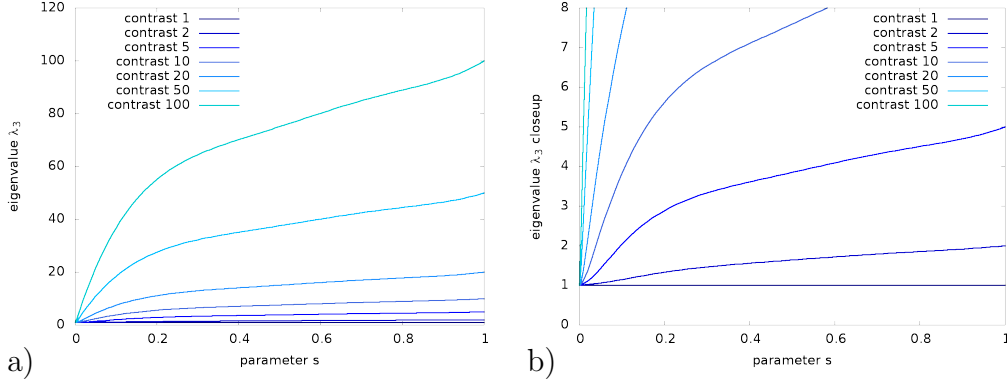


Figure 4.7: Eigenvalue λ_3 over parameter s for different contrasts c , where b) shows a closeup of a).

strikes that λ_3 dominates the other two values for all $s \in [0, 1]$ for every specific contrast in this analysis. Especially, the fact is important that for $s \approx 0$ and $s \approx 1$ the eigenvalues λ_1 and λ_2 are close to zero. This is because for these values the condition of the stiffness matrix \mathbf{K} becomes large.

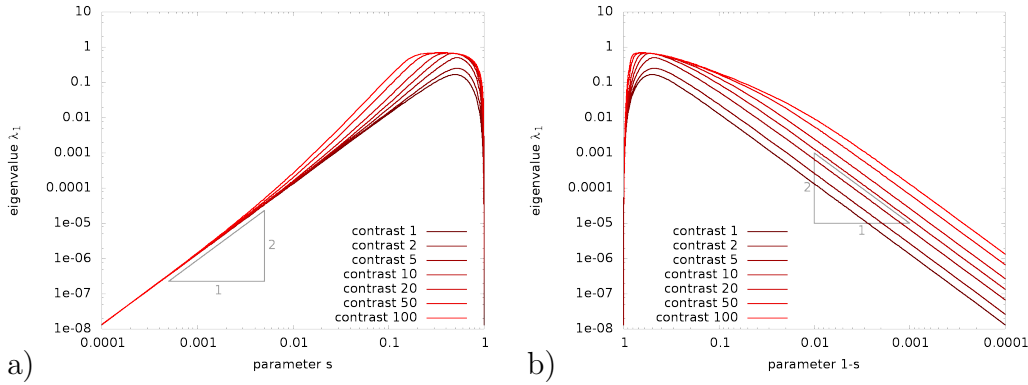


Figure 4.8: Log-log plot of eigenvalue λ_1 over parameter s for different contrasts c , where a) shows a standard log-log plot for parameter s , b) log-log plot with a mirrored x-axis for parameter $1 - s$.

Fig. 4.8 – Fig. 4.10 now show log-log plots of all three eigenvalues that allow a better analysis of the behavior of the eigenvalues when the parameter s is close to zero and close to one. The log-log plots displayed in Fig. 4.8 b) – Fig. 4.10 b) with a mirrored x -axis for parameter $1 - s$ allow to analyze the region of s being close to 1. In all cases it becomes apparent, that the change in the largest eigenvalue λ_3 is of order $\mathcal{O}(\hat{h}^0)$ for s being close to either side.

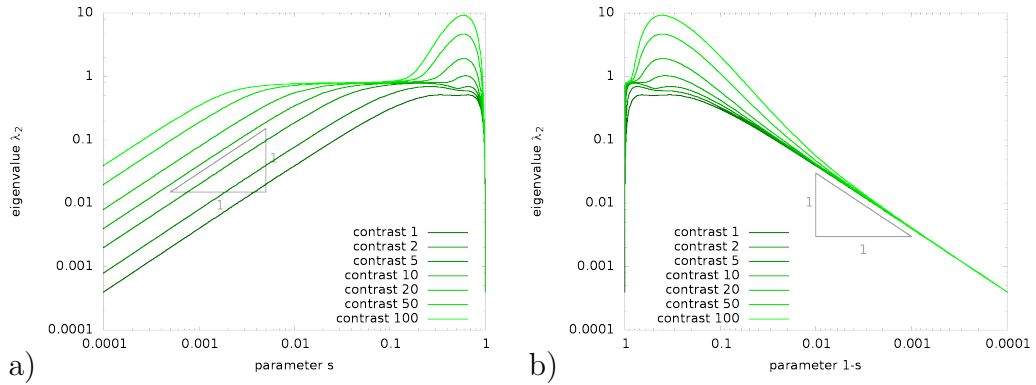


Figure 4.9: Log-log plot of eigenvalue λ_2 over parameter s for different contrasts c , where a) shows a standard log-log plot for parameter s , b) log-log plot with a mirrored x-axis for parameter $1 - s$.

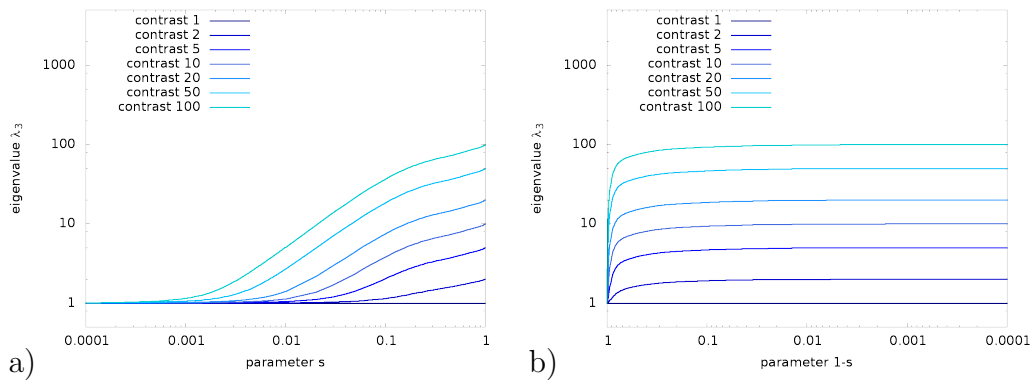


Figure 4.10: Log-log plot of eigenvalue λ_3 over parameter s for different contrasts c , where a) shows standard log-log plot for parameter s , b) log-log plot with a mirrored x-axis for parameter $1 - s$.

The change in the eigenvalue λ_2 is of order $\mathcal{O}(\hat{h}^{-1})$ for \hat{h} being close to zero, that is s being close to zero or one. The change in the smallest eigenvalue λ_1 is of order $\mathcal{O}(\hat{h}^{-2})$ for the parameter s being close to the bounds.

Putting these observations together yields that κ of the enriched global stiffness matrix \mathbf{K} is of order $\mathcal{O}(\hat{h}^{-2})$ as it is the quotient of the largest and the smallest eigenvalue which is in this example

$$\kappa(\mathbf{K}) = \frac{\lambda_3}{\lambda_1}, \tag{4.37}$$

where of course the DIRICHLET type boundary conditions are imposed in such a way that the resulting eigenvalue has no influence on the condition of \mathbf{K} as stated before.

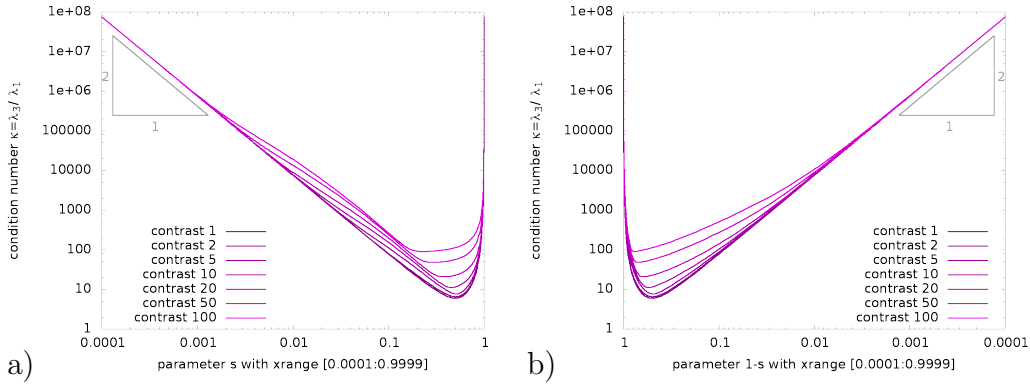


Figure 4.11: Log-log plot of $\kappa(\mathbf{K}) = \lambda_3/\lambda_1$ over parameter s for different contrasts c , where a) shows a standard log-log plot for parameter s , b) log-log plot with a mirrored x-axis for parameter $1 - s$.

Fig. 4.11 affirms the previous statement that \mathbf{K} is of order $\mathcal{O}(\hat{h}^{-2})$. Additionally, it shows that in case of the parameter s being close to the position of a node, that is $s \approx 0$ or $s \approx 1$, the bad condition of the stiffness matrix is independent of the material contrast.

4.2 Eigenvalue analysis for XFEM in 3D

The main result of section 4.1.2 was that in a simple one-dimensional example the condition of the enriched local stiffness matrix is of order $\mathcal{O}(\hat{h}^{-2})$ with the parameter s describing the minimal distance of a node to the interface. This section gives a detailed analysis of the eigenvalues of the global stiffness matrix for a simple three-dimensional example.

The setting for this example is a three-dimensional cube $\Omega = [0, 1] \times [0, 1] \times [0, 1]$ consisting of two materials Ω_M and Ω_I separated by a planar interface Γ parallel to the y - z -plane. The corresponding level set function then reads

$$\Phi : \Omega \subset \mathbb{R}^3 \rightarrow \mathbb{R} ; \Phi(\mathbf{x}) = s - x \quad (4.38)$$

with position parameter $s \in (0, 1)$. For all points $\mathbf{x} \in \Omega$ it holds that

$$\mathbf{x} \in \Omega_I \Leftrightarrow \Phi(\mathbf{x}) < 0, \quad (4.39)$$

$$\mathbf{x} \in \Gamma \Leftrightarrow \Phi(\mathbf{x}) = 0, \quad (4.40)$$

$$\mathbf{x} \in \Omega_M \Leftrightarrow \Phi(\mathbf{x}) > 0. \quad (4.41)$$

Isotropic linear elastic behavior is assumed for both materials and the material parameters read

$$E_M = 1 \text{ MPa}, E_I = 10 \text{ MPa and } \nu_M = \nu_I = 0.3. \quad (4.42)$$

As boundary conditions the following DIRICHLET type boundary conditions have been chosen

$$\begin{aligned} \mathbf{x} \in \{ 0 \times [0, 1] \times [0, 1] \} &\Rightarrow u_1 = 0, \\ \mathbf{x} \in \{ 1 \times [0, 1] \times [0, 1] \} &\Rightarrow u_1 = 0.2, \\ \mathbf{x} \in \{ [0, 1] \times 0 \times [0, 1] \} &\Rightarrow u_2 = 0, \\ \mathbf{x} \in \{ [0, 1] \times 1 \times [0, 1] \} &\Rightarrow u_2 = 0, \\ \mathbf{x} \in \{ [0, 1] \times [0, 1] \times 0 \} &\Rightarrow u_3 = 0, \\ \mathbf{x} \in \{ [0, 1] \times [0, 1] \times 1 \} &\Rightarrow u_3 = 0, \end{aligned} \quad (4.43)$$

which corresponds to uniaxial tensile loading with 20% strain. It has been stated in subsection 2.1.2 that this work restricts itself to the theory of small strains which obviously is not the case using these boundary conditions. Nevertheless, as a linear elastic material law is applied to both materials, a larger deformation does not contradict any of the previous statements.

The standard FEM is able to solve this type of problem, if the underlying mesh resolves the planar interface precisely. This already is the case when using two hexahedral elements for example. If the interface is not resolved by the underlying mesh FEM will not be able to produce the exact solution, but XFEM is (assuming the resulting linear system is not singular due to nodal level set values equal to zero).

In this section the focus does not lie on the exact solution but on the eigenvalues of the corresponding global stiffness matrix with respect to the position parameter s and the corresponding minimal distance between nodes and the

interface. In order to exclude boundary effects from the analysis a nontrivial mesh has been chosen. The underlying mesh is a regular tetrahedral mesh created from a voxelized image with mesh parameter $h = 0.1$ which results in 5000 elements and $11 \times 11 \times 11$ nodes. If the interface is not resolved by the mesh, exactly 500 elements are intersected by the interface and $2 \times 11 \times 11$ nodes are enriched. Taking into account the three spacial dimensions this results in the XFEM problem having 4719 degrees of freedom of which 726 correspond to enrichment degrees of freedom.

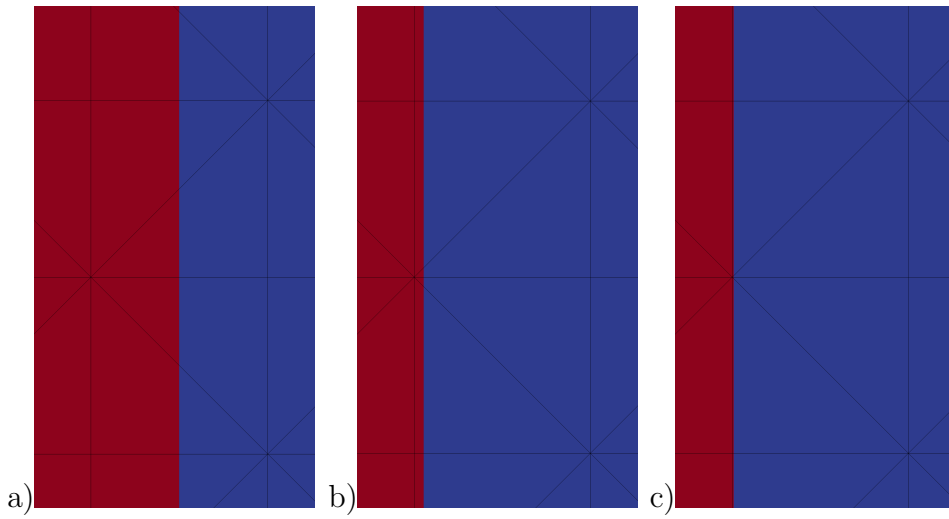


Figure 4.12: Position of interface in mesh for a) position parameter s_1 , b) position parameter s_2 , c) position parameter s_3 .

The analysis of three different position parameters s is explained in detail. They are $s_1 = 0.55$, $s_2 = 0.505$ and $s_3 = 0.5005$ as it is shown in Fig. 4.12. The first, s_1 is set in the middle between the two layers of enriched nodes, that is $\{0.5 \times [0, 1] \times [0, 1]\}$ and $\{0.6 \times [0, 1] \times [0, 1]\}$. The second position parameter is chosen such that the closest distance from the interface to enriched nodes is reduced by the factor $1/10$ which results in $s_2 = 0.505$. The same procedure is applied to achieve the third position parameter $s_3 = 0.5005$. Special emphasis is laid on the example being chosen such that at each element intersected by the interface, there are exactly two different level set values. For parameter s_1 these two read 0.05 and -0.05 , for parameter s_2 they are 0.005 and -0.095 and for parameter s_3 they read 0.0005 and -0.0995 . This is the case for every single element intersected by the interface! Hence, even though the different tetrahedrons in the finite element mesh are aligned in different ways with respect to the interface, there are only three different scenarios for the exact alignment. This is either one or two or three nodes of

each tetrahedron have the smaller of the two level set values. This is done in order to reduce the variety of different intersection scenarios one typically obtains when analyzing three-dimensional problems.

For a better understanding of the following figures, the reader is reminded of the block structure of the global stiffness matrix when using a separated ordering of the unknowns. The upper left part of the stiffness matrix corresponds to the standard degrees of freedom and the lower right part corresponds to the enrichment degrees of freedom.

Assume a standard FEM analysis of the same problem with special treatment of the elements intersected by the interface and the normal material parameters for the elements not intersecting the interface. If the material parameters for the intersected elements were the average of the material parameters of Ω_I and Ω_M according to the volumetric percentage of the two in each intersected element, the resulting global stiffness matrix would be exactly the same as the previously mentioned upper left submatrix of the XFEM stiffness matrix.

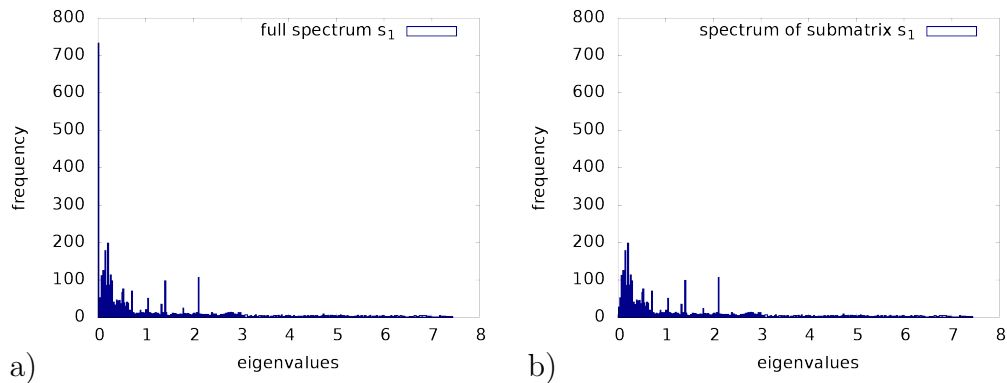


Figure 4.13: Spectrum of stiffness matrix for position parameter s_1 , a) spectrum of the full stiffness matrix, b) spectrum of the submatrix corresponding to standard degrees of freedom.

The main result of Fig. 4.13 is that obviously from left to right more than 700 very small eigenvalues have vanished. Rescaling the data range results in Fig. 4.14.

The two images in in Fig. 4.14 are almost identical. The 726 enrichment degrees of freedom seem to influence the spectrum of the global stiffness matrix on its lower end solely. The same holds true for the position parameters s_2 and s_3 .

The images in Fig. 4.15 show the same data range and it becomes apparent that a changing position parameter s indeed does change the spectrum of the

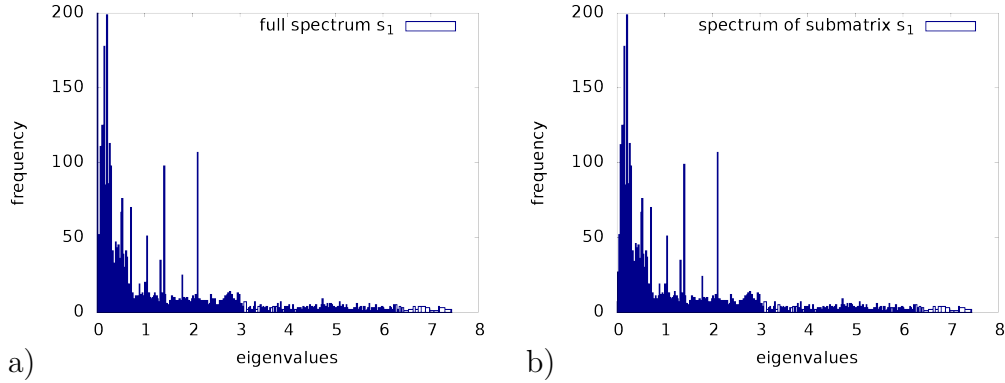


Figure 4.14: Spectrum of stiffness matrix for position parameter s_1 with rescaled data range, a) spectrum of the full stiffness matrix, b) spectrum of the submatrix corresponding to standard degrees of freedom.

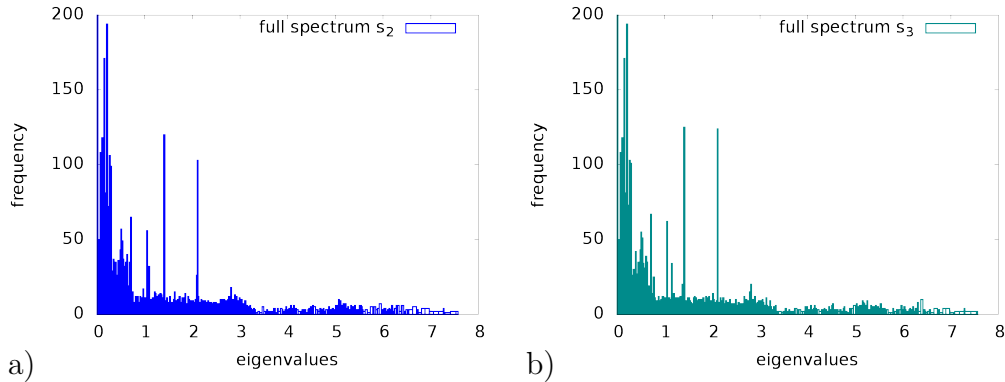


Figure 4.15: Spectrum of stiffness matrix, a) spectrum for position parameter s_2 , b) spectrum for position parameter s_3 .

standard part the stiffness matrix but not in a significant way. The largest eigenvalues for the three different position parameters read $\lambda_{\max}^{s_1} = 7.42$, $\lambda_{\max}^{s_2} = 7.54$ and $\lambda_{\max}^{s_3} = 7.56$.

A look at the lower end of the spectrum of the stiffness matrices reveals that the smallest eigenvalue for position parameter s_1 reads $\lambda_{\min}^{s_1} = 7.87 \cdot 10^{-5}$ and the majority of the small eigenvalues are of order 10^{-5} to 10^{-4} as can be seen in Fig. 4.16.

The smallest eigenvalue for position parameter s_2 reads $\lambda_{\min}^{s_2} = 4.59 \cdot 10^{-6}$ and the majority of the small eigenvalues are of order 10^{-6} to 10^{-5} . They are plotted in Fig. 4.17.

Fig. 4.18 shows the lower end of the spectrum of the stiffness matrix for

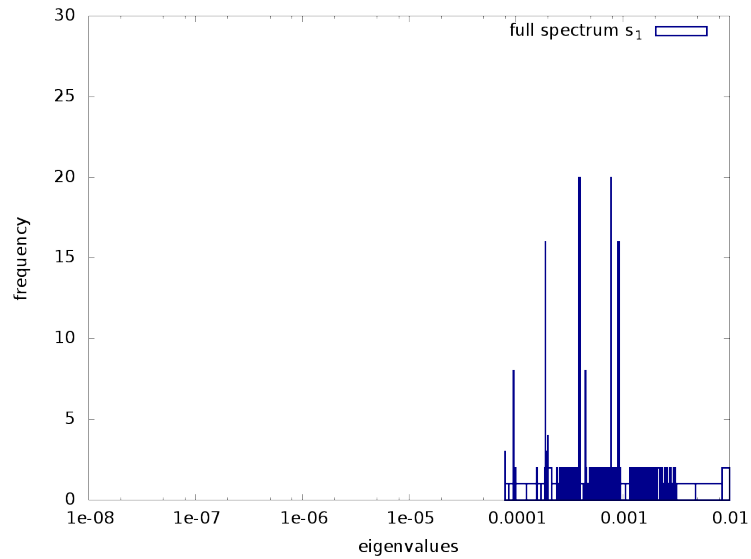


Figure 4.16: Lower end of spectrum of stiffness matrix for position parameter s_1 .

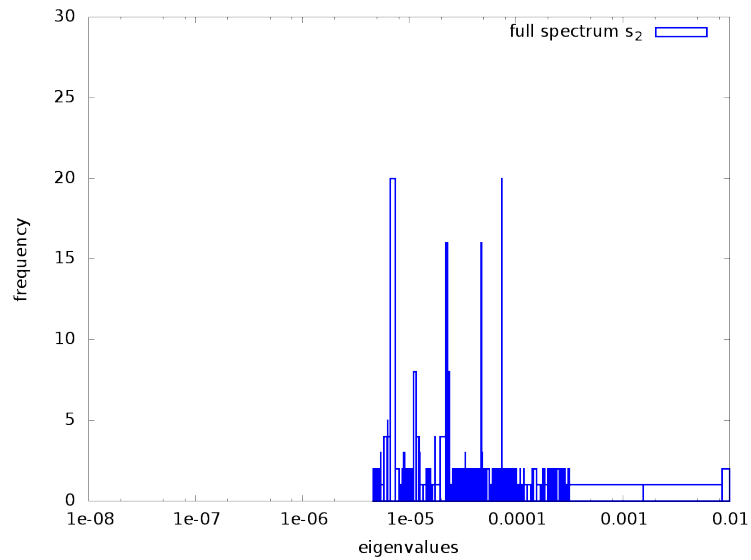


Figure 4.17: Lower end of spectrum of stiffness matrix for position parameter s_2 .

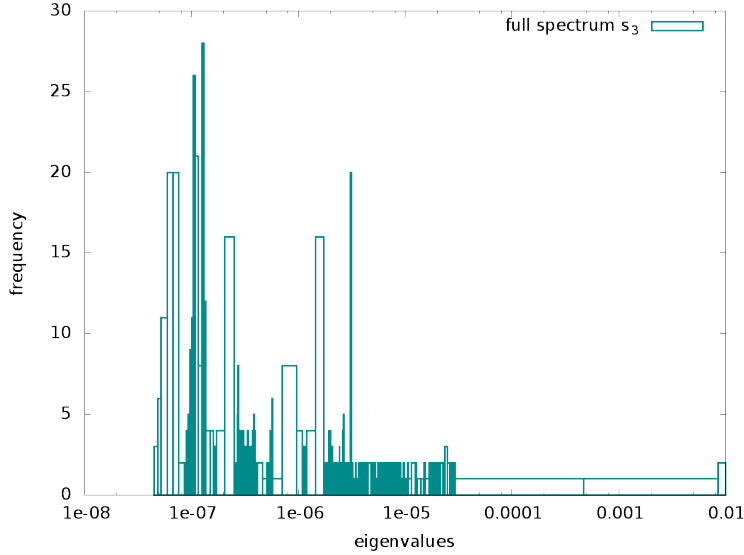


Figure 4.18: Lower end of spectrum of stiffness matrix for position parameter s_3 .

position parameter s_3 . The smallest eigenvalue reads $\lambda_{\min}^{s_3} = 4.82 \cdot 10^{-8}$ and the majority of the small eigenvalues are of order 10^{-8} to 10^{-6} .

Summarizing the largest eigenvalues and the smallest eigenvalues of the global stiffness matrix for the three different position parameters and therewith the condition of the global stiffness matrix is depicted in Table 4.1. The

| position parameter s | $s_1 = 0.55$ | $s_2 = 0.505$ | $s_3 = 0.5005$ |
|------------------------|----------------------|----------------------|----------------------|
| λ_{\min} | $7.87 \cdot 10^{-5}$ | $4.59 \cdot 10^{-6}$ | $4.82 \cdot 10^{-8}$ |
| λ_{\max} | 7.42 | 7.54 | 7.56 |
| κ | $9.44 \cdot 10^4$ | $1.64 \cdot 10^6$ | $1.57 \cdot 10^8$ |

Table 4.1: Condition of the global stiffness matrix for different position parameters s .

main result of this analysis is, that the smallest eigenvalue of the global stiffness matrix depends directly on the smallest distance between an enriched node and the interface. The magnitude of the smallest eigenvalue seems to depend quadratic on this smallest distance which agrees well with the findings of section 4.1.2.

4.3 Comparison XFEM vs FEM - spherical inclusion

After identifying possible problems due to ill-conditioning of the XFEM in sections 4.1.2 and 4.2, this section provides some findings on computational errors of XFEM compared to FEM. In [Eshelby, 1957] some fundamental analytical solutions for the case are derived where a given material is infinitely extended and has a single ellipsoidal inhomogeneity. This section uses these findings to obtain analytical solutions for a spherical inclusion in a finite domain so that it is possible to measure the absolute error of the FE simulation results. The findings of this section have already been published in [Zangmeister et al., 2013].

4.3.1 Analytical solution

Consider a classical ESHELBY problem (cf. [Eshelby, 1957]) with an infinitely extended material Ω that has a single spherical inclusion Ω_I . Let both materials have the same POISSON'S ratio $\nu = \nu_M = \nu_I$. The bulk modulus of the inclusion is denoted with K_I and the bulk modulus of the surrounding matrix with K_M . At infinity the strain $\boldsymbol{\varepsilon}^0 = \epsilon \mathbf{I}$ is applied, where \mathbf{I} denotes the identity tensor. It is a strain field without a deviatoric part. The corresponding equivalent eigenstrain $\boldsymbol{\varepsilon}^*$ in the spherical inclusion is (cf. [Mura, 1987])

$$\boldsymbol{\varepsilon}^* = \frac{(K_I - K_M) \text{tr}(\boldsymbol{\varepsilon}^0)(1 - \nu)}{(4\nu - 2)K_M - (1 + \nu)K_I} \mathbf{I}. \quad (4.44)$$

Consider the material parameters

$$E_M = 1 \text{ MPa}, \quad E_I = 10 \text{ MPa} \text{ and } \nu_M = \nu_I = 0.3, \quad (4.45)$$

which lead to

$$K_M = 5/6 \text{ MPa} \text{ and } K_I = 25/3 \text{ MPa}. \quad (4.46)$$

Additionally, let $\epsilon = 0.01$. Inserting these parameters into (4.44) yields

$$\boldsymbol{\varepsilon}^* = \frac{3(K_I - K_M)\epsilon(1 - \nu)}{(4\nu - 2)K_M - (1 + \nu)K_I} \mathbf{I} = -\frac{63}{4600} \mathbf{I} \quad (4.47)$$

as the equivalent eigenstrain in Ω_I for an equivalent homogeneous material. As this strain $\boldsymbol{\varepsilon}^*$ is purely volumetric another result from Eshelby (cf. [Eshelby, 1957], [Mura, 1987]) can be used. The radial displacement in this

equivalent inclusion problem is

$$u_r = \frac{1 + \nu}{1 - \nu} \frac{1}{r^2} \int_0^r \epsilon^* \xi^2 d\xi, \quad (4.48)$$

where r is the distance from the center of the sphere and ϵ^* denotes the radial component of the volumetric strain ϵ^* . Denoting the radius of the sphere with a , (4.48) becomes for $r > a$

$$u_r = \frac{1 + \nu}{1 - \nu} \frac{1}{r^2} \left(\int_0^a \epsilon^* \xi^2 d\xi + \int_a^r 0 d\xi \right) = -\frac{39a^3}{4600r^2}, \quad (4.49)$$

as the equivalent eigenstrain vanishes outside of the sphere.

Now consider a spherical inclusion in a finite volume Ω , a cube with a sphere Ω_I in its center. Let the diameter of the sphere be $l = 2a$, which is half of the length of the cube. When superimposing this equivalent eigenstrain

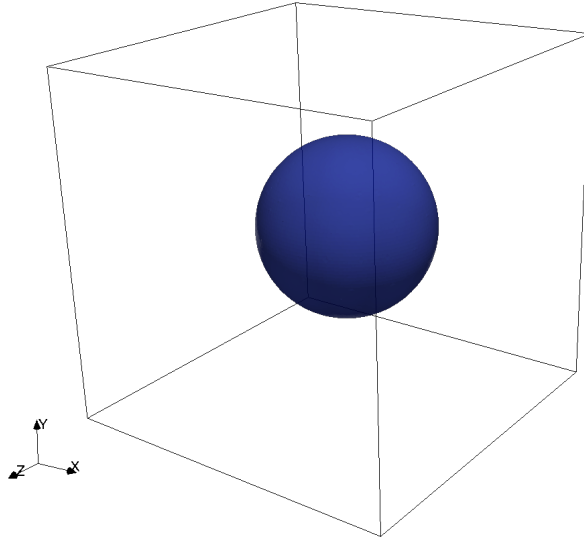


Figure 4.19: Spherical inclusion in standard RVE.

with the applied strain at infinity ϵ^0 , (4.49) provides the possibility to specify displacement boundary conditions on the geometry shown in Fig. 4.19 such that the strain field is equal to the strain field in the vicinity of the sphere in the infinitely extended material described earlier. Thus, for any $\mathbf{x} \in \Omega$ with

a distance r from the center of the sphere, the radial displacement equals

$$u_r(\mathbf{x}) = \begin{cases} r\epsilon - \frac{39r}{4600}, & \mathbf{x} \in \Omega_I \\ r\epsilon - \frac{39l^3}{36800r^2}, & \mathbf{x} \in \Omega \setminus \Omega_I. \end{cases} \quad (4.50)$$

When imposing this radial displacement everywhere on the boundary $\partial\Omega$ of the representative volume element (RVE) as visualized in Fig. 4.19, the radial strain in Ω_I is

$$\varepsilon_r = \frac{1 + \nu}{3(1 - \nu)}\epsilon^* + \epsilon \approx 0.00152174 \quad (4.51)$$

and

$$\varepsilon_r = -\frac{2(1 + \nu)}{3(1 - \nu)}\frac{a^3}{r^3}\epsilon^* + \epsilon \approx 0.0169565\frac{a^3}{r^3} + 0.01 \quad (4.52)$$

in $\Omega \setminus \Omega_I$. Fig. 4.20 shows a plot of the analytical solution for the radial strain ε_r across the material interface. As already stated, the radial strain within the sphere is constant, at the material interface there is a jump, and in the matrix the radial strain decays proportional to r^{-3} . The underlying

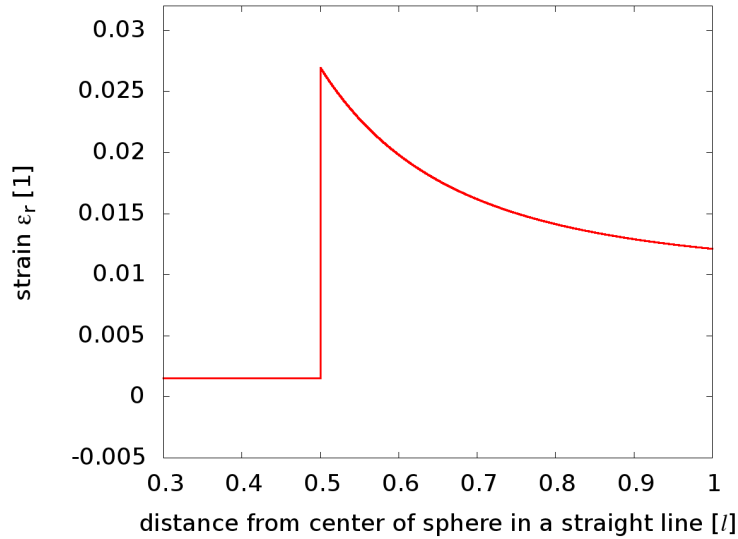


Figure 4.20: Analytical solution for radial strain.

mesh is a regular tetrahedral mesh, created from a voxelized image of the sphere discretized with four different mesh parameters $h_1 = 2^{-3}l$, $h_2 = 2^{-4}l$, $h_3 = 2^{-5}l$ and $h_4 = 2^{-6}l$. The mesh corresponding to h_1 consists of 16^3 voxels, h_2 corresponds to 32^3 voxels, h_3 corresponds to 64^3 voxels and h_4 corresponds to 128^3 voxels. In Fig. 4.21 cross sections from the meshes with

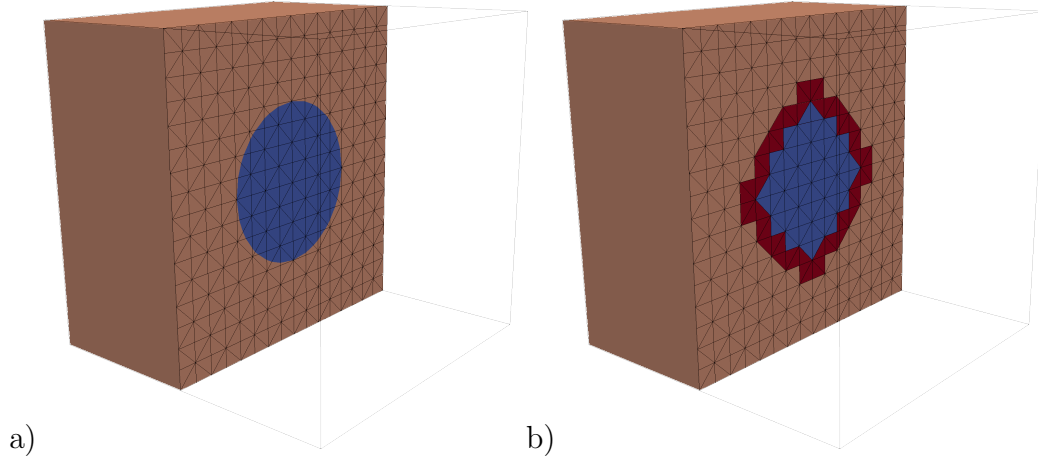


Figure 4.21: Discretization example for XFEM and standard FEM on mesh with $h_1 = 2^{-3}l$.

mesh parameter $h_1 = 2^{-3}l$ are shown. Fig. 4.21 a) displays the mesh used for both standard FEM and XFEM. The material colors are set according to the level set function. It can be seen that the material interface does not coincide with element faces. In Fig. 4.21 b) the elements containing the material interface are colored in dark red. These are the elements which need the extra enrichment for the XFEM and hence defines the set $\bar{\mathcal{N}}_{h_1}^*$ introduced in 3.31. $\bar{\mathcal{N}}_{h_1}^*$ is the set of all nodes attached to at least one element which is intersected by the material interface for mesh parameter h_1 . Obviously, when computing the stiffness matrix from 3.30, the local elasticity tensor depends on the material. Hence, when integrating 3.23 in the elements containing the interface, special emphasis has to be put on the local elasticity tensor. In this work this has been taken care of by splitting up the interface elements into sub-tetrahedrons for the numerical integration. This is done according to the underlying level set function with linear shape functions. That is, the level set values are evaluated exactly at each grid point of the underlying mesh and approximated linearly in between. The sphere shown in Fig. 4.21 is plotted according to these linear approximation of the level set function.

The interface elements are either split into four or six sub-tetrahedrons, depending on how the four nodes of the element are separated into the two material phases as described in section 3.2. As for the standard FEM approach linear shape functions for the finite element mesh were chosen, one Gauß point per sub-tetrahedron is required. For the XFEM with linear shape functions, quadratic terms occur as explained in detail in section 3.2 and appendix A.1. Hence, the numerical integration has to be performed with a

four point Gauß quadrature rule per sub-tetrahedron for an exact integration of the approximated functions, again as described in section 3.2.

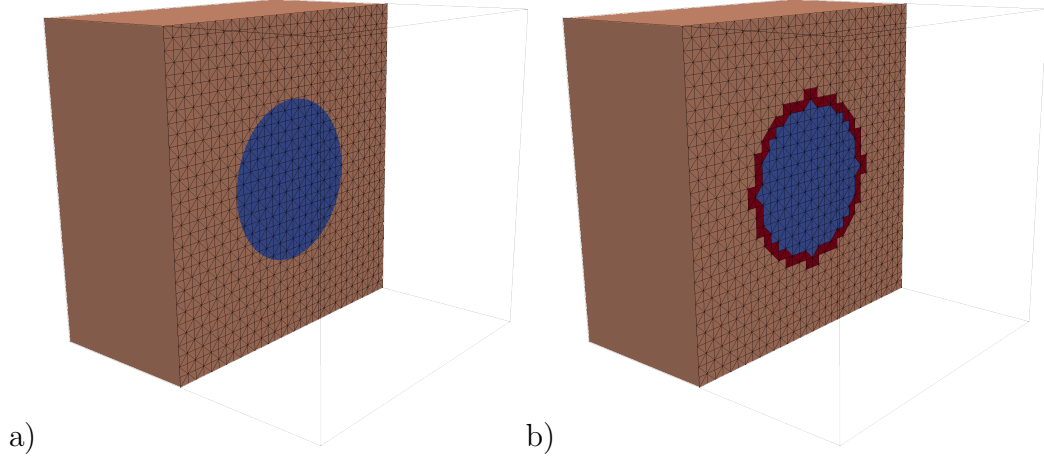


Figure 4.22: Discretization example for XFEM and standard FEM on mesh with $h_2 = 2^{-4}l$.

Fig. 4.22 shows the same geometry as in Fig. 4.21, but discretized with a different mesh parameter $h_2 = 2^{-4}l$. It strikes that the number of interface elements increase. It is also obvious that it does not increase as fast as the total number of elements in the mesh does, compared to Fig. 4.21. The exact figures of the computational effort created by the enriching technique is summarized in Table 4.2.

| Mesh parameter h | $2^{-3}l$ | $2^{-4}l$ | $2^{-5}l$ | $2^{-6}l$ |
|--------------------------|-----------|-----------|-----------|------------|
| No. of elements | 20,480 | 163,840 | 1,310,720 | 10,485,760 |
| No. of enriched elements | 1,160 | 4,472 | 18,236 | 73,652 |
| No. of nodes | 4,913 | 35,937 | 274,625 | 2,146,689 |
| No. of enriched nodes | 436 | 1,660 | 6,744 | 27,216 |
| No. of Gauß points FEM | 25,284 | 182,930 | 1,388,617 | 10,800,411 |
| No. of Gauß points XFEM | 39,696 | 240,200 | 1,622,308 | 11,744,364 |

Table 4.2: Number of elements, nodes and Gauß points for different mesh parameters h .

4.3.2 Simulation results

As stated before, the simulations described in the following have all been computed with FeelMath (Finite Elements for Elastic MATerials and Homog-

enization) an in-house software project at Fraunhofer ITWM (cf. [FeelMath, 2014]).

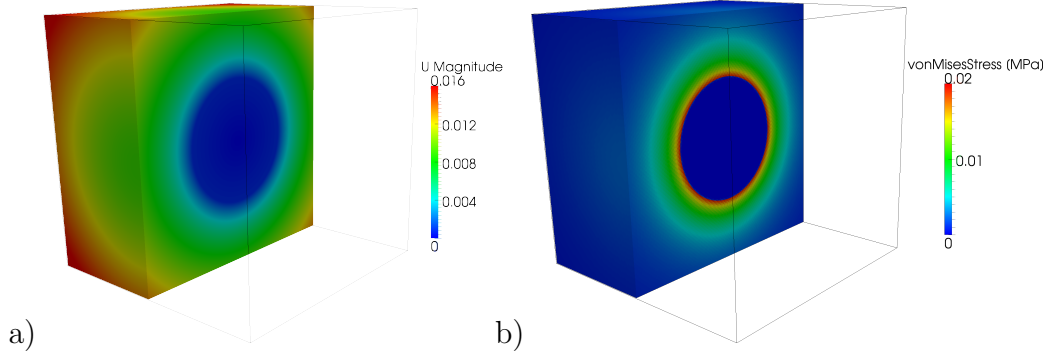


Figure 4.23: Simulation results for XFEM with mesh parameter $h_4 = 2^{-6}l$: a) displacement field and b) VON MISES equivalent stress in MPa.

Fig. 4.23 shows the magnitude of the displacement field and the VON MISES equivalent stress σ_v for one of the simulations. The VON MISES equivalent stress is defined as $\sigma_v = \sqrt{3J_2}$ with J_2 the second invariant of the stress deviator (cf. [Wriggers, 2001]). As the imposed displacement boundary conditions correspond to a purely radial strain, it is not surprising to find the solution being a radial displacement field. It was stated in the previous section that the strain in the spherical inclusion is constant and its deviatoric part is equal to $\mathbf{0}$. Hence, the VON MISES equivalent stress σ_v inside the spherical inclusion must equal zero, which is recovered in the simulation. The jump in the stress field across the material interface is quite pronounced in Fig. 4.23. Nevertheless, the focus of this work is on the correct approximation of the jump in the strain field and the accuracy with regard to the analytical solution. In order to do so, the strain tensor along different orientations is analyzed. The origin of all lines is the center of the sphere and they reach out in different angles. Along each line the normal component of the strain is analyzed.

Fig. 4.24 shows some of these lines in a 2D cross section of the 3D volume. Due to symmetry reasons only one-eighth of the volume is analyzed. The orientation of each line is described by two angles. Analogously to standard spherical coordinates, the first angle describes the angle in the x - y -plane (polar angle), the second angle denotes the angle in the x - z -plane (azimuthal angle). For both angles a step-size of 15° has been chosen such that for one-eighths of the sphere, 43 different lines have been analyzed. These lines can be imagined as rays starting from the center of the sphere and passing through the whole volume. Fig. 4.25 – Fig. 4.28 plot the normal component of the

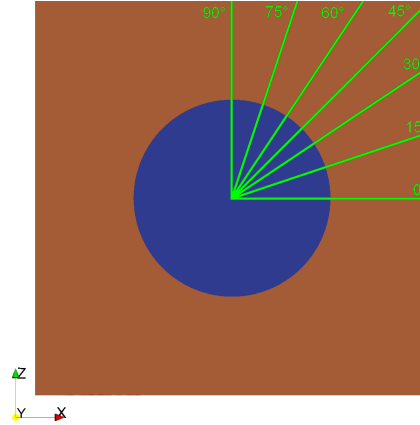


Figure 4.24: Visualization of different lines in a 2D cross section.

strain tensor along such lines over the distance to the center of the sphere. Tetrahedrons with linear shape functions (with and without XFEM enrichments) are chosen as the base elements of the finite element mesh. Hence, the solution for the strains is constant in each element. In the following plots, XFEM results are always plotted with 'x' tick-marks and standard FEM with 'o'. The tick-marks along these lines have been set at each beginning of a new element intersected by the line.

The first example corresponds to x - z -angle= 0° and x - y -angle= 15° and therefore resembles the line that is tilted by 0° away from the x axis in the x - z -plane and 15° in the x - y -plane, respectively.

In Fig. 4.25 and Fig. 4.26 it can be seen, that the analytical solution is approximated well. In both cases (similar to every single other case analyzed in this study) the radial strain within the spherical inclusion is reproduced more or less exactly. The jump at the interface is approximated rather well. Not surprisingly the standard FEM is not reproducing the exact jump but underestimating it. This behavior appears in the vast majority of the analyzed examples. As in almost every single case in this study, XFEM reproduces the jump significantly better. Special emphasis is put on the fact that XFEM reproduces the analytical solution rather well already with a comparatively coarse grid with a large mesh parameter h . It is also striking that the difference in the result between the two methods vanishes away from the interface. Nevertheless, the results of the two methods differ in the vicinity of the material interface. With a decreasing mesh parameter h , the difference between numerical results and analytical solution reduces.

The effect that standard FEM is mostly underestimating the exact jump at the material interface seems to have a simple explanation. The interface

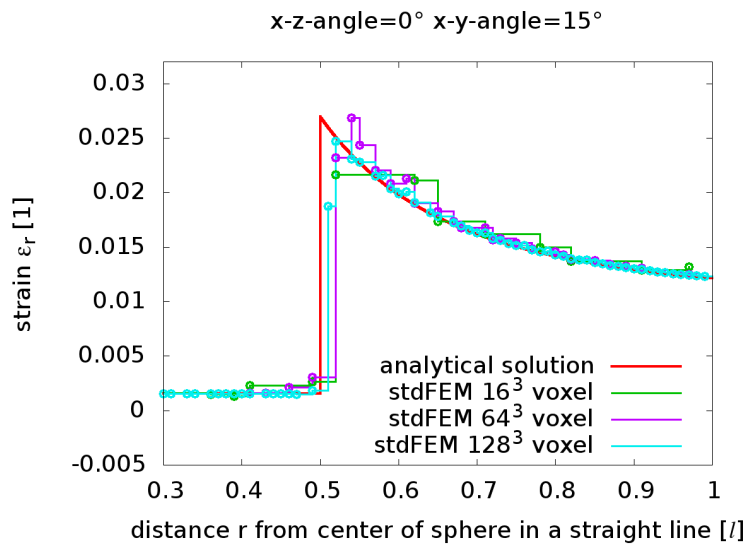


Figure 4.25: Normal strain component along line with $x-y$ -angle=15° and $x-z$ -angle=0° for standard FEM.

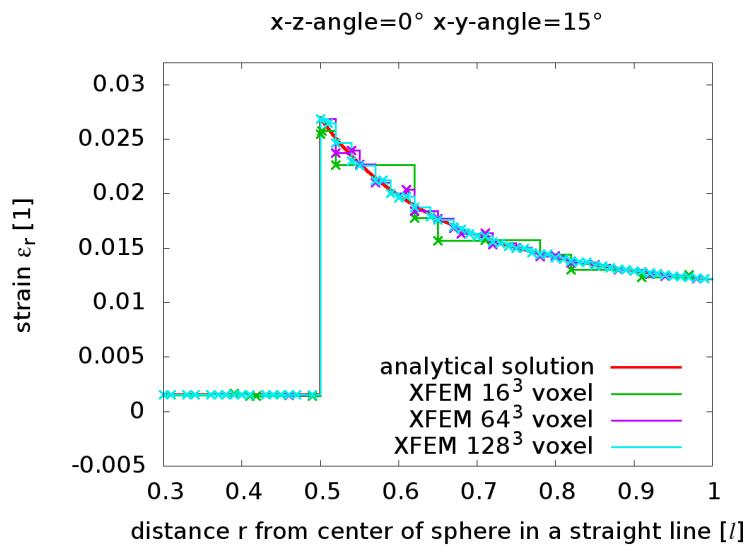


Figure 4.26: Normal strain component along line with $x-y$ -angle=15° and $x-z$ -angle=0° for XFEM.

elements are tackled with a special integration rule but linear shape functions over the whole element. Since these elements have been integrated via sub-tetrahedrons with piecewise constant material parameters, the interface elements act similar to a small layer of some interface material with some mean YOUNG'S modulus. The exact value of the resulting YOUNG'S modulus depends on the volume percentage of the different materials in the interface elements only. Nevertheless, when introducing a different integration rule without taking the sub-tetrahedrons into account, similar results are obtained, especially the general underestimation of the jump at the interface. Hence, different integration rules will not be discussed further in this work.

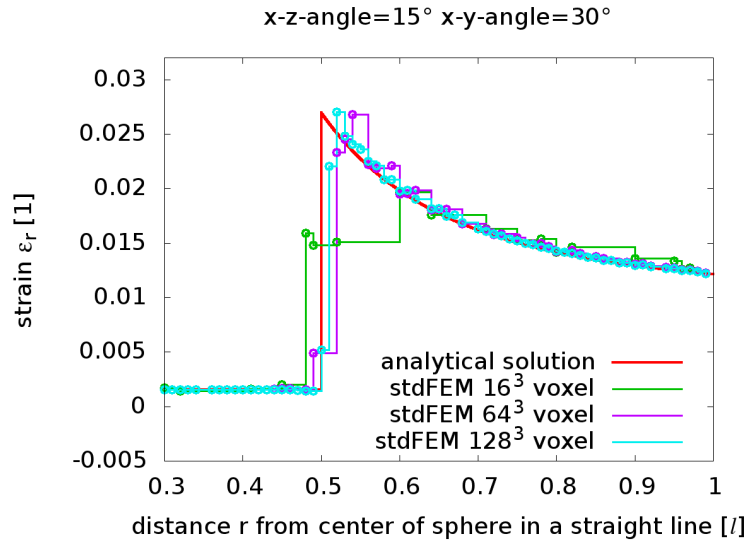


Figure 4.27: Normal strain component along line with x - y -angle= 30° and x - z -angle= 15° for standard FEM.

Fig. 4.27 and Fig. 4.28 show a line that is tilted by 15° away from the x axis in the x - z -plane and 30° in the x - y -plane, respectively. Fig. 4.27 is a good example for the standard FE method not being able to reproduce the jump in the radial strain component, independent from the mesh parameter h . Not surprising at all, the finest meshes with a mesh parameter h_4 does reproduce the jump better than the coarser meshes. An additional error is introduced as for most of the meshes in Fig. 4.27 there is a ramp up effect instead of a single jump. This again was also observed with different integration rules. Fig. 4.28 shows that the same line as in Fig. 4.27 does not lead to problems for the XFEM. Only the coarsest mesh seems to be a bit off. Nevertheless, in

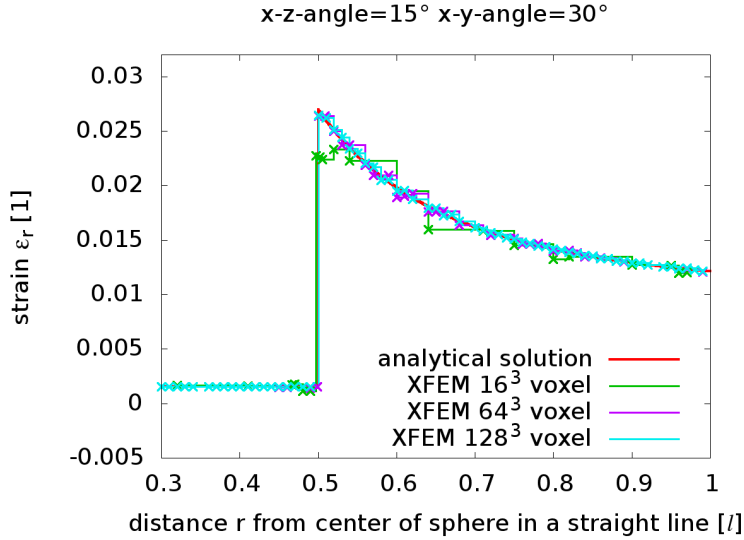


Figure 4.28: Normal strain component along line with x - y -angle= 30° and x - z -angle= 15° for XFEM.

both figures there are oscillations around the analytical solution observable, which was the case in all simulations.

To get a better impression on the difference between the computed result and the analytical solution, an error measure depending on the mesh parameter h is introduced as follows

$$e(h) = \frac{1}{|\Omega_h|} \int_{\Omega_h} \|\mathbf{u}_{\text{analytical}}(\mathbf{x}) - \mathbf{u}_h^{\text{fem/xfem}}(\mathbf{x})\| d\mathbf{x}. \quad (4.53)$$

This function introduces rational terms, as the analytical solution declines proportional to $1/r^2$ as explained in (4.50). In order to minimize the numerical error of the integration in this analysis, a RIEMANN quadrature rule (cf. [Bronstein et al., 2001]) with 167167167 integration points per tetrahedron in the finite element mesh is used.

Fig. 4.29 shows a log-log-plot of this integrated error over mesh parameter h introduced in 4.53. It strikes that the total error with XFEM on the coarsest grid with mesh parameter h_1 is only slightly larger than the total error in the standard FEM on the finest grid analyzed. The numerical convergence rate of the XFEM is drastically better than for standard FEM, as well. The order of convergence for the standard FEM is quadratic whereas the XFEM converges significantly faster. Nevertheless, it is emphasized that both XFEM

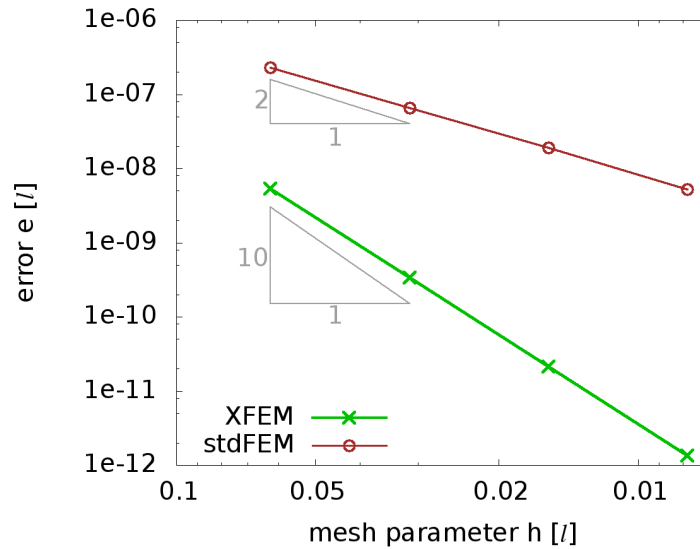


Figure 4.29: Error in displacement for different mesh parameters.

and FEM will never exactly match the analytical solution. This is due to the fact that in both cases the material interface is approximated by piecewise linear elements independent of the mesh size.

4.4 Stabilizing ill-conditioned XFEM problems

The preceding sections showed that nodal level set values close to zero lead to an ill-conditioned global stiffness matrix. Additionally, it was shown that unphysical oscillations of the displacement solution around the analytical solution is reduced when using XFEM instead of FEM. Nevertheless, they still occur. This section is presenting possible ways to tackle these two problems, starting with the ill-conditioning of the global stiffness matrix.

It is well-known that XFEM needs to circumvent the situation that the level set value at a nodal position is equal to zero. This is because it leads to (almost) linearly dependent approximation functions that span the approximation space of XFEM (see section 3.2 and cf. for example [Fries and Belytschko, 2010]). Additionally, the findings of sections 4.1.2 and 4.2 showed the exact influence of a nodal level set value close to zero on the condition of the global stiffness matrix.

Only surprisingly few publications address the problem of nearly singular

stiffness matrices or even ill-posed problems. In [Béchet et al., 2005] a preconditioner is introduced that uses a local CHOLESKY based decomposition. It is able to improve the condition of the stiffness matrix if the problem is not ill-posed, that is no nodal level set value is equal to zero. In [Menk and Bordas, 2011] a preconditioner is established, based on the domain decomposition method FETI introduced in [Farhat and Roux, 1991]. The algorithm introduced by MENK uses CHOLESKY decompositions on decomposed domains together with additional continuity constraints. Numerical examples presented in [Menk, 2011] show that this preconditioner is able to reduce the condition of the stiffness matrix to a value close to the condition of a corresponding standard FEM stiffness matrix. To the author's knowledge this method has not yet been generalized to the three-dimensional case. Additionally, it has the drawback that it requires special solution algorithms. A recent work of LÖHNERT (cf. [Löhnert, 2014]) introduces a novel approach to handle this problem. In a preprocessing step the physically meaningful zero eigenvalues of the local element stiffness matrices are computed. Physically meaningful in this context signifies the zero eigenmodes induced by the six rigid body eigenmodes and other specific boundary conditions. Elements that are barely intersected by an interface typically produce additional (numerically) zero eigenmodes. An orthogonal basis of the eigenvectors of these not physically meaningful zero eigenmodes is then used for stabilizing the element stiffness matrices. The results of this stabilization scheme are very promising in two dimensions as well as in three dimensions.

However, this work does not take algebraic stabilization schemes into account. In principal there are three different possible non-algebraic approaches to tackle the problem when nodal level set values are too close to zero. These are

- a) changing the level set value at the nodes of interest,
- b) eliminating the corresponding degrees of freedom,
- c) moving the nodal position such that its level set value changes to a value further away from zero.

Obviously, there exists a fourth possible approach, which is finding a new regular mesh that does not have any nodes in the critical vicinity of the interface. But as this is not always applicable, especially when it comes to complex microstructures, it is not considered in the following.

All of the three methods have their own advantages and disadvantages. In literature the most common one is the first approach (see for example [Bordas et al., 2007], [Fries and Belytschko, 2010] and [Liu et al., 2004]). It is

trivial to implement and provides an easy way to limit the minimal obtainable distance a node may have from the interface by moving the interface away from the nodes where it initially was too close. The major advantage of this method is that the underlying mesh is not changed and optimized methods demanding regular meshes can be used. The main disadvantage is that a change of the level set value obviously changes the exact position of the interface and therewith has a disturbing influence due to this geometrical error, when computing for example effective material properties. The approach definitively is well applicable, since the user only has to take care of a good middle course between a large minimal distance from nodes to the interface and a not too large change of the geometry due to this limit. The prior resulting in a better condition of the global stiffness matrix and therewith a significant convergence speedup of the algorithm. The latter resulting in a smaller geometrical error introduced due to this algorithm. It is emphasized that in case of a high contrast in the material parameters, even small geometrical errors may lead to large errors in the resulting solution.

The second approach summarizes different methods of eliminating the corresponding degrees of freedom. The easiest way of eliminating these degrees of freedom is a purely geometric approach. A specific element is intersected by the interface in such a way that only a tiny fraction of its volume is cut away from the rest, it is assumed that the element is not intersected by the interface at all. This results in the corresponding element being treated in the same way as a blending element. That is, it has no influence in whether its nodes are enriched or not. Additionally, the discretization of the displacement field is modeled via the standard FEM discretization in (3.9), which means that no enrichment terms are considered (see for example [Bordas et al., 2007] and [Liu et al., 2004]). This methodology introduces a small geometrical error, depending on the actual threshold value that indicates if a volume fraction is considered to be “tiny” as described above. The advantage of this methodology is indeed able to eliminate problems with nodal level set values close to zero. On the other hand when considering a three-dimensional problem, typically more complicated intersection cases occur.

Fig. 4.30 considers the example where the intersection of the interface with an element goes directly through one node which results in a nodal level set value of exactly zero. A handling of this element as a non-enriched element obviously results in a large geometrical error and is not applicable. This methodology is therefore not able to completely circumvent the problem of small nodal level set values.

Another possibility of type b) is to deactivate directly the corresponding enrichment degrees of freedom of each of these nodes. At least when using the MOËS enrichment this approach is absolutely useless as it is impossible

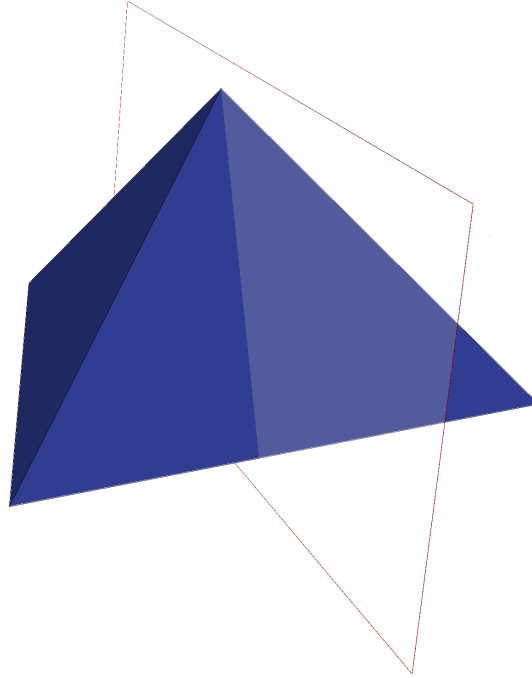


Figure 4.30: Example of worst case for an intersection plane through a tetrahedron for XFEM.

to reproduce kinks in an otherwise linear displacement field.

In approach c) nodes with level set values too close to zero are moved. It has the major advantage that the exact position of the interface is not changed, hence no additional geometrical error is introduced. The main disadvantage is that the regularity of the underlying mesh is destroyed which excludes the possibility to use memory usage optimized FEM. Additionally, when moving nodes several possible problems may occur. Firstly, it is possible to invert the volume of elements when moving the position of single nodes. Secondly, the initially specified boundary may be changed by moving non-boundary nodes to the boundary or vice versa which typically leads to unwanted results. Thirdly, the overall mesh quality typically is reduced when moving nodes away from a regular mesh which has an impact on the solution accuracy.

In this work an algorithm is created that is able to decrease the condition of the element stiffness matrix as well as the global one by moving nodal positions, whilst keeping the aforementioned disadvantages at a minimum.

4.4.1 Mesh optimization for enhancing XFEM

It has been previously stated, that when moving nodes for circumventing ill-posedness other problems typically arise. The most important one is a possibly heavily reduced overall mesh quality. The here presented novel algorithm is an iterative combination of moving nodes out of the vicinity of the interface and regularizing the mesh with both of the two algorithms presented in [Vartziotis et al., 2009] for mesh smoothing.

In a first step loop over all nodes of the mesh is performed, checking whether or not the node should be moved. When a nodal level set value is considered to be too close to zero, a direction in which the node is moved has to be specified. Naturally, the optimal direction is specified due to the gradient of the level set function as it indicates the direction to the closest point on the interface. From the approximation of the level set function in (3.33) the gradient of the level set function can be derived directly

$$\text{grad } \Phi(\mathbf{x}) \approx \frac{\partial}{\partial \mathbf{x}} \sum_{i \in K(\mathbf{x})} N_i(\mathbf{x}) \Phi(\mathbf{x}^i) = \sum_{i \in K(\mathbf{x})} \frac{\partial N_i(\mathbf{x})}{\partial \mathbf{x}} \Phi(\mathbf{x}^i) \quad (4.54)$$

with $K(\mathbf{x})$ again denoting the index set of the nodes included in an element containing point \mathbf{x} . Obviously, this index set is not unambiguous in case that the point describes a node of the finite element mesh. But with the approximation of the level set function in (3.33) and the nature of the signed distance function described in section 2.3.3 it can be assumed that in almost all cases the gradient of the level set function at a nodal position is independent from the exact choice of $K(\mathbf{x})$. The only possibility where the gradient of the level set function depends on the exact choice of $K(\mathbf{x})$ is when point \mathbf{x} has the same distance to more than one interface as discussed in section 2.3.3. These special cases are neglected in the algorithm as numerical analyses showed that the exact choice of $K(\mathbf{x})$ was insignificant for the global result. Obviously, when the nodal level set value is positive, the node is moved in the direction \mathbf{m} of the gradient of the level set function. When the nodal level set value is negative, the node is moved in the opposite direction of the gradient of the level set function.

$$m(\mathbf{x}^i) = \text{sign}((\Phi(\mathbf{x}^i)) \text{grad } \Phi(\mathbf{x}^i)) \quad (4.55)$$

As mentioned before, a typical problem when moving nodes are the geometrical boundaries of the finite element mesh. If a node lies on the boundary, its new position is first computed similar to all other nodes but afterwards the new position is projected back to the boundary. Similarly, nodes from the

inner of the mesh are not allowed to move onto or even across the geometrical boundary.

The last aforementioned problem is the possibility of inverted elements due to a movement of nodes, when a node is moved such that the volume of the element would become negative. This obviously has to be crosschecked element-wise before actually moving any nodes. Typically, the problem of inverted elements can be prevented by doing multiple iterations of small nodal movements instead of large shifts.

The algorithm presented here has in principal three parameters for variations: A threshold parameter t_0 identifies which nodal level set value is considered to be too close to zero and therewith specifying the nodes that have to be moved. The second parameter defines how far a node is moved in the direction of the gradient of the level set function and is called shiftingfactor s_0 . It is important to emphasize that the movement has to be kept relative to the element size of the finite element mesh. As a third parameter n_{it} it is suggested to perform multiple iterations of the whole algorithm with a decreasing threshold parameter, which has the effect that nodes closer to the interface are moved multiple times and hence farther than the ones further away but still in the vicinity of the interface.

Algorithm 4.1: Moving nodes core algorithm

```

1 algorithm is initialized with parameters  $t_0$  and  $s_0$ 
2 for all nodes  $x^i$  in mesh do
3   if  $|\Phi(x^i)| < t_0$  then
4     find  $K(x^i)$ 
5     compute  $\mathbf{m}(x^i)$ 
6     compute new position  $\mathbf{x}_{new}^i = \mathbf{x}^i + s_0\mathbf{m}(x^i)$ :
7     perform consistency checks for new position:
8       Is an element inverted?
9        $\mathbf{x}_{new}^i = \mathbf{x}^i$ 
10      Is a boundary node moved away from the boundary?
11      project  $\mathbf{x}_{new}^i$  back on the boundary
12      Is a nodal point in the inner of mesh moved to the boundary?
13      project  $\mathbf{x}_{new}^i$  back inside the boundary
14      move node number  $i$  to position  $\mathbf{x}_{new}^i$ 

```

Obviously, there are multiple ways of projecting a node, in case a consistency check fails. This work only considers finite element meshes in the form of cubes with $\Omega = \{[0, 1] \times [0, 1] \times [0, 1]\}$. Whenever a boundary consistency check in algorithm 4.1 fails, only a single component of \mathbf{x}_{new}^i interacts with the

specific boundary, for example the y -component. In this case the projection is chosen as

$$\mathbf{x}_{\text{new,projection}}^i = (x_{\text{new},x}^i, x_y^i, x_{\text{new},z}^i). \quad (4.56)$$

The handling of the other boundaries is analog. In case of more complicated geometries a different projection scheme has to be applied, which is straight forward.

After applying algorithm 4.1, the overall mesh quality typically is reduced drastically which leads to unwanted numerical results like oscillatory effects and possibly bad conditioning of the resulting stiffness matrix. Hence, in a second step a sequential mesh regularization algorithm and a simultaneous mesh regularization algorithm, both introduced in [Vartziotis et al., 2009] is applied. The prior is good for enhancing the regularity of individual elements with especially obtuse angles. The latter enhances the overall smoothness of the mesh. Both algorithms have a large multitude of parameters. The exact values of the parameters used in this work can be found in appendix A.4. It is emphasized, that the mesh smoothing algorithm of course has to perform consistency checks as well, similar to the ones described in algorithm 4.1.

The final algorithm suggested in this work consists of a combination of the previously described sub algorithms. First a rigorous movement of nodes in the vicinity of the interface is applied. Then a considerable mesh smoothing and afterwards a second iteration of the interface related nodal movement algorithm, but this time with moderate movement only.

Algorithm 4.2: Moving nodes complete algorithm

- 1 algorithm is initialized with parameters t_1 , s_0 , n_{it}^1 and n_{it}^2
 - 2 **for** parameter $i \in \{1, \dots, n_{\text{it}}^1\}$ **do**
 - 3 $t_0 = (i/n_{\text{it}}^1)^2 t_1$
 - 4 run algorithm 4.1 with parameters t_0 and s_0
 - 5 run simultaneous mesh smoothing algorithm
 - 6 run sequential mesh smoothing algorithm
 - 7 **for** parameter $i \in \{1, \dots, n_{\text{it}}^2\}$ **do**
 - 8 $t_0 = (i/n_{\text{it}}^2)^2 t_1$
 - 9 run algorithm 4.1 with parameters t_0 and s_0
-

In section 4.2 an example is introduced with a layered material with different positions of the interface. Exactly the same situation is now considered again and the results of the standard tetrahedral mesh generated from a voxelized image is compared to the results when preprocessing the mesh with mesh

optimization algorithm 4.2. The parameters used for algorithm 4.2 are:

$$t_1 = 0.01, \quad s_0 = 0.8, \quad n_{it}^1 = 3, \quad n_{it}^2 = 0 \quad (4.57)$$

For being able to quantify the influence of moving nodes away from the interface without the influence of the mesh regularization step, the mesh regularization relaxation parameter $\rho = 0$ is chosen, which equals no regularization at all.

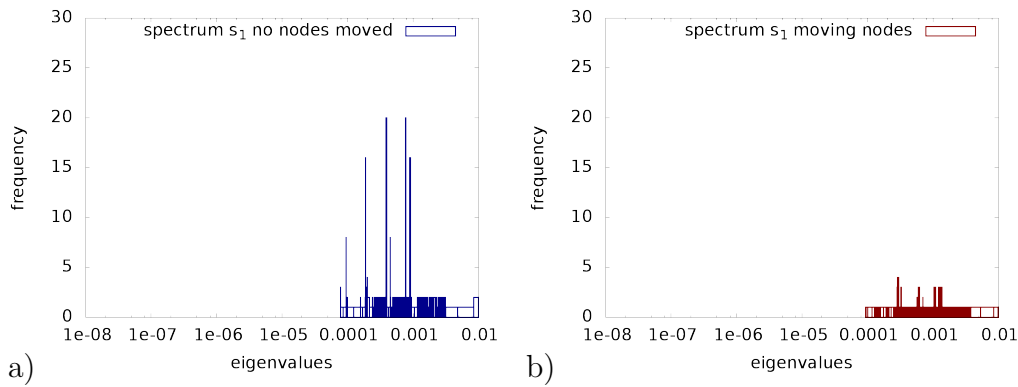


Figure 4.31: Lower end of spectrum of stiffness matrix for position parameter $s_1 = 0.55$, a) spectrum without moving nodes algorithm, b) spectrum after applying moving nodes algorithm.

Fig. 4.31 depicts the eigenvalues of the global stiffness matrix for the position parameter $s_1 = 0.55$ which was describing that the interface is aligned exactly in the center between two layers of nodes from the quasi-regular mesh. Only a closeup of the lower end of the spectrum is shown as the algorithm is designed to interfere there only and it has an almost not observable influence to the rest of the spectrum. Fig. 4.31 a) shows the results for the unchanged mesh, Fig. 4.31 b) shows the results for the optimized one. It strikes that the absolute values are not changed much ($7.87 \cdot 10^{-5}$ for the original mesh versus $9.48 \cdot 10^{-5}$ for the preprocessed mesh). This is not surprising as the interface is aligned in the middle between two layers of nodes from the finite element mesh. Such an alignment is the optimal case for XFEM when focusing on the eigenvalues corresponding to the enrichment degrees of freedom with respect to a good condition of the global stiffness matrix, just as the findings of the preceding sections suggest.

Another effect is that in Fig. 4.31 a) several eigenvalues occur repeatedly in the global stiffness matrix which is not the case for the preprocessed mesh in Fig. 4.31 b). Again this effect is not surprising due to the symmetry and

regularity of the unchanged mesh. As small perturbations to the mesh lead to small changes in corresponding eigenvalues no such peaks in the histogram of Fig. 4.31 b) can be expected.

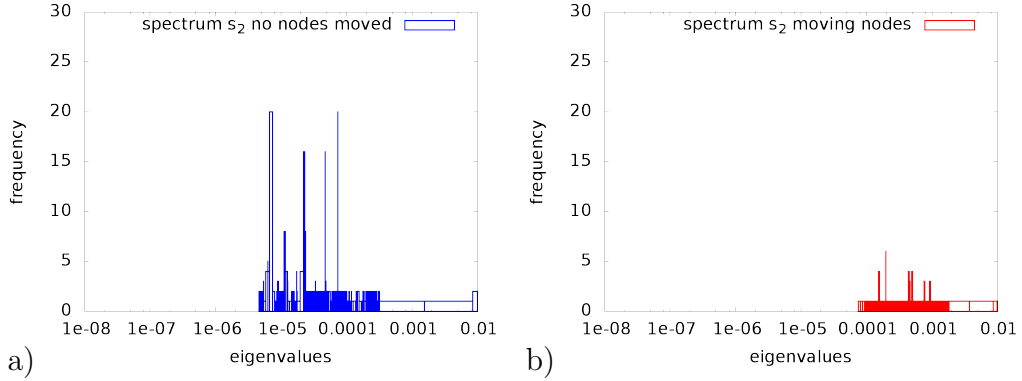


Figure 4.32: Lower end of spectrum of stiffness matrix for position parameter $s_2 = 0.505$, a) spectrum without moving nodes algorithm, b) spectrum when applying moving nodes algorithm.

Fig. 4.32 now depicts a closeup of the lower end of the eigenvalues of the global stiffness matrix for the position parameter $s_2 = 0.505$. This parameter describes the situation where the distance from the interface to a layer of nodes is one-tenth of the previous one with parameter s_1 . Again the rest of the spectrum is not visualized as there is almost no observable effect on these eigenvalues. Fig. 4.32 a) shows the results for the original mesh and Fig. 4.32 b) shows the results for the preprocessed mesh.

Again the peaks at individual eigenvalues are cut away in Fig. 4.32 b) which is unsurprising. But this time it strikes that the smallest eigenvalues in Fig. 4.32 b) are significantly larger than the ones from Fig. 4.32 a) ($4.59 \cdot 10^{-6}$ for the original mesh versus $7.78 \cdot 10^{-5}$ for the preprocessed mesh). This leads directly to an decreased condition κ of the global stiffness matrix of a whole magnitude.

Fig. 4.33 shows the same analysis as before but for parameter $s_3 = 0.5005$ which again reduces the distance of the interface to a layer of nodes to one-tenth of the distance from the example with parameter s_2 . Again Fig. 4.33 a) corresponds to the original mesh and Fig. 4.33 b) corresponds to the preprocessed mesh. As before the peaks in the histogram vanish in the preprocessed mesh and again the minimal eigenvalue is increased, this time from $4.82 \cdot 10^{-8}$ for the original mesh to $5.73 \cdot 10^{-5}$ for the preprocessed mesh. This results in the condition of the global stiffness system to be decreased by a factor larger than 1000 when preprocessing the mesh! The findings of this section

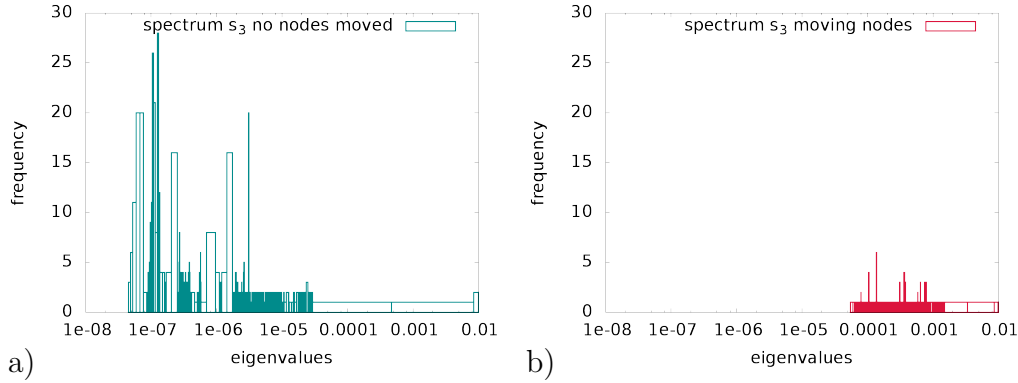


Figure 4.33: Lower end of spectrum of stiffness matrix for position parameter s_3 , a) spectrum without moving nodes algorithm, b) spectrum when applying moving nodes algorithm.

are summarized in table 4.3.

| | without mesh optimization | with mesh optimization |
|--------------------------------|---------------------------|------------------------|
| $\lambda_{\min}(s_1 = 0.55)$ | $7.87 \cdot 10^{-5}$ | $9.48 \cdot 10^{-5}$ |
| $\lambda_{\max}(s_1 = 0.55)$ | 7.42 | 7.51 |
| $\kappa(s_1 = 0.55)$ | $9.43 \cdot 10^4$ | $7.94 \cdot 10^4$ |
| $\lambda_{\min}(s_2 = 0.505)$ | $4.59 \cdot 10^{-6}$ | $7.78 \cdot 10^{-5}$ |
| $\lambda_{\max}(s_2 = 0.505)$ | 7.54 | 7.63 |
| $\kappa(s_2 = 0.505)$ | $1.64 \cdot 10^6$ | $9.80 \cdot 10^4$ |
| $\lambda_{\min}(s_3 = 0.5005)$ | $4.82 \cdot 10^{-8}$ | $5.73 \cdot 10^{-5}$ |
| $\lambda_{\max}(s_3 = 0.5005)$ | 7.56 | 7.66 |
| $\kappa(s_3 = 0.5005)$ | $1.57 \cdot 10^8$ | $1.34 \cdot 10^5$ |

Table 4.3: Condition of the global stiffness matrix for different position parameters s with and without mesh optimization.

It strikes that in all three examples the magnitude of the smallest eigenvalue is the same when preprocessing the mesh and it is more or less equal to the one of the original mesh with parameter s_1 which is the best possible for XFEM when not preprocessing the mesh. The resulting condition of the global stiffness matrix is almost the same for all three different position parameters s , even though the original condition numbers differ by two magnitudes each. Obviously, the example corresponding to parameter s_3 is very thankful for the algorithm as all the elements intersected by the interface are intersected very close to at least one node. Obviously, the approach described in section

4.4 of changing the level set value would also be able to increase the minimal eigenvalues and therewith decrease the condition of the global stiffness matrix. On the other hand this very method of changing the level set values would move the whole interface as a whole layer of nodes is positioned too close to the interface. Hence, a non negligible change in the solid volume fraction of the two materials can be expected in this example when changing the level set values instead of moving the nodes.

4.4.2 Reducing non-physical stress peaks

Whenever numerical simulations are carried out, discretization errors occur. A typical phenomenon resulting from these are unphysical stress peaks, often in the form of oscillations around the correct values. When computing effective material properties this usually is not a big issue. But when considering for example plastification processes it is of crucial importance whether or not the yield strength is reached. This is because the principal material response changes from a purely elastic deformation to a plastic floating as described in section 2.2.3.

During the analysis carried out for section 4.3 it struck that XFEM is able to reduce such unphysical stress peaks. Even though, when analyzing the comparatively trivial scenario of a single spherical inclusion the stress peaks did not vanish completely. The moving nodes algorithm presented in section 4.4.1 is able to further reduce the unphysical stress peaks. Hence, a problem similar to the one in section 4.3 is now analyzed with an additional preprocessing of the mesh.

The problem setting is a spherical inclusion in the center of the unit cube of dimensions $\Omega = [0, 1] \times [0, 1] \times [0, 1]$ with the diameter d of the sphere being half of the length of the surrounding cube, hence $d = 0.5$.

An isotropic linear elastic behavior is assumed for both materials. The material parameters read

$$E_{\text{sphere}} = 1 \text{ MPa}, E_{\text{matrix}} = 10 \text{ MPa} \text{ and } \nu_{\text{sphere}} = \nu_{\text{matrix}} = 0.3. \quad (4.58)$$

As boundary conditions the following DIRICHLET type boundary condition

are chosen

$$\begin{aligned}
 \mathbf{x} \in \{ 0 \times [0, 1] \times [0, 1] \} &\Rightarrow u_1 = 0, \\
 \mathbf{x} \in \{ 1 \times [0, 1] \times [0, 1] \} &\Rightarrow u_1 = 0.2, \\
 \mathbf{x} \in \{ [0, 1] \times 0 \times [0, 1] \} &\Rightarrow u_2 = 0, \\
 \mathbf{x} \in \{ [0, 1] \times 1 \times [0, 1] \} &\Rightarrow u_2 = 0, \\
 \mathbf{x} \in \{ [0, 1] \times [0, 1] \times 0 \} &\Rightarrow u_3 = 0, \\
 \mathbf{x} \in \{ [0, 1] \times [0, 1] \times 1 \} &\Rightarrow u_3 = 0,
 \end{aligned}
 \tag{4.59}$$

which corresponds to an uniaxial tensile loading with 20% strain. Due to symmetry reasons only one-eighth of the cube is analyzed.

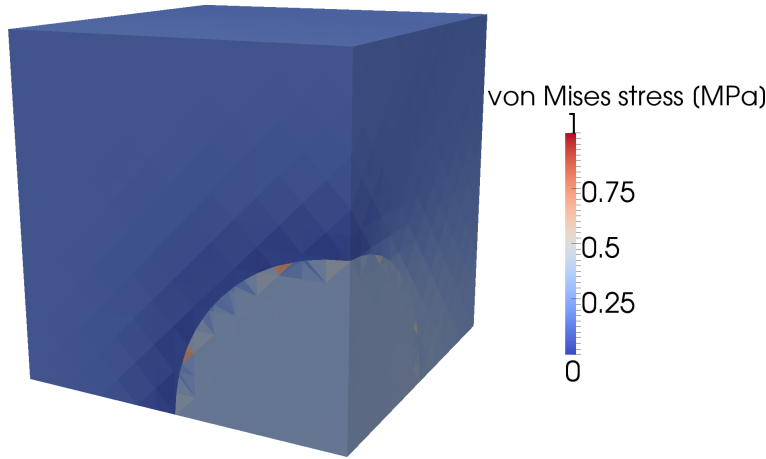


Figure 4.34: Example for stress peaks using XFEM.

Fig. 4.34 shows an example discretization for the above described problem (without a preprocessing of the mesh) where the VON MISES equivalent stress is plotted. Theoretically, this stress should be constant in the interior of the sphere in case of an infinitely extended matrix (cf. for example [Mura, 1987]). In a case of a finite volume like in this example some small variations in the VON MISES equivalent stress can be expected, but they are dominated by stress peaks resulting from numerical discretization errors, as illustrated in Fig. 4.34. In the following the VON MISES equivalent stress on the surface of the sphere is visualized for different mesh discretizations, each time once with the previously described preprocessing of the mesh and once without the preprocessing. The color scheme of the follow-up images is in all cases the same as in Fig. 4.34. Additionally, the exact values of the VON MISES equivalent stress in the outermost layer of tetrahedrons of the sphere are plotted in histograms. The histograms refer to the number of sub-tetrahedrons (as explained in section 3.2) with a given VON MISES equivalent stress.

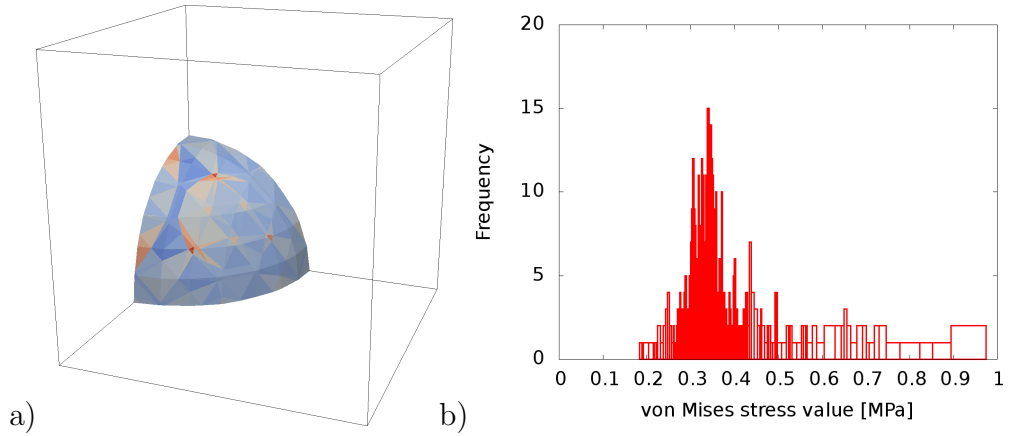


Figure 4.35: Reference result 10x10x10 voxels, color scheme as in Fig. 4.34
 a) visualization of the VON MISES equivalent stress at the bound of the sphere,
 b) histogram of the frequency of the different values for the VON MISES equivalent stress.

Fig. 4.35 shows the situation for a discretization of the tetrahedral mesh generated from a $10 \times 10 \times 10$ voxel mesh. In Fig. 4.35 a) it becomes obvious that the highest stress peaks occur in very small sub-tetrahedrons. The highest VON MISES equivalent stress value occurring in the mesh is 0.93 MPa.

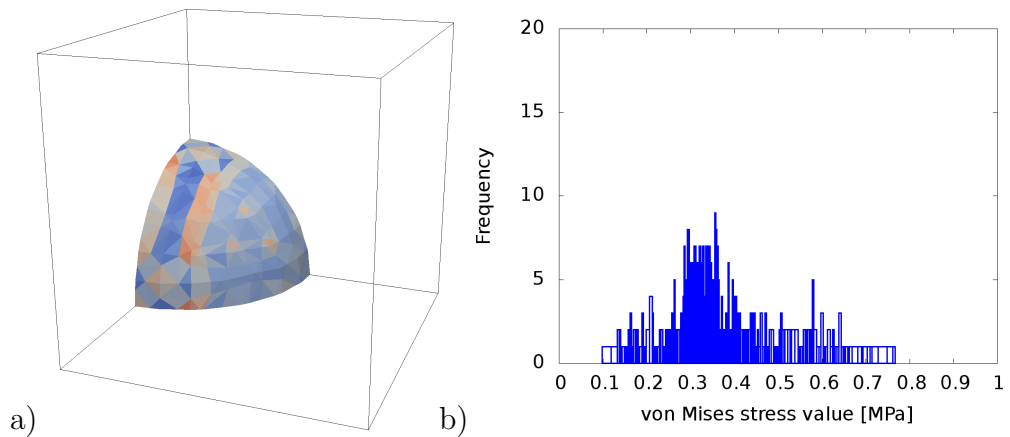


Figure 4.36: Remeshed result 10x10x10 voxels, color scheme as in Fig. 4.34
 a) visualization of the VON MISES equivalent stress at the bound of the sphere,
 b) histogram of the frequency of the different values for the VON MISES equivalent stress.

Fig. 4.36 presents the same situation for a discretization of the tetrahedral mesh generated from a $10 \times 10 \times 10$ voxel mesh, but this time the node moving

algorithm 4.2 has been applied first with parameters $s_0 = 0.7 \cdot \text{voxel length}$, $t_1 = 0.5$, $n_{\text{it}}^1 = 3$ and $n_{\text{it}}^2 = 5$. In Fig. 4.36 a) it can be seen easily that the tiny sub-tetrahedrons have been enlarged due to the preprocessing algorithm. It also becomes obvious from Fig. 4.36 b) that the maximal VON MISES equivalent stress value is reduced. The maximal value is equal to 0.76 MPa which equals a reduction to 81.64% of the original value.

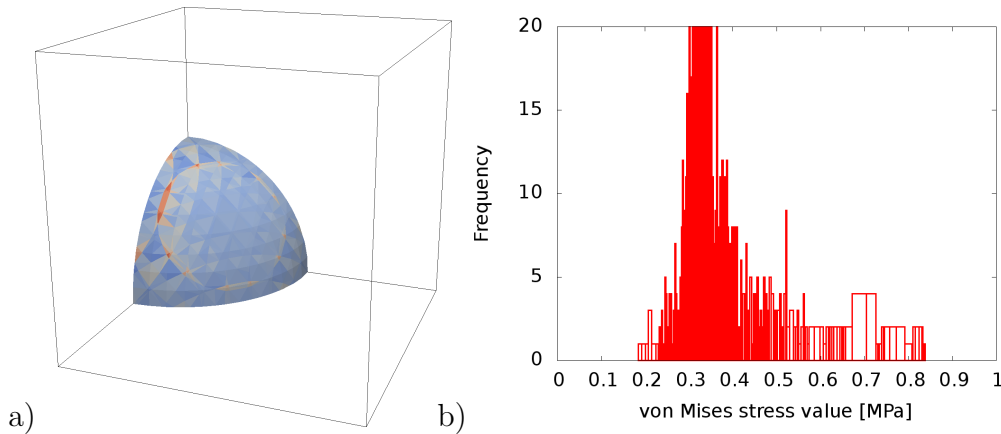


Figure 4.37: Reference result 16x16x16 voxels, color scheme as in Fig. 4.34
a) visualization of the VON MISES equivalent stress at the bound of the sphere,
b) histogram of the frequency of the different values for the VON MISES equivalent stress.

Fig. 4.37 depicts the results corresponding to a discretization of the tetrahedral mesh generated from a $16 \times 16 \times 16$ voxel mesh. In Fig. 4.37 a) it becomes obvious again, that the highest stress peaks occur in very small sub-tetrahedrons. The highest VON MISES equivalent stress value occurring in the mesh is 0.84 MPa.

Fig. 4.38 reveals the same situation for a discretization of the tetrahedral mesh generated from a $16 \times 16 \times 16$ voxel mesh, where the node moving algorithm 4.2 has been applied first with parameters $s_0 = 0.7 \cdot \text{voxel length}$, $t_1 = 0.4$, $n_{\text{it}}^1 = 20$ and $n_{\text{it}}^2 = 5$. In Fig. 4.38 a) again it can be seen that the smallest sub-tetrahedrons have been enlarged due to the preprocessing algorithm. Also, it becomes obvious from Fig. 4.38 b) that the maximal VON MISES equivalent stress value is reduced. The maximal value is 0.76 MPa which is the same as in the previous preprocessed example and equals a reduction to 91.38% of the original value.

Fig. 4.39 shows the results corresponding to a discretization of the tetrahedral mesh generated from a $32 \times 32 \times 32$ voxel mesh. In Fig. 4.39 a) the stress peaks are not obvious anymore. The highest VON MISES equivalent stress value occurring in the mesh is 0.68 MPa.

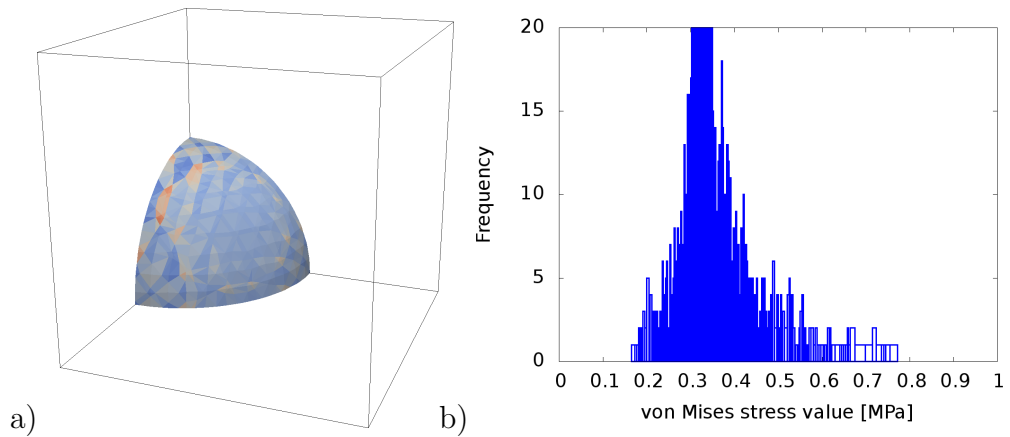


Figure 4.38: Remeshed result 16x16x16 voxels, color scheme as in Fig. 4.34
a) visualization of the VON MISES equivalent stress at the bound of the sphere,
b) histogram of the frequency of the different values for the VON MISES equivalent stress.

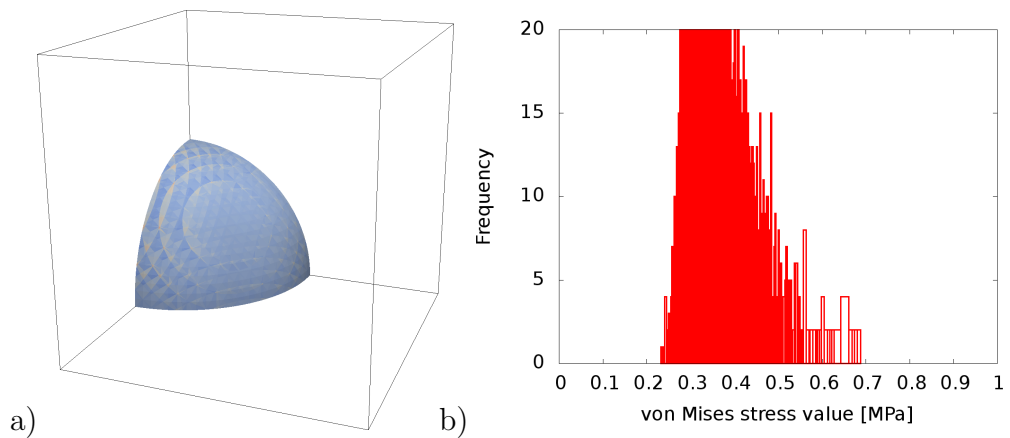


Figure 4.39: Reference result 32x32x32 voxels, color scheme as in Fig. 4.34
a) visualization of the VON MISES equivalent stress at the bound of the sphere,
b) histogram of the frequency of the different values for the VON MISES equivalent stress.

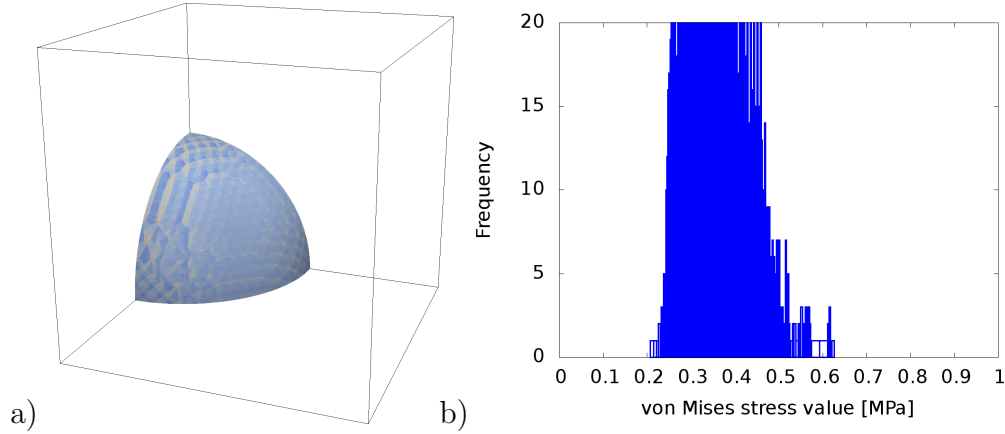


Figure 4.40: Remeshed result $32 \times 32 \times 32$ voxels, color scheme as in Fig. 4.34
a) visualization of the VON MISES equivalent stress at the bound of the sphere,
b) histogram of the frequency of the different values for the VON MISES equivalent stress.

Fig. 4.40 depicts the same situation for a discretization of the tetrahedral mesh generated from a $32 \times 32 \times 32$ voxel mesh, this time with the node moving algorithm 4.2 with parameters $s_0 = 0.8 \cdot \text{voxel length}$, $t_1 = 0.4$, $n_{\text{it}}^1 = 20$ and $n_{\text{it}}^2 = 5$. In Fig. 4.40 a) once more it can be seen that the smallest sub-tetrahedrons have been enlarged due to the preprocessing algorithm. Again, in Fig. 4.40 b) the maximal VON MISES equivalent stress value is reduced in comparison to Fig. 4.39 b). The maximal value is 0.62 MPa which equals a reduction to 91.31% of the original value.

Fig. 4.41 displays the results corresponding to a discretization of the tetrahedral mesh generated from a $64 \times 64 \times 64$ voxel mesh. In Fig. 4.41 a) no stress peaks are obvious anymore. The highest VON MISES equivalent stress value occurring in the mesh is 0.53 MPa.

Fig. 4.42 illustrates the same situation for a discretization of the tetrahedral mesh generated from a $64 \times 64 \times 64$ voxel mesh, again this time with the node moving algorithm 4.2 applied first with parameters $s_0 = 0.8 \cdot \text{voxel length}$, $t_1 = 0.5$, $n_{\text{it}}^1 = 20$ and $n_{\text{it}}^2 = 5$. applied first. In Fig. 4.42 a) again the smallest sub-tetrahedrons have been enlarged due to the preprocessing algorithm. Fig. 4.42 b) shows that the maximal VON MISES equivalent stress value is reduced in comparison to Fig. 4.41 b) but not as much as in the discretization examples before. The maximal value occurring in the mesh is 0.51 MPa which equals a reduction to 96.63% of the original value.

Table 4.4 summarizes the results of this section by comparing the maximal occurring values of the VON MISES equivalent stress values σ_v^{max} once with and once without the mesh optimization algorithm for different mesh dis-

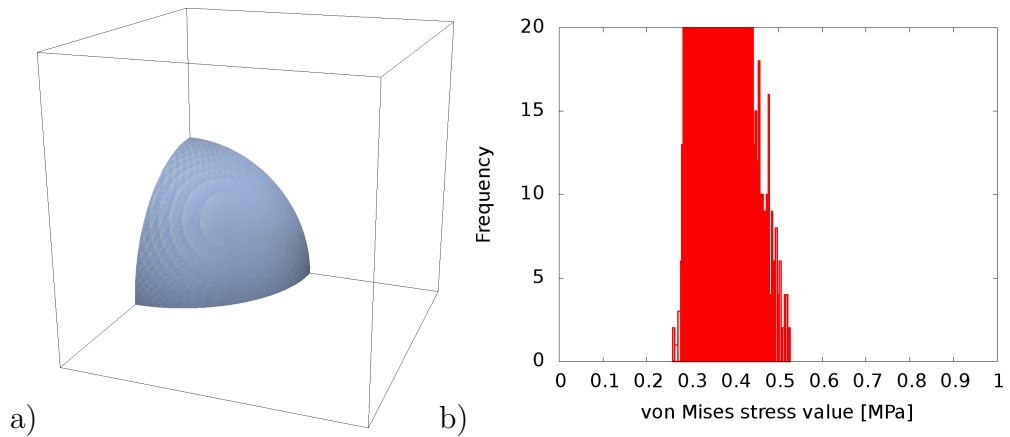


Figure 4.41: Reference result 64x64x64 voxels, color scheme as in Fig. 4.34
a) visualization of the VON MISES equivalent stress at the bound of the sphere,
b) histogram of the frequency of the different values for the VON MISES equivalent stress.

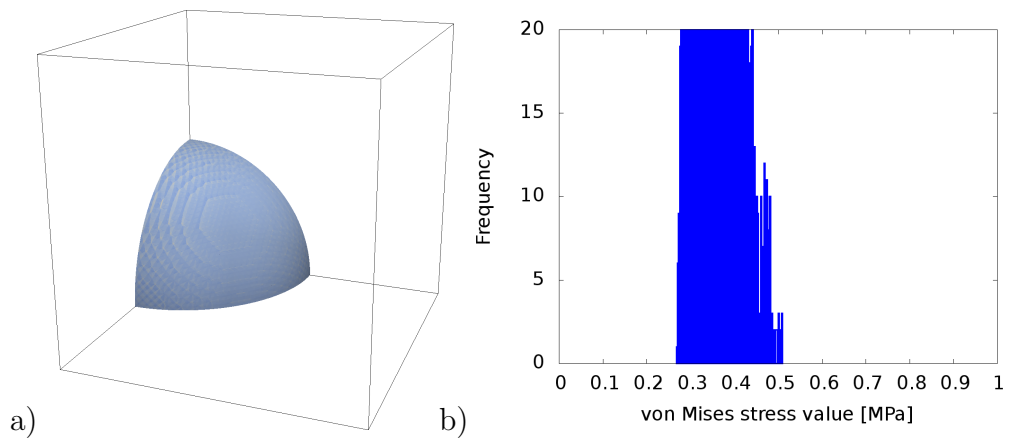


Figure 4.42: Remeshed result 64x64x64 voxels, color scheme as in Fig. 4.34
a) visualization of the VON MISES equivalent stress at the bound of the sphere,
b) histogram of the frequency of the different values for the VON MISES equivalent stress.

cretization sizes.

| mesh discretization | σ_v^{\max} original | σ_v^{\max} optimized mesh | red. factor |
|--------------------------------|----------------------------|----------------------------------|-------------|
| $10 \times 10 \times 10$ voxel | 0.935 MPa | 0.763 MPa | 81.64% |
| $16 \times 16 \times 16$ voxel | 0.835 MPa | 0.763 MPa | 91.38% |
| $32 \times 32 \times 32$ voxel | 0.683 MPa | 0.624 MPa | 91.31% |
| $64 \times 64 \times 64$ voxel | 0.527 MPa | 0.510 MPa | 96.63% |

Table 4.4: Reduction of stress peaks with mesh optimization algorithm 4.2.

Summarizing the different discretization examples it strikes that the node moving algorithm has the potential to reduce unphysical stress peaks significantly, especially when the underlying finite element discretization is done on a coarse mesh. For finer grids the potential of reducing stress peaks is not as good, due to fact that for finer discretizations the stress peaks are already naturally reduced in the original mesh.

It is emphasized that for the remeshed results presented here, different parameter sets for the node moving algorithm 4.2 have been used. In some rare cases some combinations of algorithmic parameters even lead to an increased maximal VON MISES equivalent stress in the mesh, even though the total amount of elements with a large stress value had been reduced. Overall, it becomes obvious that more research in the fine tuning of the algorithm seems worthwhile. Nevertheless, a good potential of the algorithm in reducing unphysical stress peaks has been demonstrated even though it has been specifically designed for a reduction of the condition of the global stiffness matrix without introducing additional geometrical errors.

Chapter 5

Applications

5.1 Adhesive joints in concrete

In the context of concrete constructions which are as filigree and material-saving as possible, shell structures are particularly well-suited. But as these structures can not be cast in a single construction step, special focus must be put on joining the multiple members to an entire structure. One possible solution of this is the use of adhesive joints as a method of a continuous connection. The drawback of adhesive joints of structural concrete elements is the relatively low adhesive strength of the near-surface concrete layers, assuming that the strength of the adhesive is sufficient (cf. [Oster et al., 2012]).

In this section some results are presented for optimizing the adhesive joint geometry in such a way that the tensile stresses caused by the applied loads are reduced to a minimum.



Figure 5.1: Test joint geometries: a) rectangular teeth, b) triangular teeth, c) undercut geometry.

The three different test geometry types considered are shown in Fig. 5.1 (images from [Schnell et al., 2013], courtesy of Prof. Christian Kohlmeyer). Obviously, all of these geometries offer the possibility to consider only a small fraction of the structure for simulations due to the periodicity of the structure. Fig. 5.2 shows the simulation setting, that is the considered microstructure, the symmetry planes and the boundary conditions of the uniaxial tensile loading test with 2 MPa.

As already stated, the focus of this work lies on optimizing the joint geometry such that the tensile stresses within the structure, caused by external loads,

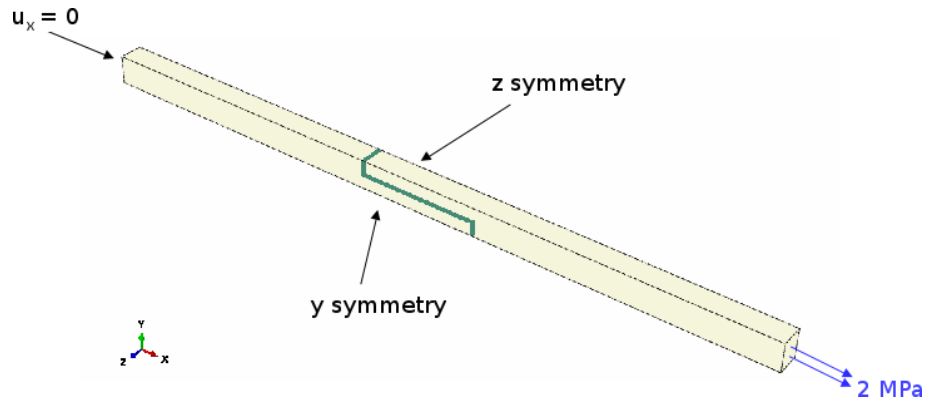


Figure 5.2: Simulation setting: Uniaxial tensile loading with 2 MPa with a periodic microstructure.

are reduced to a minimum. Undertaking such a task with standard FEM, for every joint geometry under consideration a new finite element mesh has to be created. With XFEM a regular finite element mesh can be used and just the level set function has to be changed accordingly. As explained in section 3.2 for the enhanced abs enrichment the signed distance function is required as the corresponding level set function. The signed distance function comes straight forward in case the underlying geometry is analytically known. Hence, for this study a simple parametrization of the geometry of the adhesive joint has been created, depending on the following three parameters only

$$\begin{aligned}
 \text{width:} & \quad A \cdot 18 \text{ mm} \quad A \in [0, 0.8], \\
 \text{depth:} & \quad B \cdot 75 \text{ mm} \quad B \in [0, 1], \\
 \text{thickness:} & \quad d = 3 \text{ mm}.
 \end{aligned} \tag{5.1}$$

Fig. 5.3 shows an example geometry created from model parameters $A = 0.5$ and $B = 1$.

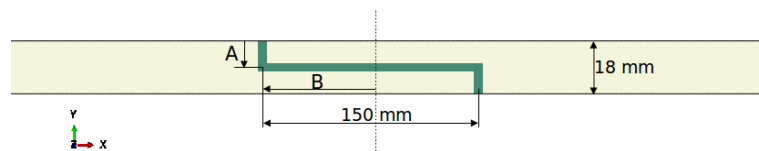


Figure 5.3: Example visualization for model parameter $A = 0.5$ and $B = 1$.

The third parameter, describing the thickness of the adhesive joint is kept constant with $d = 3 \text{ mm}$ in the whole study. With the predefined intervals $A \in [0, 0.8]$ and $B \in [0, 1]$ all admissible geometry types shown in Fig. 5.1 can

be reproduced, given the maximal depth of the adhesive joint being 150 mm. The rectangular teeth are reproduced with parameter $A = 0.5$. A value for parameter A larger than 0.5 leads to the prescribed undercut geometry and a value smaller than 0.5 leads to the geometry type triangular teeth. The parameter B describes the length of the teeth.

For the simulations the following material parameters are chosen, according to tests undertaken in the project, for an assumed linear elastic material behavior

$$E_{\text{concrete}} = 39 \text{ GPa}, E_{\text{joint}} = 36 \text{ GPa} \text{ and } \nu_{\text{concrete}} = \nu_{\text{joint}} = 0.2. \quad (5.2)$$

The underlying finite element mesh used for this analysis is a regular voxel based tetrahedron mesh with a voxel length of 1 mm. This leads to a discretization of the width of the glue joints with at least 3 layers of voxels at every point within the geometry. Fig. 5.4 – Fig. 5.6 show some examples of the influence of the geometry of the adhesive joint on the maximal principal stresses in the geometry.

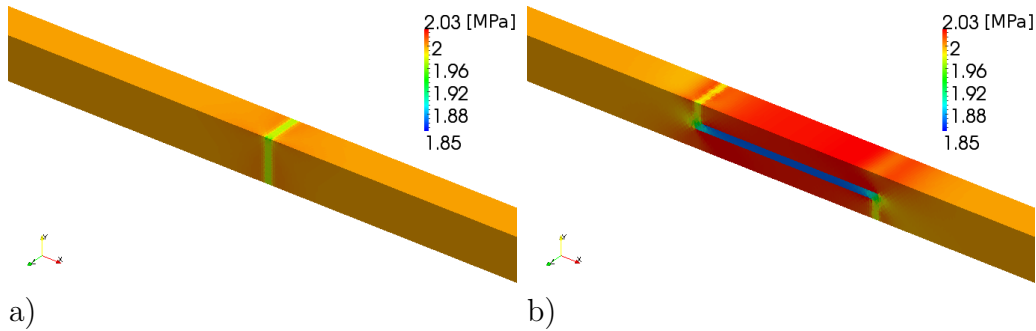


Figure 5.4: Maximal principal stress in the material when using model parameters a) $A = 0.0$ and $B = 0.0$ and b) $A = 0.5$ and $B = 0.5$.

These few examples make it obvious already, that a larger value for parameter B results in a larger region of high principal stress. Obviously, a closer look at the complete admissible range for the parameters A and B is of interest. In order to evaluate the results of a parameter set, a measure is needed that quantifies how critical the tensile load of 2 MPa for the given structure is. As a preliminary thought to obtain such a measure, assume the load to lead to a constant strain over the whole geometry, resulting in

$$\begin{aligned} \sigma_{N,\text{concrete}} &= 2.0 \text{ MPa}, \\ \sigma_{N,\text{joint}} &= 2.0 \text{ MPa} \cdot \frac{E_{\text{joint}}}{E_{\text{concrete}}} \approx 1.8 \text{ MPa}, \end{aligned} \quad (5.3)$$

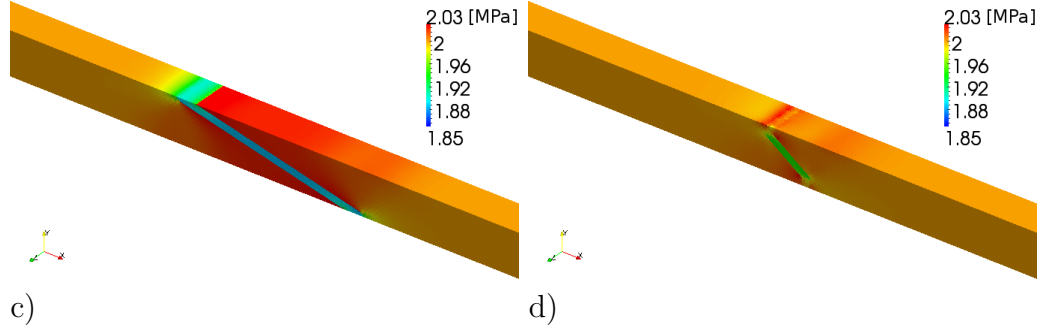


Figure 5.5: Maximal principal stress in the material when using model parameters c) $A = 0.0$ and $B = 0.5$ and d) $A = 0.2$ and $B = 0.1$.

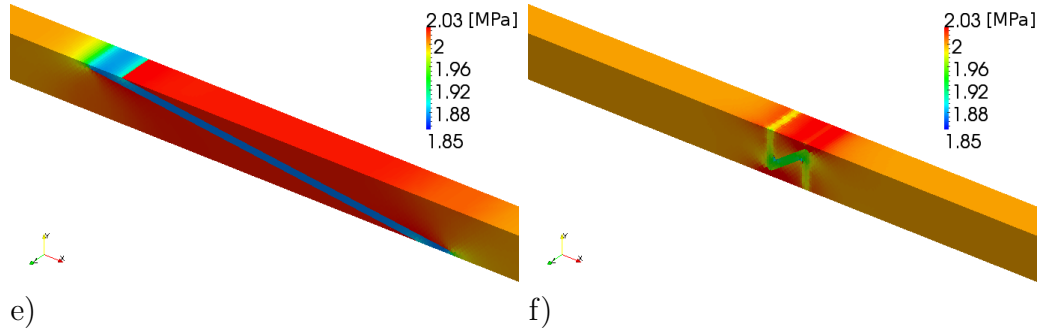


Figure 5.6: Maximal principal stress in the material when using model parameters e) $A = 0.0$ and $B = 1.0$ and f) $A = 0.8$ and $B = 0.1$.

with $\sigma_{1,\max}(\mathbf{x})$ denoting the maximal principal stress at point \mathbf{x} . The following measure is used for evaluating the quality of the geometry

$$q(\Omega) = \sqrt{\frac{1}{V_\Omega} \int_{\Omega} \left(\frac{\max[(\sigma_{1,\max}(\mathbf{x}) - \sigma_{N,\Omega}), 0]}{\sigma_{N,\Omega}} \right)^2 d\mathbf{x}}. \quad (5.4)$$

The reason for using such a non-trivial quality measure originates in the nature of concrete. Exceeding the critical stress results in a certain probability of failure and the size of the area where these stress peaks occur has an influence on the probability of failure. Hence, a measure is chosen such that takes the following criteria into consideration

- Areas where the critical principal stress value is not exceeded are not influencing the measure.
- If the critical value is exceeded just barely, but on a large area, this

must have a non negligible influence.

- Small areas with a high exaggeration of the critical value should have a comparable influence to large areas of small exaggerations.
- Due to the fact that the exact value of the critical principal stress is not known, a reasonable norm value is taken instead that would be the result of a homogeneous material response to the applied external load.

Fig. 5.7 shows the previously introduced quality measure $q(\Omega_{\text{joint}})$ in a) and $q(\Omega_{\text{concrete}})$ in b).

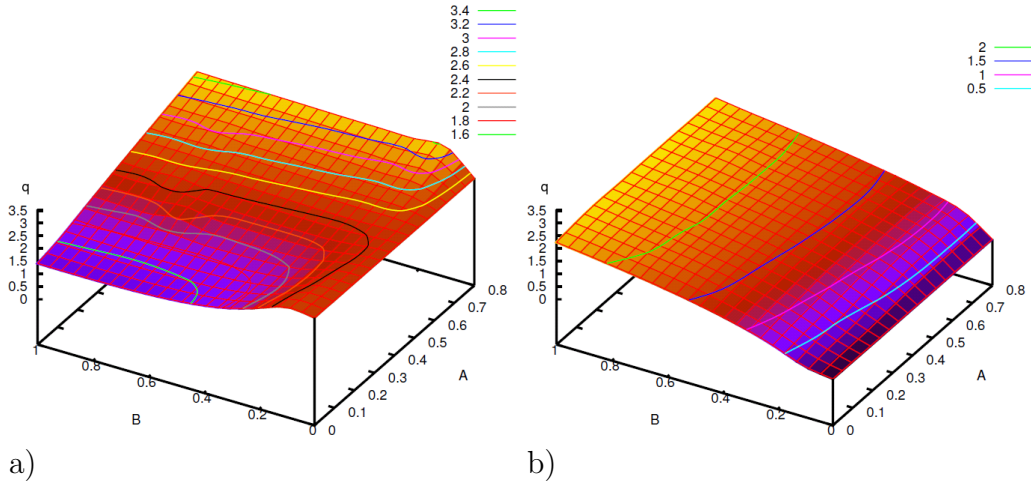


Figure 5.7: Quality measure for geometries depending on parameters A and B for a) the joint and b) the concrete.

As Fig. 5.7 a) depicts, the geometry is optimal with respect to the adhesive joint in case of a small width value of parameter A and a large depth parameter B. The influence of parameter A dominates the influence of parameter B. Fig. 5.7 b) reveals that the largest principal stress in the concrete on volumetric average is small, especially if the width parameter A is small and the depth parameter B is small as well. It is obvious, that the influence of parameter B dominates the influence of parameter A in this case.

In summary a small parameter A leads to the best results, hence the principal geometry type b) from Fig. 5.1 of triangular teeth is optimal. For parameter B a reasonable compromise has to be found depending on the exact problem at hand, as the exact results obviously are influenced by the contrast of the two YOUNG'S moduli E_{concrete} and E_{joint} .

This example underlines that XFEM is well-suited for this type of problem formulations: It is easy to parameterize the geometry and the influence of

the geometry parameters on some simulation results is of interest. Since no remeshing is required, no numerical overhead is created when repeating the simulation with different geometry parameters multiple times.

5.2 Metal matrix composite AMC225xe

The significant improvements in mechanical performance of metal matrix composites (MMC) over unreinforced metal alloys are well-known. In this section the aluminum matrix composite AMC225xe, i.e. the aluminum alloy AA2124 reinforced with 25 vol.-% ultra fine silicon carbide (SiC) particles is investigated in detail. In order to be able to simulate the thermo-mechanical material behavior, a coupled procedure of computer modeling and experimental validation is created.

In a first step the microstructural details of the aluminum matrix composite AMC225xe are investigated by scanning electron microscopy and quantitatively evaluated by digital image software. For a later use of XFEM a generic level set description for such microstructures is created. This computer model of the material is adopted to the statistic geometric parameters of individual grains as well as the overall structure.

The deformation behavior for tensile and compressive loading is characterized in detailed experiments. A pronounced difference in plastic strain response between tension and compression is observed under monotonic loading. It can be caused by several influence factors, e.g. the residual stress distribution in the composite due to the heat treatment. The residual stresses are measured in the aluminum matrix of the MMC by X-ray stress analyses.

The numerical simulation of the production process including heat treatment. The cooling from 500°C to room temperature led to thermal residual stresses in good accordance with the experimental data.

In a second step a parameter study with some simplifying assumptions is carried out in order to train the material model parameters such that the simulation results under monotonic loading coincided with the experimental data.

Finally, putting the simulation steps together, a computer model of the material AMC225xe has been created such that the complex material behavior can be modeled in detail.

5.2.1 Geometric microstructure model

A two step approach is chosen to create a microstructure model of the metal matrix composite AMC225xe. In the first step a stochastic model for single

SiC particles is created. The model is chosen with respect to the shape of SiC particles as observed in scanning electron microscope (SEM) images from SiC powder.

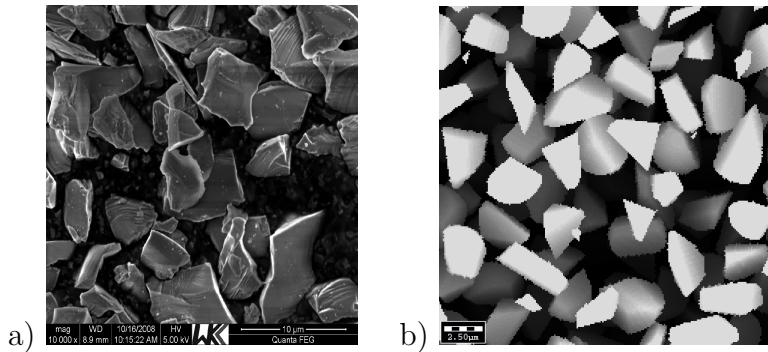


Figure 5.8: a) SEM image of SiC powder with 10,000x magnification, b) image of simulated particles.

The left image in Fig. 5.8 is a SEM image of SiC powder with 10,000x magnification. Please note that during the production process of AMC225xe this powder is further grinded and sifted with a 2-3 μm sieve. As SiC is brittle, it is assumed that the grinding process shatters the individual SiC particles into smaller ones of approximately the same shape.

The individual particles are defined by a more or less convex shape with some round edges and many plain sides with complex and sharp angled borders. To obtain a stochastic single particle model a sphere is generated with a radius r and multiple randomly oriented plains tangential to the sphere. The distance of the plains to the center of the sphere is $d_i < r$ for plain number i . Each plain then cuts away a spherical segment and if two plains intersect within the sphere, the resulting boundary of the generated particle is similar to the original particle. It has a convex shape with some round edges and many plain sides with complex and (mostly) sharp angled boundaries (cf. image b) in Fig. 5.8). The exact parameters for the individual generated particles are chosen in such a way that the particles should be able to pass through a 3 μm sieve as an upper limit for the size of the particles.

This stochastic single particle model is used to generate a complex microstructure of SiC particles within an aluminum matrix using a random sequential adsorption algorithm. This microstructure is used for a further validation of the single particle model. An analysis of SEM images of AMC225xe makes some information on random cut particles available. So far only the chord length distribution (cf. [Zhang et al., 2014]) has been taken into account for the validation of the single particle model. The reference values

from the micrographs are an average chord length of $1.73 \mu\text{m}$ [$0.63 \mu\text{m}$, $4.67 \mu\text{m}$], the average chord length from the stochastic model is $1.98 \mu\text{m}$ with a confidence interval of [$1.25 \mu\text{m}$, $2.72 \mu\text{m}$].

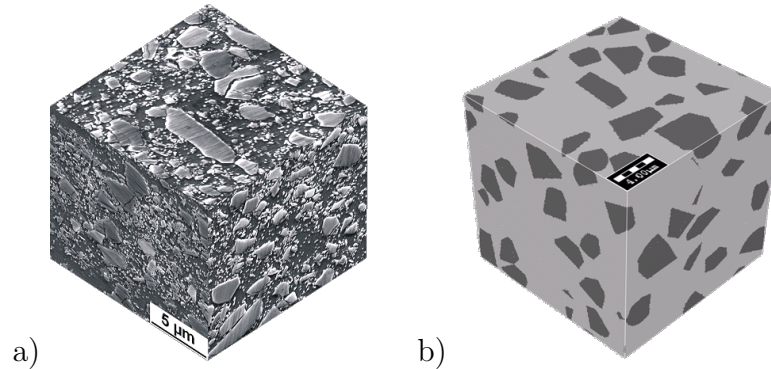


Figure 5.9: a) micrographs of AMC225xe, b) model of AMC225xe.

As can be observed in Fig. 5.9, there are few large particles of SiC in the microstructure of AMC225xe and additionally lots of tiny particles with diameters $\ll 1 \mu\text{m}$. This work does not consider multi-scale models, hence the larger particles are considered only in this microstructure model. The interested reader is referred to [Zhang et al., 2014], where a generalization of the here presented algorithm, derived from the very same, for creating a realistic microstructure is presented.

5.2.2 Experimental data

The aluminum matrix composite AMC225xe has been analyzed at the Institute of Materials Science and Engineering at the University of Kaiserslautern. For instance uniaxial loading experiments have been carried out. It struck that the material response under a compressive load is asymmetrical compared to the material response under tensile load.

Fig. 5.10 shows the stress-strain curve for a uniaxial tensile loading as well as a stress-strain curve for a uniaxial compressive loading.

The most likely explanation for this asymmetry are residual stresses of second order: During the production process of the AMC225xe, the material is cooled down in a so-called quenching process from the heat treatment temperature of above 500°C to room temperature (cf. [Materion Aerospace Metal Composites Limited, 2013]). During the resulting thermal contraction, the multi-phase material with different thermal expansion coefficients builds up residual stresses in each phase. This leads to tensile residual stresses in the

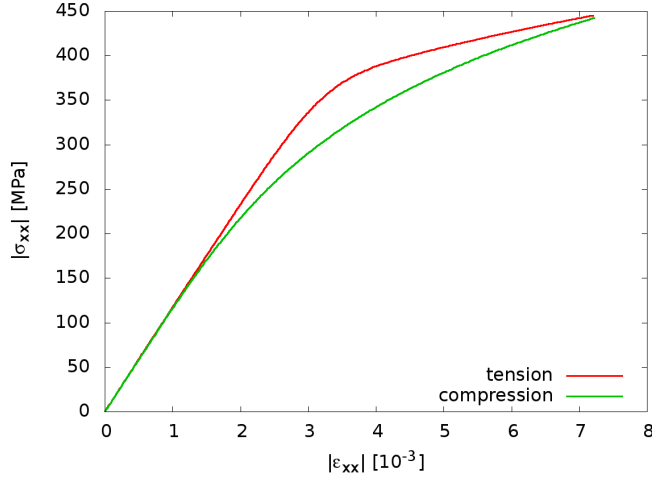


Figure 5.10: Asymmetry in stress strain diagram under uniaxial loading.

aluminum phase and compressive stress in the silicon carbide, where the tensile and compressive stress are equilibrated. Applying an external mechanical load, the residual stresses within the material, especially in combination with local plastification, lead to an asymmetrical material response.

Even though the exact type of materials in AMC225xe is known (aluminum matrix Al-Cu-Mg AA2124 and silicon carbide SiC_p particles with 25% solid volume fraction), lots of questions about the material parameters arise. On the one hand, for almost all material parameters the exact values are only known up to a certain precision, that is instead of a single value a whole interval is specified in literature (cf. for example [Granta Design Limited, 2009]). Hence, the inverse problem has to be solved, i.e. find material parameters such that the simulation result coincides with the experimental data.

On the other hand, many material parameters like the POISSON'S ratio, YOUNG'S modulus, thermal expansion coefficient and yield strength for the aluminum matrix and POISSON'S ratio for the silicon carbide particles are temperature dependent. They vary significantly during the quenching process as the temperature changes. Even when assuming a piecewise linear relation between most of the parameters and the temperature, this leads to a large parameter space for the inverse problem due to the sheer amount of variable parameters.

In order to circumvent the problem of the high dimensional problem, some simplifying assumptions are made and a hierarchical approach is carried out in the following parameter study.

5.2.3 Parameter study - solving the inverse problem

In order to separate the influence of the complex microstructure from the influence of the material parameters on the principal physical material behavior, the parameter study is carried out on a periodic cell of a regular microstructure.

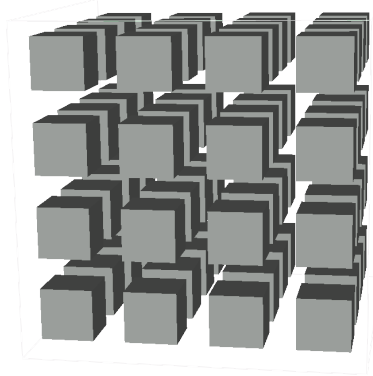


Figure 5.11: Fully periodic microstructure of 25 vol.-% SiC particles.

Fig. 5.11 shows an excerpt of the periodic microstructure. Due to symmetry reasons only one-eighth of a single particle has to be analyzed.

So far no information at all of the material response during the quenching phase is available, hence some simplifying assumptions have to be made for simulating this quenching process. First, it is assumed that at temperatures above 500°C both materials are in a stress free state. Second, it is assumed that at all times the temperature in the analyzed microstructure is constant over time. Both assumptions are reasonable as a) aluminum's yield strength is known to be close to zero at such a high temperature and b) compared to the tiny volume under consideration the cooling process is too slow to establish large temperature gradients.

For the parameter study the applied load is separated into two different steps. In a first step, the quenching process is simulated by applying a thermal load without a mechanical load. That is symmetry boundary conditions (as in (5.5)) are applied as well as a linear temperature cooling from 500°C to room temperature is simulated.

$$\begin{aligned}
 \mathbf{x} \in \{ 0 \times [0, 1] \times [0, 1] \} &\Rightarrow u_1 = 0, \\
 \mathbf{x} \in \{ [0, 1] \times 0 \times [0, 1] \} &\Rightarrow u_2 = 0, \\
 \mathbf{x} \in \{ [0, 1] \times [0, 1] \times 0 \} &\Rightarrow u_3 = 0,
 \end{aligned} \tag{5.5}$$

In a second step, the temperature is held constant at room temperature and

a mechanical uniaxial load is introduced. This is done by introducing a Neumann type boundary condition on a single surface of the volume element in addition to the symmetry boundary conditions and Neumann zero boundary conditions on the remaining surfaces. The load is modeled to increase linearly over time from 0 MPa up to 450 MPa. The applied force is always parallel to the outer surface normal vector of the surface it is applied on. As it is of interest to simulate an uniaxial tensile stress experiment as well as an uniaxial compression experiment, the simulated force is either directed towards the surface or away from it accordingly.

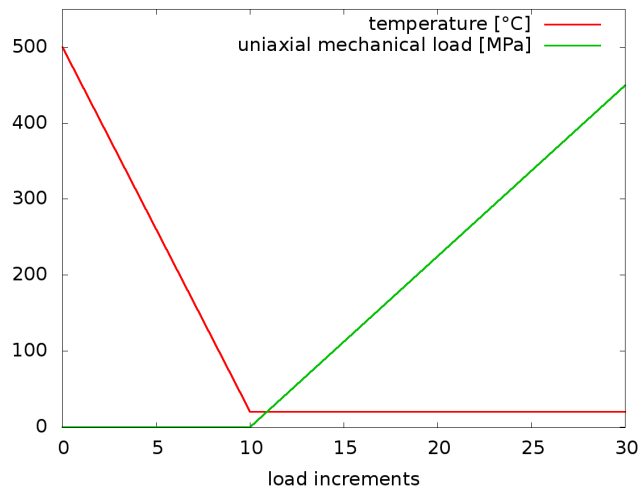


Figure 5.12: Boundary conditions over pseudo time in parameter study.

These steps of thermal load and mechanical load are visualized in Fig. 5.12. Please note how these loading steps are discretized. The whole load is split into 30 increments. This arbitrary number of increments is chosen as a reasonable trade-off between accuracy and computation time required for each simulation. The temperature load is linearly applied within the first 10 increments. The mechanical load of step two is applied linearly within the 20 increments. The resulting stress strain curve created from the 20 increments of the mechanical load then is compared to experimental data. Now a classical inverse problem is formulated. Find such material parameters for the simulation model such that the resulting stress-strain curve is fitting the experimental stress strain curve in the best possible way. Obviously, all material parameters have to be physically plausible.

When fitting a single curve to another one there are plenty of different possibilities to define a “good” fit. For the parameter study a hierarchical set of

curve characteristics is specified to define the “goodness of fit”.

- The initial slope of the linear part of the curves (equivalent to YOUNG’S modulus of homogenized reference material) was identified as the most important characteristic.
- As the simulation reproduces a stress controlled uniaxial loading experiment, the maximal strain observed is a crucial characteristic as well.
- The L_2 -error $\|\sigma_{xx}^{\text{simulation}} - \sigma_{xx}^{\text{experiment}}\|_{L_2(0, \varepsilon_{xx}^{\text{max}})}$ between the simulated curve and the experimental data.

Obviously, such a multicriterial optimization with a huge parameter space is nontrivial. Therefore, an adaptive scheme starting with a plausible set of material parameters is created. In a first step, the material parameters with the largest influence on our hierarchical multicriterial “goodness of fit” are identified. This leads to a grouping of material parameters according to their influence. These groups of parameters are then optimized one after the other, starting with the one with the assumed largest influence on the “goodness of fit”. The parameters in the other groups are held constant during the optimization of each group.

It is obvious that two possible sources for errors are introduced with this approach. First, it is not clear a-priori that if a certain variable has a large influence on the “goodness of fit” at a certain point in the high-dimensional parameter space, that it still has a large influence when the other parameters are changed. Second, this approach is deliberately reducing the dimensionality of the parameter space to analyze as more or less certain dimensions are coupled. Therefore, it may be the case that a globally optimal set of parameters is excluded from the analysis. As a complete analysis of the full parameter space is out of scope because the required computing time is way out of league. These two drawbacks are accepted as a good trade-off between accuracy and feasibility.

So far this study has been carried out for tensile loading and compressive loading separately. A good result for the tensile loading with still a reasonable result for compressive loading is visualized in Fig. 5.13.

The material parameters of silicon carbide are assumed to be of linear relation with respect to temperature. For the aluminum phase a piecewise linear relation is assumed with the three supporting points at temperature $\theta_1 = 25^\circ\text{C}$, $\theta_2 = 262.5^\circ\text{C}$ and $\theta_3 = 500^\circ\text{C}$. The resulting material parameters are

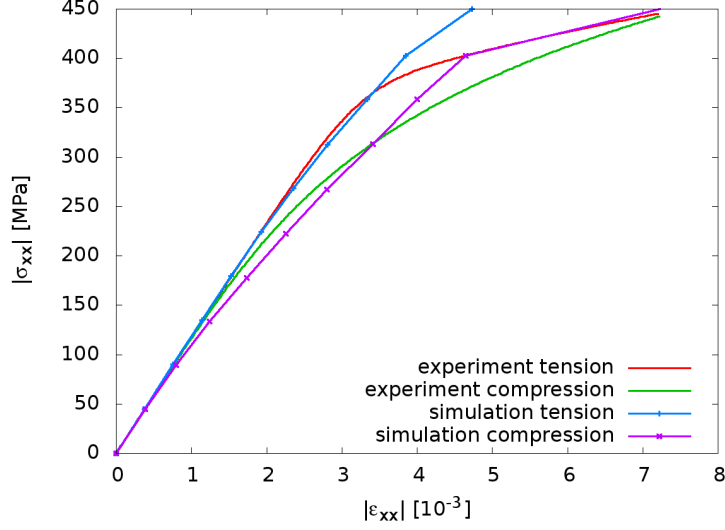


Figure 5.13: Stress-Strain diagram comparing simulated material response with experiments.

for the aluminum

$$\begin{aligned}
\alpha_{Al}(\theta_1) &= 22 \text{ microstrain}/^\circ\text{C}, \\
\alpha_{Al}(\theta_2) &= 27.25 \text{ microstrain}/^\circ\text{C}, \\
\alpha_{Al}(\theta_3) &= 32.5 \text{ microstrain}/^\circ\text{C}, \\
E_{Al}(\theta_1) &= 75.7 \text{ GPa}, \\
E_{Al}(\theta_2) &= 55 \text{ GPa}, \\
E_{Al}(\theta_3) &= 10 \text{ GPa}, \\
\nu_{Al}(\theta_1) &= 0.33, \\
\nu_{Al}(\theta_2) &= 0.355, \\
\nu_{Al}(\theta_3) &= 0.38, \\
\sigma_{y,Al}(\theta_1) &= 400 \text{ MPa}, \\
\sigma_{y,Al}(\theta_2) &= 50 \text{ MPa}, \\
\sigma_{y,Al}(\theta_3) &= 20 \text{ MPa}, \\
m_{Al}(\theta_1) &= 0.6, \\
m_{Al}(\theta_2) &= 0.6, \\
m_{Al}(\theta_3) &= 0.6, \\
\tilde{h}_{Al}(\theta_1) &= 1250, \\
\tilde{h}_{Al}(\theta_2) &= 416.67, \\
\tilde{h}_{Al}(\theta_3) &= 0
\end{aligned} \tag{5.6}$$

and for the silicon carbide

$$\begin{aligned}
 \alpha_{\text{SiC}}(\theta_1) &= 2.78 \text{ microstrain}/^\circ\text{C}, \\
 \alpha_{\text{SiC}}(\theta_3) &= 5.09 \text{ microstrain}/^\circ\text{C}, \\
 E_{\text{SiC}}(\theta_1) &= 450 \text{ GPa}, \\
 E_{\text{SiC}}(\theta_3) &= 450 \text{ GPa}, \\
 \nu_{\text{SiC}}(\theta_1) &= 0.18, \\
 \nu_{\text{SiC}}(\theta_3) &= 0.18.
 \end{aligned} \tag{5.7}$$

5.2.4 Simulation on complex microstructure

In this section the result of the simulation of a complex microstructure is presented. An excerpt of microstructure from Fig. 5.9 b) is taken and the boundary conditions of (5.5) and Fig. 5.12 are applied. The material parameters are taken from the results of the parameter study presented in section 5.2.3. Fig. 5.14 shows the silicon carbide particles in the microstructure. The colors represent the level set values $\Phi(\mathbf{x})$ (signed distance) inside the particles.

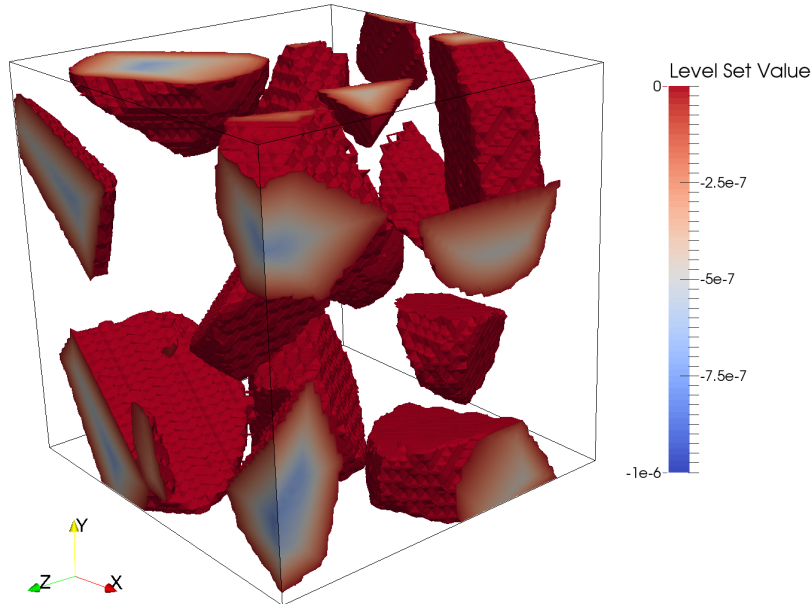


Figure 5.14: Distribution of silicon carbide particles, level set values $\Phi(\mathbf{x})$ plotted.

Fig. 5.15 depicts the magnitude of the elastic part of the strain tensor $\|\boldsymbol{\varepsilon}^{\text{el}}\|$ in the material. As expected the strain in the silicon carbide particles is by

magnitudes smaller than in the aluminum, because of the significantly larger YOUNG'S modulus.

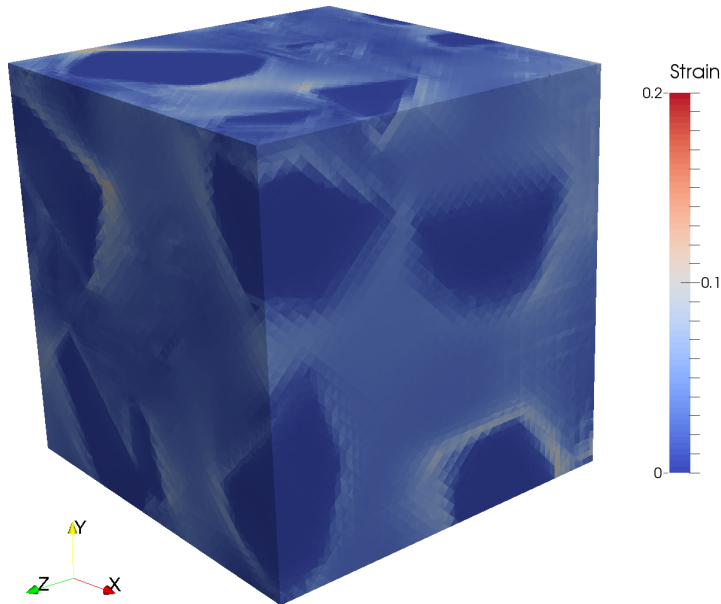


Figure 5.15: Strain in the RVE.

At a first glance it seems surprising that the largest elastic strain in the aluminum phase occurs in the vicinity of the interface to silicon carbide particles. With a closer look on the plastic strain this can be easily explained. Fig. 5.16 visualizes the plastic strain in the material.

Obviously, no plastic strain occurs in the silicon carbide particles. As the thermal expansion coefficients of the two materials differ by a whole magnitude during the complete cool-down period, large shear stresses occur at the interface during the quenching process. This leads to comparably huge deformations in the vicinity of the material interface. As the yield strength of the aluminum is exceeded, huge parts of the deformation are plastic deformations but not exclusively, hence the strain peaks in the vicinity of the material interface.

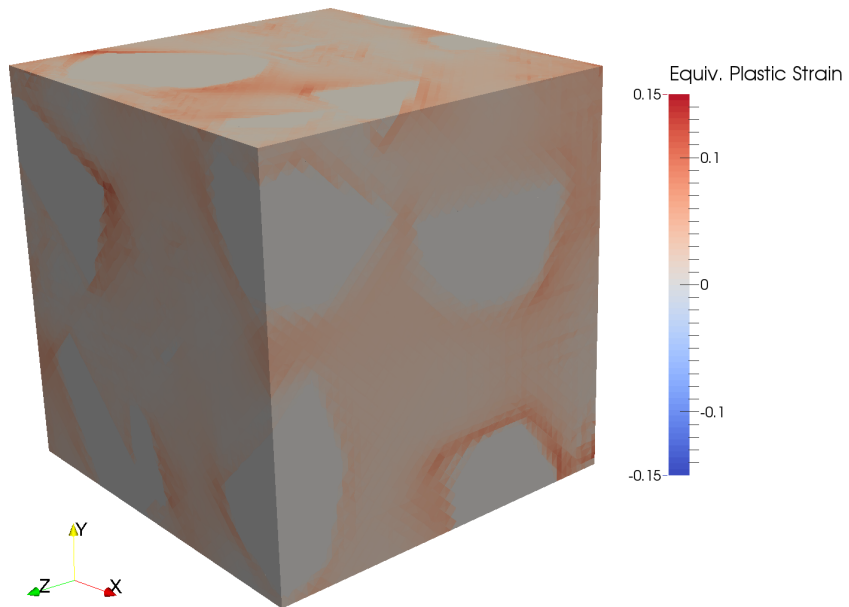


Figure 5.16: Equivalent plastic strain in the RVE.

Chapter 6

Conclusions

Over the last years the extended finite element method has become a standard means for simulating micromechanical material behavior. Its advantages in terms of discretization errors of the XFEM over the standard FEM is well-known (cf. for example [Fries and Belytschko, 2010]) and this work adds some more insights of the advantages of XFEM over FEM. A nontrivial example for a three-dimensional bimaterial problem is created, for which the analytical displacement solution can be derived. Both, standard FEM and XFEM solutions for multiple finite element mesh discretizations are compared to the analytical solution. A special examination routine is created that allows to capture the solution error in the material interface region. It is shown that the XFEM is superior to the FEM in capturing the jump in the strain field across the interface. It is also shown that the overall error of the XFEM is significantly smaller than the error of the standard FEM for all finite element meshes under consideration. Additionally, the convergence rate of the XFEM is significantly larger than the convergence rate of the standard FEM.

One of the major drawbacks of the XFEM for bimaterial problems is documented well in the literature (cf. again for example [Fries and Belytschko, 2010]): The XFEM problem becomes ill-posed when nodal level set values are too close to zero, which corresponds to a node of the finite element mesh being too close to the material interface.

To the author's surprise an extensive literature study did not bring up a single publication analyzing this problem in detail. A trivial one-dimensional example is used to create a dependence of the problem condition to the minimal distance between a node and the interface. It is discovered that the problem becomes ill-posed with quadratic order depending on parameter \hat{h} describing the minimal distance between a node and the interface.

A trivial three-dimensional problem of specific example situations is analyzed in detail as well and the results strongly suggest the same quadratic relation of the ill-posedness depending on parameter \hat{h} .

Based on this finding, the existing methods of stabilizing the XFEM are re-evaluated and a novel stabilization algorithm that combines movement of nodes and mesh regularization techniques is presented. It is demonstrated that the algorithm is able to reduce the condition of the global stiffness matrix significantly. Additionally, it is shown that the algorithm has a major

advantage over traditional methods for stabilizing the XFEM:

The algorithm is able to reduce unphysical stress peaks as well as stress oscillations in the region of material interfaces.

So far, the algorithm cannot guarantee to reduce all unphysical stress peaks, as it depends on the exact combination of the layout of the underlying finite element mesh and the geometry and a large multitude of parameters. Nevertheless, it is a promising novel approach for optimizing the XFEM that has to be analyzed further in future work.

As an example application for the XFEM, adhesive joints in concrete are analyzed. The advantage of the XFEM being able to analyze geometries independent of the underlying finite element mesh is demonstrated in detail. This is done by carrying out a parameter study concerning the joint geometry without having to adopt the underlying mesh.

Furthermore, this work presents a complex framework for simulating mechanical properties of the metal matrix composite AMC225xe. First, a statistically validated stochastic model for the particle geometry is created. Second, the material parameters of the model are fitted with a huge parameter study according to experimental uniaxial loading tests. Combining the results of the geometry model with the solution of the inverse problem of finding correct material parameters, a ready to use framework is created for analyzing the metal matrix composite in further detail.

6.1 Future work

Concerning the influence of the mesh parameter \hat{h} on the condition of the XFEM bimaterial problem, it is planned to analyze more three-dimensional problem situations. Therewith, it should be possible to further back up the working hypothesis of a quadratic relation between the mesh parameter \hat{h} and the condition of the XFEM bimaterial problem.

Multiple starting points for future work originate in the novel XFEM stabilization algorithm. A study of the influence of the algorithmic parameters on the problem condition and the reduction of unphysical stress peaks is of obvious importance. Also, the algorithm has to be tested for robustness concerning the exact geometry in relation to the underlying finite element mesh. Additionally, a detailed comparison of this novel algorithm to XFEM stabilization potential of the algebraic stabilization schemes presented in [Löhnert, 2014] is recommended for future work.

For the simulatory framework for simulating mechanical properties of the metal matrix composite AMC225xe it is planned to further validate the stochastic model as soon as more statistical data of the original material

is available. Finally, it is planned to analyze the influence of specific changes of the geometry on the effective material properties of the material in detail. Considering the parameter study of adhesive joints in concrete it is planned to combine the XFEM with a three-dimensional spline parametrization of the adhesive joints. This seems to create a promising bundle of methodology that should easily be transferred to other types of micromechanical problems.

Chapter A

Appendix

A.1 Higher order terms in XFEM approximation

The XFEM formulation with the standard enhanced abs enrichment by MOËS (cf. [Moës et al., 2003]) reads

$$u^h(\mathbf{x}) = \sum_{i \in \bar{\mathcal{N}}_h} \varphi^{i,h}(\mathbf{x}) u_i + \sum_{i \in \bar{\mathcal{N}}_h^*} \tilde{\varphi}^{i,h}(\mathbf{x}) a_i, \quad (\text{A.1})$$

with

$$\tilde{\varphi}^{i,h}(\mathbf{x}) = \varphi^{i,h}(\mathbf{x}) \left(\sum_{j \in K(\mathbf{x})} |\phi_j| \varphi^{j,h}(\mathbf{x}) - \left| \sum_{j \in K(\mathbf{x})} \phi_j \varphi^{j,h}(\mathbf{x}) \right| \right). \quad (\text{A.2})$$

When assuming the polynomial shape functions to be of n -th order, denoted with

$$\mathcal{O}(\varphi^{i,h}(\mathbf{x})) = \mathcal{O}(\mathbf{x}^n), \quad (\text{A.3})$$

it becomes immediately clear that the shape functions of the enriched degrees of freedom may contain terms of order

$$\mathcal{O}(\tilde{\varphi}^{i,h}(\mathbf{x})) = \mathcal{O}(\mathbf{x}^{2n}), \quad (\text{A.4})$$

independently of the exact choice of the shape functions.

Nevertheless, when computing the sum over all enrichment shape functions

of an enriched element at any given point \mathbf{x} inside this element, it reads

$$\begin{aligned}
\sum_{i \in K(\mathbf{x})} \tilde{\varphi}^{i,h}(\mathbf{x}) &= \sum_{i \in K(\mathbf{x})} \left(\varphi^{i,h}(\mathbf{x}) \left(\sum_{j \in K(\mathbf{x})} |\phi_j| \varphi^{j,h}(\mathbf{x}) - \left| \sum_{j \in K(\mathbf{x})} \phi_j \varphi^{j,h}(\mathbf{x}) \right| \right) \right) \\
&= \left(\sum_{j \in K(\mathbf{x})} |\phi_j| \varphi^{j,h}(\mathbf{x}) - \left| \sum_{j \in K(\mathbf{x})} \phi_j \varphi^{j,h}(\mathbf{x}) \right| \right) \underbrace{\sum_{i \in K(\mathbf{x})} \varphi^{i,h}(\mathbf{x})}_{=1, \text{ partition of unity}} \\
&= \sum_{j \in K(\mathbf{x})} |\phi_j| \varphi^{j,h}(\mathbf{x}) - \left| \sum_{j \in K(\mathbf{x})} \phi_j \varphi^{j,h}(\mathbf{x}) \right| \\
&= \mathcal{O}(\mathbf{x}^n).
\end{aligned} \tag{A.5}$$

From (A.5) it becomes obvious, that the standard enhanced abs enrichment by MÖES is able to do exactly what it is designed to do. It reproduces polynoms of order $\mathcal{O}(\mathbf{x}^n)$ with a kink at the predefined interface. This is because the interface is defined as all points where the level set function has a zero value and as the level set function is approximated via the standard shape functions this condition reads

$$\sum_{j \in K(\mathbf{x})} \phi_j \varphi^{j,h}(\mathbf{x}) = 0. \tag{A.6}$$

Inserting this into (A.5) shows directly the kink at these points. From A.1 to (A.5) it now becomes clear that the approximation function is of order

$$\mathcal{O}(u^h(\mathbf{x})) = \begin{cases} \mathcal{O}(\mathbf{x}^n) \Leftrightarrow a_i = a_j \quad \forall i, j \in K(\mathbf{x}) \\ \mathcal{O}(\mathbf{x}^{2n}) \Leftrightarrow \exists i, j \in K(\mathbf{x}) : a_i \neq a_j \quad \text{i.g.} \end{cases} \tag{A.7}$$

This section now takes a closer look at the cases where $\exists i, j \in K(\mathbf{x}) : a_i \neq a_j$ and hence the order of the discretized displacement function is of higher order than expected.

In section 4.1 a one-dimensional example for XFEM is introduced, where a one-dimensional bar of length 1 with an interface at position $x = a$ is discretized with a single enriched element. The displacement field, using linear shape functions, then reads for $x \in [0, a]$

$$u^{h-}(x) = (1-x)u_1 + xu_2 + (1-x)(2x-2ax)a_1 + x(2x-2ax)a_2 \tag{A.8}$$

and for $x \in [a, 1]$

$$u^{h+}(x) = (1-x)u_1 + xu_2 + (1-x)(2a-2ax)a_1 + x(2a-2ax)a_2, \quad (\text{A.9})$$

with the two displacement unknowns u_1 and u_2 as well as the two enrichment unknowns a_1 and a_2 . Reordering the terms yields

$$u^{h-}(x) = x^2(-2(1-a)(a_1-a_2)) + x(-u_1+u_2+(2-2a)a_1) + u_1 \quad (\text{A.10})$$

and

$$u^{h+}(x) = x^2(2a(a_1-a_2)) + x(-u_1+u_2-4aa_1+2aa_2) + (u_1+2aa_1). \quad (\text{A.11})$$

If and only if $a_1 = a_2$ both quadratic terms vanish, as the parameter a describes the position of the interface somewhere in the interval $(0, 1)$. Additionally, it follows from $a \in (0, 1)$ that the coefficient of the quadratic terms changes its sign from u^{h-} to u^{h+} .

Of special interest is, what type of quadratic functions can be reproduced with this type of function. The general case of quadratic polynomials with a kink at position a reads

$$\tilde{u}^-(x) = c_1x^2 + c_2x + c_3, \quad x \in [0, a] \quad (\text{A.12})$$

and

$$\tilde{u}^+(x) = c_4x^2 + c_5x + c_6, \quad x \in [a, 1] \quad (\text{A.13})$$

with

$$\tilde{u}^-(a) = \tilde{u}^+(a). \quad (\text{A.14})$$

In general these polynomials cannot be reproduced by one enriched XFEM element using linear shape functions as (A.10) and (A.11) display. The consistency condition (A.14) and a trivial comparison of the coefficients of the polynomials yields that a general quadratic polynomial can be reproduced if and only if the following two requirements are fulfilled

$$\begin{aligned} (1) \quad \exists d \in \mathbb{R} : \quad & \begin{cases} c_1 = d(|\phi_1| + \phi_1 - (|\phi_2| + \phi_2)) \\ c_4 = d(|\phi_1| - \phi_1 - (|\phi_2| - \phi_2)), \end{cases} \quad (\text{A.15}) \\ (2) \quad & c_3 = a^2c_1 - ac_2 + ac_5 + c_6, \end{aligned}$$

with the nodal level set values ϕ_i at node i . Introducing the abbreviations

$$\begin{aligned} \varphi_{ij}^- &= |\phi_i| + \phi_i - (|\phi_j| + \phi_j), \\ \varphi_{ij}^+ &= |\phi_i| - \phi_i - (|\phi_j| - \phi_j) \end{aligned} \quad (\text{A.16})$$

and evaluating these for the nodal level set values this yields

$$\begin{aligned}\varphi_{12}^- &= |-a| + (-a) - (|1-a| + (1-a)) = -2(1-a), \\ \varphi_{12}^+ &= |-a| - (-a) - (|1-a| - (1-a)) = 2a.\end{aligned}\tag{A.17}$$

For the quadratic polynomials with a possible kink at position a that can be reproduced with a single enriched element. This results in

$$\tilde{u}(x) = \begin{cases} 2d_1(a-1)x^2 + d_2x + d_5 & , x \in [0, a] \\ 2d_1ax^2 + d_3x + d_4 & , x \in [a, 1], \end{cases}\tag{A.18}$$

with the consistency condition

$$d_5 = a(2d_1a - d_2 + d_3) + d_4.\tag{A.19}$$

Comparing the coefficients yields

$$\begin{aligned}d_1 &= a_1 - a_2, \\ d_2 &= -u_1 + u_2 + (2-2a)a_1, \\ d_3 &= -u_1 + u_2 - 4aa_1 + 2aa_2, \\ d_4 &= u_1 + 2aa_1,\end{aligned}\tag{A.20}$$

which can also be expressed in matrix notation with

$$\begin{pmatrix} d_1 \\ d_2 \\ d_3 \\ d_4 \end{pmatrix} = \underbrace{\begin{pmatrix} 0 & 0 & 1 & -1 \\ -1 & 1 & 2-2a & 0 \\ -1 & 1 & -4a & 2a \\ 1 & 0 & 2a & 0 \end{pmatrix}}_{=: A} \begin{pmatrix} u_1 \\ u_2 \\ a_1 \\ a_2 \end{pmatrix}.\tag{A.21}$$

For parameter $a \in (0, 1)$ the matrix A is invertible and for a given polynomial of the type specified in (A.18) fulfilling the consistency condition (A.19) the XFEM solution reads

$$\begin{pmatrix} u_1 \\ u_2 \\ a_1 \\ a_2 \end{pmatrix} = \begin{pmatrix} 2a^2 & -a & a & 1 \\ 2a & 0 & 1 & 1 \\ -a & \frac{1}{2} & -\frac{1}{2} & 0 \\ \frac{1}{2}(-2a-2) & \frac{1}{2} & -\frac{1}{2} & 0 \end{pmatrix} \begin{pmatrix} d_1 \\ d_2 \\ d_3 \\ d_4 \end{pmatrix}.\tag{A.22}$$

In the three-dimensional case, considering a tetrahedral element with linear shape functions, also some quadratic functions can be reproduced by a sin-

gle XFEM enriched element with linear shape functions. The procedure of deriving the reproducible quadratic polynoms with kinks at the interface is analogous to the one-dimensional case. Assume the tetrahedron to be the unit tetrahedron consisting of the four nodes

$$\begin{aligned} n_1 &= (0; 0; 0), \\ n_2 &= (1; 0; 0), \\ n_3 &= (0; 1; 0), \\ n_4 &= (0; 0; 1), \end{aligned} \tag{A.23}$$

where the four corresponding level set values are denoted by ϕ_1, \dots, ϕ_4 . Each individual component of the reproducible quadratic polynoms must be of the form

$$\tilde{u}(\mathbf{x}) = \begin{cases} \tilde{u}^-(\mathbf{x}) & , \phi(\mathbf{x}) \leq 0 \\ \tilde{u}^+(\mathbf{x}) & , \phi(\mathbf{x}) \geq 0 \end{cases} \tag{A.24}$$

with

$$\begin{aligned} \tilde{u}^-(\mathbf{x}) &= x^2 d_1 (\varphi_2^- - \varphi_1^-) + y^2 d_2 (\varphi_3^- - \varphi_1^-) + z^2 d_3 (\varphi_4^- - \varphi_1^-) \\ &+ xy ((\varphi_3^- - \varphi_1^-)d_1 + (\varphi_2^- - \varphi_1^-)d_2) \\ &+ xz ((\varphi_4^- - \varphi_1^-)d_1 + (\varphi_2^- - \varphi_1^-)d_3) \\ &+ yz ((\varphi_4^- - \varphi_1^-)d_2 + (\varphi_3^- - \varphi_1^-)d_3) \\ &+ xd_4 + yd_5 + zd_6 + d_7 \end{aligned} \tag{A.25}$$

and

$$\begin{aligned} \tilde{u}^+(\mathbf{x}) &= x^2 d_1 (\varphi_2^+ - \varphi_1^-) + y^2 d_2 (\varphi_3^+ - \varphi_1^-) + z^2 d_3 (\varphi_4^+ - \varphi_1^-) \\ &+ xy ((\varphi_3^+ - \varphi_1^-)d_1 + (\varphi_2^+ - \varphi_1^-)d_2) \\ &+ xz ((\varphi_4^+ - \varphi_1^-)d_1 + (\varphi_2^+ - \varphi_1^-)d_3) \\ &+ yz ((\varphi_4^+ - \varphi_1^-)d_2 + (\varphi_3^+ - \varphi_1^-)d_3) \\ &+ xd_8 + yd_9 + zd_{10} + d_{11}, \end{aligned} \tag{A.26}$$

where again the level set term abbreviations of (A.16) are used. Analogously to the one-dimensional case a consistency condition is required. This time it is not defined at a single point, but for the whole iso-zero surface of the level set function $\phi(\mathbf{x})$

$$\tilde{u}^-(\mathbf{x}) = \tilde{u}^+(\mathbf{x}) \quad \forall \mathbf{x} \in \{\mathbf{x} \in \Omega \mid \phi(\mathbf{x}) = 0\}. \tag{A.27}$$

Depending on the exact layout of the interface, different restrictions on the coefficients are introduced. Without going into further details it is sufficient

to state that a quadratic polynomial can be reproduced by the enhanced abs enrichment used in this work if and only if it fulfills (A.25), (A.26) and (A.27).

A.2 Function spaces

As in section 3.1 certain function spaces for vector-valued functions in \mathbb{R}^d for $d \in \mathbb{N}$ are required, they are introduced here. The interested reader is also referred to [Bronstein et al., 2001].

Let $\Omega \subset \mathbb{R}^d$ be open and bounded. The space of square integrable functions on Ω then is defined as

$$L^2(\Omega) = \left\{ v : \Omega \rightarrow \mathbb{R} \left| \int_{\Omega} v^2 dx < \infty \right. \right\}, \quad (\text{A.28})$$

with the norm

$$\|u\| = \sqrt{(u, u)_{L^2(\Omega)}}, \quad (\text{A.29})$$

where the inner product is defined as follows

$$(u, v)_{L^2(\Omega)} = \int_{\Omega} uv dx \quad (\text{A.30})$$

Two elements $u \in L^2(\Omega)$ and $v \in L^2(\Omega)$ are called equal, that is $u = v$, if and only if

$$u = v \Leftrightarrow u(\mathbf{x}) = v(\mathbf{x}) \quad \forall \mathbf{x} \in \Omega \setminus N, \quad (\text{A.31})$$

where N is a set of measure zero. The generalization of $L^2(\Omega)$ to vector-valued functions $[L^2(\Omega)]^3$ is straightforward by generalizing the scalar-product and norm to a higher dimension $d \in \mathbb{N}$

$$\|\mathbf{u}\| = \sqrt{(\mathbf{u}, \mathbf{u})_{[L^2(\Omega)]^d}} \quad (\text{A.32})$$

with

$$(\mathbf{u}, \mathbf{v})_{[L^2(\Omega)]^d} = \sum_{i=1}^d \int_{\Omega} u_i v_i dx, \quad (\text{A.33})$$

where \mathbf{u} and \mathbf{v} are now vector-valued functions with components in $L^2(\Omega)$. Additionally, later on for the finite element discretizations, the concept of weak derivatives is applied. For defining a weak derivative, some preliminaries are needed. Let $u \in \mathcal{D}'(\Omega)$ be a distribution (see [Schwartz, 1966] or

[Ern and Guermond, 2004]) and let $\boldsymbol{\alpha} = (\alpha_1, \dots, \alpha_d)^T$ be a multi-index (cf. [Saint Raymond, 1991]) with

$$|\boldsymbol{\alpha}| = \sum_{i=1}^d \alpha_i. \quad (\text{A.34})$$

The weak derivative $D^\alpha u$ is then defined as

$$\int_{\Omega} D^\alpha u \zeta \, dx = (-1)^{|\boldsymbol{\alpha}|} \int_{\Omega} u D^\alpha \zeta \, dx \quad \forall \zeta \in C_0^\infty(\Omega), \quad (\text{A.35})$$

with

$$D^\alpha u = \frac{\partial^{|\boldsymbol{\alpha}|} u}{\partial x_1^{\alpha_1} \dots \partial x_n^{\alpha_n}}, \quad (\text{A.36})$$

where $C_0^\infty(\Omega)$ is the class of functions infinitely many times continuously differentiable with compact support.

With the help of weak derivatives now the SOBOLEV space $H^1(\Omega)$ can be introduced,

$$H^1(\Omega) = \{u \in L^2(\Omega) \mid D^\alpha u \in L^2(\Omega) \forall |\boldsymbol{\alpha}| \leq 1\}, \quad (\text{A.37})$$

where $D^\alpha u$ has to be understood as a weak derivative as in (A.35) and is equipped with a scalar product

$$(u, v)_{H^1(\Omega)} = \sum_{|\boldsymbol{\alpha}| \leq 1} \int_{\Omega} D^\alpha u D^\alpha v \, dx. \quad (\text{A.38})$$

With the induced norm

$$\|u\|_{H^1(\Omega)} = \sqrt{(u, u)_{H^1(\Omega)}}, \quad (\text{A.39})$$

it can be shown that the space $H^1(\Omega)$ defines a HILBERT space (see for example [Alt, 2007]). The derived function space for vector fields in \mathbb{R}^d then reads

$$\mathcal{V} = [H^1(\Omega)]^d = \{\mathbf{v} = (v_1, \dots, v_d)^T \mid v_i \in H^1(\Omega), i = 1, \dots, d\} \quad (\text{A.40})$$

With the scalar product

$$(\mathbf{u}, \mathbf{v})_{[H^1(\Omega)]^d} = \sum_{i=1}^d (u_i, v_i)_{H^1(\Omega)} \quad (\text{A.41})$$

the space \mathcal{V} is a SOBOLEV space (cf. [Alt, 2007]).

A.3 Continuum mechanical trivia

A.3.1 Contraction of tensors

A double contraction of tensors is denoted by “:”. In case of fourth order tensor and second order tensor this yields a second order tensor

$$\mathbf{C} : \boldsymbol{\varepsilon} = \mathbb{C}_{ijkl} \varepsilon_{kl} \mathbf{e}_i \otimes \mathbf{e}_j. \quad (\text{A.42})$$

In case of two second order tensors this yields a scalar value

$$\boldsymbol{\sigma} : \boldsymbol{\varepsilon} = \sigma_{ij} \varepsilon_{ij}. \quad (\text{A.43})$$

A single contraction of tensors or vectors is described by “·”. In case of second order tensor and a vector this yields a vector

$$\boldsymbol{\sigma} \cdot \mathbf{n} = \sigma_{ij} n_j \mathbf{e}_i. \quad (\text{A.44})$$

In case of two vectors this yields the scalar product and hence, a scalar value

$$\mathbf{n} \cdot \mathbf{b} = n_i b_i. \quad (\text{A.45})$$

A.3.2 Rigid body motion

A body Ω is said to undergo a rigid body motion, if it is rotated or translated (or both) in space without deforming the body. Any rigid body motion can be expressed in the following form

$$\mathbf{x}(\mathbf{X}, t) = \mathbf{R}(t) \cdot \mathbf{X} + \mathbf{v}_T(t) \quad \forall \mathbf{x} \in \varphi(\mathbf{X}), \quad (\text{A.46})$$

with $\mathbf{R}(t)$ denoting a rotation tensor and $\mathbf{v}_T(t)$ denoting a translation that are both independent from \mathbf{X} . Every rigid body motion is well-defined by specifying six parameters, that is three rotation angles and three translational degrees of freedom.

A.3.3 Derivative of the norm of stress tensor deviator

In (2.49) the term $\partial \|\text{dev}(\boldsymbol{\sigma})\| / \partial \boldsymbol{\sigma}$ occurs. In order to derive this, in a first step the chain rule is applied

$$\frac{\partial \|\text{dev}(\boldsymbol{\sigma})\|^2}{\partial \boldsymbol{\sigma}} = 2 \|\text{dev}(\boldsymbol{\sigma})\| \frac{\partial \|\text{dev}(\boldsymbol{\sigma})\|}{\partial \boldsymbol{\sigma}}. \quad (\text{A.47})$$

On the other hand, when using the definition of the deviator and the index notation one obtains

$$\begin{aligned} \frac{\partial \|\text{dev}(\boldsymbol{\sigma})\|^2}{\partial \boldsymbol{\sigma}} &= \frac{\partial}{\partial \sigma_{lm}} \left(\left(\sigma_{ij} - \frac{1}{3} \sigma_{kk} \delta_{ij} \right) \left(\sigma_{ij} - \frac{1}{3} \sigma_{kk} \delta_{ij} \right) \right) \\ &= \frac{\partial}{\partial \sigma_{lm}} \left(\sigma_{ij} \sigma_{ij} - \frac{2}{3} \sigma_{ij} \sigma_{kk} \delta_{ij} + \frac{1}{9} \delta_{ij} \delta_{ij} \sigma_{kk} \sigma_{kk} \right) \\ &= 2 \sigma_{ij} \delta_{il} \delta_{jm} - \frac{2}{3} \delta_{il} \delta_{jm} \sigma_{kk} \delta_{ij} - \frac{2}{3} \sigma_{ij} \delta_{ij} \delta_{lm} + \frac{2}{9} \delta_{ij} \delta_{ij} \sigma_{kk} \delta_{lm} \\ &= 2 \sigma_{lm} - \frac{2}{3} \sigma_{kk} \delta_{lm} - \frac{2}{3} \sigma_{ij} \delta_{ij} \delta_{lm} + \frac{2}{9} \delta_{ij} \delta_{ij} \sigma_{kk} \delta_{lm} \\ &= 2 \sigma_{lm} - \frac{2}{3} \sigma_{kk} \delta_{lm} - \frac{2}{3} \sigma_{kk} \delta_{lm} + \frac{2}{3} \sigma_{kk} \delta_{lm} \\ &= 2 \sigma_{lm} - \frac{2}{3} \sigma_{kk} \delta_{lm} \\ &= 2 \text{dev}(\boldsymbol{\sigma}). \end{aligned} \quad (\text{A.48})$$

Now combining (A.47) and (A.48) yields

$$2 \|\text{dev}(\boldsymbol{\sigma})\| \frac{\partial \|\text{dev}(\boldsymbol{\sigma})\|}{\partial \boldsymbol{\sigma}} = 2 \text{dev}(\boldsymbol{\sigma}) \quad (\text{A.49})$$

and therewith

$$\frac{\partial \|\text{dev}(\boldsymbol{\sigma})\|}{\partial \boldsymbol{\sigma}} = \frac{\text{dev}(\boldsymbol{\sigma})}{\|\text{dev}(\boldsymbol{\sigma})\|}. \quad (\text{A.50})$$

A.3.4 Derivation of the weak formulation of the BVP

In section 2.6 some intermediate steps of the derivation of the bilinear form (2.90) are left out. For the sake of completeness these are summarized here. Starting from (2.79), stating

$$\text{div } \boldsymbol{\sigma} + \rho \mathbf{b} = \mathbf{0} \quad (\text{A.51})$$

and multiplying it with a so-called virtual displacement $\boldsymbol{\eta} \in \mathcal{V}$ and integrat-

ing the equation over Ω leads to

$$g(\mathbf{u}, \boldsymbol{\eta}) = \int_{\Omega} (\operatorname{div} \boldsymbol{\sigma}) \cdot \boldsymbol{\eta} \, dx + \int_{\Omega} \rho \mathbf{b} \cdot \boldsymbol{\eta} \, dx = 0. \quad (\text{A.52})$$

With the help of the divergence theorem (see for example [Bronstein et al., 2001]) $g(\mathbf{u}, \boldsymbol{\eta})$ can be transformed to

$$g(\mathbf{u}, \boldsymbol{\eta}) = \int_{\partial\Omega} (\boldsymbol{\sigma} \cdot \mathbf{n}) \cdot \boldsymbol{\eta} \, dx - \int_{\Omega} \boldsymbol{\sigma} : \operatorname{grad} \boldsymbol{\eta} \, dx + \int_{\Omega} \rho \mathbf{b} \cdot \boldsymbol{\eta} \, dx. \quad (\text{A.53})$$

As $\boldsymbol{\eta} = \mathbf{0}$ on $\partial\Omega^u$, (A.53) can be simplified further to

$$g(\mathbf{u}, \boldsymbol{\eta}) = \int_{\partial\Omega^t} (\boldsymbol{\sigma} \cdot \mathbf{n}) \cdot \boldsymbol{\eta} \, dx - \int_{\Omega} \boldsymbol{\sigma} : \operatorname{grad} \boldsymbol{\eta} \, dx + \int_{\Omega} \rho \mathbf{b} \cdot \boldsymbol{\eta} \, dx. \quad (\text{A.54})$$

Incorporating the traction boundary condition from (2.82) yields

$$g(\mathbf{u}, \boldsymbol{\eta}) = \int_{\partial\Omega^t} \bar{\mathbf{t}} \cdot \boldsymbol{\eta} \, dx - \int_{\Omega} \boldsymbol{\sigma} : \operatorname{grad} \boldsymbol{\eta} \, dx + \int_{\Omega} \rho \mathbf{b} \cdot \boldsymbol{\eta} \, dx. \quad (\text{A.55})$$

Furthermore, due to the symmetry of $\boldsymbol{\sigma}$ in (A.55) the gradient operator can be substituted by its symmetric part

$$\operatorname{grad}_s \boldsymbol{\eta} = \frac{1}{2} (\operatorname{grad} \boldsymbol{\eta} + (\operatorname{grad} \boldsymbol{\eta})^T). \quad (\text{A.56})$$

This yields

$$g(\mathbf{u}, \boldsymbol{\eta}) = - \underbrace{\int_{\Omega} \boldsymbol{\sigma} : \operatorname{grad}_s \boldsymbol{\eta} \, dx}_{=a(\mathbf{u}, \boldsymbol{\eta})} + \underbrace{\int_{\partial\Omega^t} \bar{\mathbf{t}} \cdot \boldsymbol{\eta} \, dx + \int_{\Omega} \rho \mathbf{b} \cdot \boldsymbol{\eta} \, dx}_{f(\boldsymbol{\eta})} = 0, \quad (\text{A.57})$$

and herewith the weak form (2.90), which is repeated here

$$a(\mathbf{u}, \boldsymbol{\eta}) = f(\boldsymbol{\eta}), \quad \forall \boldsymbol{\eta} \in \mathcal{V}_t. \quad (\text{A.58})$$

A.4 Parameters used for mesh smoothing

Without further discussion the parameters used for the mesh smoothing algorithm of [Vartziotis et al., 2009] are listed here. The notation in this section is similar to the one in [Vartziotis et al., 2009] and similarities to the notation of this work are ignored. For the simultaneous mesh regularization algorithm, the isovolumetric substep approach from [Vartziotis et al., 2009] is used. The values used for the other parameters can be found in table A.1.

| parameter description | symbol | value |
|---|---------------------------------|-----------|
| minimal scaling factor | σ_{\min} | 0.05 |
| maximal scaling factor | σ_{\max} | 0.1 |
| relaxiation factor | ρ | 0.4 |
| weighting factor exponent | η | 2 |
| average mesh quality stopping criterion | ε_q | 0.95 |
| no change stopping criterion | $\sum_{i=1}^{n_p} p'_i - p_i $ | 10^{-8} |

Table A.1: Parameter description for simultaneous mesh smoothing algorithm.

Analogously the parameters for the sequential mesh regularization algorithm introduced in [Vartziotis et al., 2009] are specified in table A.2.

| parameter description | symbol | value |
|----------------------------------|-----------------|-------|
| minimal scaling factor | σ_{\min} | 0.05 |
| maximal scaling factor | σ_{\max} | 0.1 |
| relaxiation factor | ρ | 0.3 |
| maximal number of iterations | | 100 |
| number of elements per iteration | | 3 |

Table A.2: Parameter description for sequential mesh smoothing algorithm.

List of Symbols

| | |
|------------------------------------|---|
| A | Cross section area. 39 |
| A | Parameter describing the width of a glue joint. 88 |
| \mathbf{a}_i | Enrichment solution value corresponding to node i . 30 |
| α | Material parameter thermal expansion coefficient. 11 |
| $\boldsymbol{\alpha}$ | Multi-index. 113 |
| \cup | Assembly operator. 29 |
| $a(\mathbf{u}, \boldsymbol{\eta})$ | Bilinear form used in weak form of boundary value problem. 23 |
| \mathbf{B} | Gradient matrix of shape functions. 28 |
| B | Parameter describing the depth of a glue joint. 88 |
| \mathbf{b} | Vector-valued volume forces. 20 |
| $C_0^\infty(\Omega)$ | Function space of functions that are infinitely many times continuously differentiable with compact support in Ω . 113 |
| $\boldsymbol{\chi}$ | Internal variables in elastoplastic material model. 12 |
| : | Double contraction of tensors. 114 |
| \cdot | Single contraction of tensors. 114 |
| \mathbb{C} | Fourth order elasticity tensor of a material. 10 |
| $\underline{\mathbb{C}}$ | VOIGT notation of material stiffness matrix or material stiffness tangent modulus \mathbb{C} . 27 |
| d | Parameter describing the thickness of a glue joint. 88 |
| dA | Area segment in the reference configuration. 8 |
| da | Area segment in the current configuration. 8 |
| δ_{ij} | KRONECKER delta with $\delta_{ij} = 1$ if $i = j$ and $\delta_{ij} = 0$ if $i \neq j$. 11 |
| \det | Determinant operator. 9 |
| dev | Deviator operator. 13 |

| | |
|--|--|
| Δa | Increment of the bilinear form a . 29 |
| \mathbf{d}^h | Solution vector containing all unknowns. 34 |
| \mathbf{d}_e^h | Vector containing the unknowns corresponding to element e . 34 |
| $\partial\Omega$ | Boundary of Ω . 20 |
| $\partial\Omega^t$ | Boundary of Ω with a surface traction load specified. 22 |
| $\partial\Omega^u$ | Boundary of Ω with a displacement load specified. 22 |
| $\Delta\mathbf{u}$ | Increment of the displacement vector \mathbf{u} . 29 |
| dV | Volume segment in the reference configuration. 7 |
| dv | Volume segment in the current configuration. 7 |
| $d\mathbf{X}$ | Line segment in the reference configuration. 7 |
| $d\mathbf{x}$ | Line segment in the current configuration. 7 |
| ∂_x | Partial derivative in direction of component x . 28 |
| \otimes | Dyadic product. 7 |
| E | Material parameter YOUNG'S modulus. 11 |
| $\{\mathbf{E}_A\}_{A=1,\dots,3}$ | Basis for the reference configuration. 7 |
| $\{\mathbf{e}_i\}_{i=1\dots 3}$ | Basis for the current configuration. 7 |
| E_{concrete} | Material parameter YOUNG'S modulus of the concrete shell. 89 |
| E_{joint} | Material parameter YOUNG'S modulus of the glue joint. 89 |
| $\boldsymbol{\varepsilon}^{\text{el}}$ | Elastic part of strain tensor. 11 |
| $\boldsymbol{\varepsilon}^{\text{pl}}$ | Plastic part of strain tensor. 12 |
| $\boldsymbol{\varepsilon}$ | Linearized strain tensor. 9 |
| $\boldsymbol{\varepsilon}^{\text{th}}$ | Thermal part of strain tensor. 14 |
| $\underline{\boldsymbol{\varepsilon}}$ | VOIGT notation of strain tensor $\boldsymbol{\varepsilon}$. 27 |
| $\boldsymbol{\varepsilon}^*$ | Radial component of strain tensor. 59 |
| $\boldsymbol{\varepsilon}^*$ | Equivalent eigenstrain. 58 |
| $\boldsymbol{\eta}$ | Test function for weak formulation. 23 |
| \mathbf{E} | GREEN-LAGRANGE strain tensor. 8 |
| \mathbf{F} | Scalar-valued enrichment function. 30 |
| f.a.a. | for almost all. 18 |
| F | A specific point force. 39 |

| | |
|------------------------------------|--|
| $f(\boldsymbol{\eta})$ | Linearform used in weak form of boundary value problem. 23 |
| \mathbf{F} | Right hand side of weak form. 30 |
| \mathbf{F} | Deformation gradient. 7 |
| f | Scalar-valued yield function describing type of deformation for elastoplastic material behavior. 12 |
| Γ | Interface between two materials within Ω . 15 |
| grad | Gradient operator with respect to the current configuration. 9 |
| ∇ | Symbol for gradient operator. 18 |
| grad_s | Symmetric gradient operator. 24 |
| $g(\mathbf{u}, \boldsymbol{\eta})$ | Function describing the weak form of boundary value problem. 23 |
| \tilde{h} | Model parameter in the elastoplastic material model. 14 |
| $H^1(\Omega)$ | SOBOLEV space defined on Ω . 113 |
| h | Mesh parameter, describing a typical length unit of the mesh. 25 |
| \mathbf{I} | Second order identity tensor. 8 |
| J_2 | Second invariant of stress deviator. 63 |
| J | Jacobian determinant of deformation gradient \mathbf{F} . 7 |
| J^e | Fundamental determinant of the coordinate transformation from a given element e to Ω^e . 29 |
| $[[\cdot]]$ | Jump operator. 15 |
| \mathbf{K} | Global stiffness matrix. 30 |
| K | Scalar-valued hardening function in the elastoplastic material model. 13 |
| κ | Conditioning number of a matrix. 51 |
| K_I | Material parameter bulk modulus of material I. 58 |
| \mathcal{K} | Curvature. 18 |

| | |
|----------------------------|---|
| \mathbf{L} | Vector-valued measure for the momentum. 20 |
| $L^2(\Omega)$ | Function space of square integrable functions defined on Ω . 112 |
| λ_1 | Eigenvalue number one of global stiffness matrix. 47 |
| λ | LAMÉ constant λ . 10 |
| Δ | Laplace operator. 19 |
| ϕ | Scalar-valued level set function without further specifications. 17 |
| Φ | Scalar-valued signed distance level set function. 18 |
| \wedge | Logical “and”. 17 |
| m | Model parameter in the elastoplastic material model. 14 |
| \mathbf{m} | Direction for moving nodes algorithm. 72 |
| n_d | Total number of degrees of freedom. 26 |
| n_e | Number of elements in the finite element mesh. 25 |
| $\bar{\mathcal{N}}_h^*$ | Index set of all enriched nodes in the finite element mesh. 30 |
| $\bar{\mathcal{N}}_h$ | Index set of nodes in $\bar{\Sigma}_h$. 25 |
| $N_i(\mathbf{x})$ | Scalar-valued shape function defined on the reference element, corresponding to node i of the reference element. 29 |
| n_{it} | Multiple iteration parameter for moving nodes algorithm. 73 |
| \mathbf{N} | Normal vector of an area element in reference configuration. 8 |
| \mathbf{n} | Normal vector of an area element in current configuration. 8 |
| ν | Material parameter POISSON’S ratio. 11 |
| Ω | Domain of reference configuration. 5 |
| $\bar{\Omega}$ | Closure of Ω . 26 |
| Ω_{concrete} | Volume of concrete shell excluding the glue joint. 91 |
| Ω^e | Single element of finite element mesh. 25 |
| Ω^h | Discretized domain Ω . 25 |

| | |
|--------------------------|--|
| Ω_I | One of usually two parts of Ω , typically denoting the material of some inclusion. 15 |
| Ω_{joint} | Volume of glue joint excluding the rest of the concrete shell. 91 |
| Ω_M | One of usually two parts of Ω , typically denoting the matrix material. 16 |
| Ω^{ref} | Reference element. 28 |
| \mathcal{O} | LANDAU symbol describing the mathematical order of approximation. 9 |
| $\tilde{\varphi}^{i,h}$ | Shape function corresponding to enriched degree of freedom for enriched node \mathbf{x}^i . 33 |
| $\varphi^{j,h}$ | Piecewise linear function on \mathcal{T}_h with $\varphi^{j,h}(\mathbf{x}^i) = \delta_{ij}$. 26 |
| $\varphi^{j,h}$ | Element of space \mathcal{V}^h . 26 |
| $\varphi(\Omega)$ | Motion of the body Ω in \mathbb{R}^3 , is called current configuration. 5 |
| $\varphi(\mathbf{X})$ | Position of point \mathbf{X} in the current configuration. 5 |
| $\varphi(\mathbf{X}, t)$ | Position of point \mathbf{X} in the current configuration at time t . 6 |
| $\varphi_t(\Omega)$ | Motion of the body Ω in \mathbb{R}^3 , is called current configuration at time t . 6 |
| π | Accumulated plastic strain. 13 |
| $q(\Omega)$ | Quality measure in glue joint example for volume Ω . 90 |
| ρ | Local density in the current configuration. 19 |
| ρ_0 | Local density in the reference configuration. 19 |
| $\mathbf{R}(t)$ | Rotation tensor depending on time t . 114 |
| \mathbb{R} | Real numbers. 5 |
| \mathbb{R}^3 | Three-dimensional Euclidean space. 5 |
| \mathcal{S} | Derivative operator for shape function matrix. 28 |
| s | Scalar-valued parameter typically describing the position of a discontinuity. 39 |
| \emptyset | Empty set. 17 |
| \cap | Intersection of two sets. 17 |

| | |
|-------------------------------|---|
| \cup | Union of two sets. 17 |
| \mathbf{s}^h | Part of decomposition of \mathbf{u}^h into $\mathcal{S}_t^h + \mathcal{V}_t^h$. 26 |
| $\text{shift}(i, j)$ | Shifting operator for VOIGT notation. 27 |
| $\sigma_{1,\max}(\mathbf{x})$ | Maximal principal stress at point \mathbf{x} . 90 |
| $\bar{\Sigma}_h$ | Set of all vertices of \mathcal{T}_h . 25 |
| σ_v^{\max} | Maximal VON MISES equivalent stress value. 83 |
| $\sigma_{N,\text{concrete}}$ | Reference stress in concrete shell. 89 |
| $\sigma_{N,\text{joint}}$ | Reference stress in glue joint. 89 |
| $\sigma_{N,\Omega}$ | Reference stress in volume Ω . 90 |
| $\underline{\sigma}$ | VOIGT notation of stress tensor σ . 27 |
| σ_y | Yield strength. 14 |
| sign | Sign function. 32 |
| s_0 | Shiftingfactor for moving nodes algorithm. 73 |
| σ | Cauchy stress tensor. 10 |
| $\mathcal{S}_t^h(\mathbf{x})$ | Discretized function space for displacement solution at time t for a given point $\mathbf{x} \in \Omega$. 26 |
| \mathcal{S}_t | Function space for displacement solution at time t . 23, 24 |
| \subset | Subset. 17 |
| \mathbf{t} | Surface traction vector. 20 |
| \mathcal{T}_h | Quasi uniform triangulation of Ω . 25 |
| $\Delta\vartheta$ | Change of temperature. 11 |
| t_0 | Thresholdparameter for moving nodes algorithm. 73 |
| $\bar{\mathbf{t}}$ | Surface traction load. 21 |
| tr | Trace operator. 9 |
| \mathbf{u}_0 | Initial displacement conditions. 21 |
| \mathbf{u}^h | Projection of solution \mathbf{u} onto $\mathcal{S}_t^h(\mathbf{x})$. 26 |
| $u_k^h(\mathbf{x})$ | Component k of discretized displacement solution. 26 |
| \mathbf{u}_i | Displacement solution value corresponding to node i . 30 |
| $\mathbf{u}(\mathbf{X}, t)$ | Displacement vector at position $\mathbf{x}(\mathbf{X}, t)$ in current configuration. 6 |
| $\bar{\mathbf{u}}$ | Prescribed displacement. 21 |
| u_r | Radial component of displacement. 59 |

| | |
|--------------------------------|---|
| \mathbf{v} | Vector-valued local velocity. 20 |
| \mathcal{V}^h | Finite dimensional subspace of solution space \mathcal{V} . 25 |
| \mathbf{v}^h | Part of decomposition of \mathbf{u}^h into $\mathcal{S}_t^h + \mathcal{V}_t^h$. 26 |
| $\mathbf{v}_T(t)$ | Translation depending on time t . 114 |
| $\mathcal{V}_t^h(\mathbf{x})$ | Discretized function space of admissible test functions. 26 |
| \mathcal{V}_t | Function space of admissible test functions. 23 |
| \mathbf{x} | Parameter for a position vector in the current configuration. 5 |
| \mathbf{x}^i | The i^{th} node in the finite element mesh. 26 |
| $\boldsymbol{\xi}(\mathbf{x})$ | Transformation to the reference element. 33 |
| \mathbf{X} | Reference position of a material point in the body (material coordinate). 5 |

Bibliography

- Alt, H., 2007. *Lineare Funktionalanalysis*. Springer, Berlin.
- Altenbach, J., Altenbach, H., Betten, H., 1996. Einführung in die Kontinuumsmechanik. *ZAMM-Zeitschrift für Angewandte Mathematik und Mechanik* 76 (10), 34.
- Antman, S., 2005. *Nonlinear problems of elasticity*. Vol. 107. Springer, New York.
- Axelsson, R., Barker, V., 1984. *Finite Element Solution of Boundary Value Problems*. Academic Press, London.
- Babuska, I., Melenk, J., 1995. The partition of unity finite element method. Tech. rep., DTIC Document.
- Béchet, E., Minnebo, H., Moës, N., Burgardt, B., 2005. Improved implementation and robustness study of the X-FEM for stress analysis around cracks. *International Journal for Numerical Methods in Engineering* 64 (8), 1033–1056.
- Becker, E., Bürger, W., 1975. *Kontinuumsmechanik: eine Einführung in die Grundlagen und einfachen Anwendungen*. Vol. 20. Teubner, Stuttgart.
- Becker, W., Gross, D., 2002. *Mechanik elastischer Körper und Strukturen*. Springer, Berlin.
- Belytschko, T., Black, T., 1999. Elastic crack growth in finite elements with minimal remeshing. *International Journal for Numerical Methods in Engineering* 45 (5), 601–620.
- Belytschko, T., Liu, W., Moran, B., 2000. *Nonlinear finite elements for continua and structures*. Chichester 16, 650.
- Belytschko, T., Moës, N., Usui, S., Parimi, C., 2001. Arbitrary discontinuities in finite elements. *International Journal for Numerical Methods in Engineering* 50 (4), 993–1013.
- Bordas, S., Nguyen, P., Dunant, C., Guidoum, A., Nguyen-Dang, H., 2007. An extended finite element library. *International Journal for Numerical Methods in Engineering* 71 (6), 703–732.

- Bordas, S., Rabczuk, T., Hung, N.-X., Nguyen, P., Natarajan, S., Bog, T., Quan, D., Hiep, N., 2010. Strain smoothing in fem and xfem. *Computers & structures* 88 (23), 1419–1443.
- Braess, D., 2007. *Finite Elemente*. Springer.
- Brenner, S., Scott, L., 2008. *The mathematical theory of finite element methods*. Vol. 15. Springer, New York.
- Bridgman, P., 1970. *The physics of high pressure*. Courier Dover Publications, New York.
- Bronstein, I., Semendjajew, K., Musiol, G., Mühlig, H., 2001. *Taschenbuch der Mathematik*. Harri Deutsch, Frankfurt.
- Chadwick, P., 1999. *Continuum mechanics: Concise theory and problems*. Courier Dover Publications, New York.
- Chawla, K., Chawla, N., 2004. *Metal-Matrix Composites*. John Wiley & Sons, Inc.
- Chessa, J., Belytschko, T., 2003. An extended finite element method for two-phase fluids. *Journal of Applied Mechanics* 70 (1), 10–17.
- Chessa, J., Smolinski, P., Belytschko, T., 2002. The extended finite element method (xfem) for solidification problems. *International Journal for Numerical Methods in Engineering* 53 (8), 1959–1977.
- Dolbow, J., 1999. *An extended finite element method with discontinuous enrichment for applied mechanics*. Northwestern university, Evanston.
- Duddu, R., Bordas, S., Chopp, D., Moran, B., 2008. A combined extended finite element and level set method for biofilm growth. *International Journal for Numerical Methods in Engineering* 74 (5), 848–870.
- Ern, A., Guermond, J.-L., 2004. *Theory and practice of finite elements*. Vol. 159. Springer, New York.
- Eshelby, J., 1957. The determination of the elastic field of an ellipsoidal inclusion, and related problems. *Proceedings of the Royal Society of London. Series A. Mathematical and Physical Sciences* 241 (1226), 376–396.
- Farhat, C., Roux, F.-X., 1991. A method of finite element tearing and interconnecting and its parallel solution algorithm. *International Journal for Numerical Methods in Engineering* 32 (6), 1205–1227.

-
- FeelMath, 2014. Finite elements for ELastic MATerials and homogenization.
URL <http://www.itwm.fraunhofer.de/en/departments/flow-and-material-simulation/mechanics-of-materials/feelmath/>
- Feynman, R., Leighton, R., Sands, M., 1963. The Feynman Lectures on Physics, Volume I: Mainly mechanics, radiation, and Heat. Vol. 1. Addison-Wesley.
- Fries, T., Belytschko, T., 2010. The extended/generalized finite element method: An overview of the method and its applications. *International Journal for Numerical Methods in Engineering* 84 (3), 253–304.
- Fries, T.-P., 2008. A corrected XFEM approximation without problems in blending elements. *International Journal for Numerical Methods in Engineering* 75 (5), 503–532.
- Granta Design Limited, 2009. CES EduPack 2009 software.
URL <http://www.grantadesign.com/education/overview.htm>
- Groß, S., Reusken, A., 2007. An extended pressure finite element space for two-phase incompressible flows with surface tension. *Journal of Computational Physics* 224 (1), 40–58.
- Guldberg, R., Hollister, S., Charras, G., 1998. The accuracy of digital image-based finite element models. *Journal of Biomechanical Engineering* 120 (2), 289.
- Gurtin, M., 1982. An introduction to continuum mechanics. Vol. 158. Academic press.
- Han, W., Reddy, B., 2013. Plasticity. Vol. 9. Springer, Berlin.
- Hoffmann, S., 2012. Computational Homogenization of Short Fiber Reinforced Thermoplastic Materials. Techn. Univ. Kaiserslautern, Lehrstuhl für Techn. Mechanik, Kaiserslautern.
- Holzapfel, G., 2000. Nonlinear solid mechanics: A continuum approach for engineering. John Wiley & Sons Ltd., Chichester.
- Hughes, T., 1987. The finite element method: linear static and dynamic finite element analysis. Prentice-Hall, Inc., Englewood.

- Legay, A., Chessa, J., Belytschko, T., 2006. An eulerian–lagrangian method for fluid–structure interaction based on level sets. *Computer Methods in Applied Mechanics and Engineering* 195 (17), 2070–2087.
- Liu, X., Xiao, Q., Karihaloo, B., 2004. XFEM for direct evaluation of mixed mode sifs in homogeneous and bi-materials. *International Journal for Numerical Methods in Engineering* 59 (8), 1103–1118.
- Löhnert, S., 2014. A stabilization technique for the regularization of nearly singular extended finite elements. *Computational Mechanics*, 1–11.
- Malvern, L., 1969. *Introduction to the Mechanics of a Continuous Medium*. No. Monograph.
- Marsden, J., Hughes, T., 1983. *Mathematical foundations of elasticity*. Courier Dover Publications, New York.
- Materion Aerospace Metal Composites Limited, Nov. 2013. Aerospace metal composites.
URL <http://www.materion.com/aerospacemetalcomposites>
- Melenk, J., Babuška, I., 1996. The partition of unity finite element method: basic theory and applications. *Computer methods in applied mechanics and engineering* 139 (1), 289–314.
- Menk, A., 2011. Simulation of complex microstructural geometries using X-FEM and the application to solder joint lifetime prediction. Ph.D. thesis, University of Glasgow.
- Menk, A., Bordas, S., 2011. A robust preconditioning technique for the extended finite element method. *International Journal for Numerical Methods in Engineering* 85 (13), 1609–1632.
- Moës, N., Cloirec, M., Cartraud, P., Remacle, J., 2003. A computational approach to handle complex microstructure geometries. *Computer Methods in Applied Mechanics and Engineering* 192 (28), 3163–3177.
- Moës, N., Dolbow, J., Belytschko, T., 1999. A finite element method for crack growth without remeshing. *International Journal for Numerical Methods in Engineering* 46 (1), 131–150.
- Mura, T., 1987. *Micromechanics of defects in solids*. Vol. 3. Kluwer Academic Publishers, Dordrecht.

-
- Ogden, R., 1997. Non-linear elastic deformations. Courier Dover Publications.
- Osher, S., Fedkiw, R., 2003. Level set methods and dynamic implicit surfaces. Vol. 153. Springer, New York.
- Osher, S., Sethian, J., 1988. Fronts propagating with curvature-dependent speed: Algorithms based on Hamilton-Jacobi formulations. *Journal of Computational Physics* 79 (1), 12–49.
- Oster, S., Kohlmeyer, C., Shklyar, I., Andrä, H., 2012. Adhesive joints for structural elements of high performance concrete (HPC). 9th fib International PhD Symposium in Civil Engineering, Karlsruhe Institute of Technology (KIT), 335–340.
- Rutka, V., Wiegmann, A., Andrä, H., 2006. EJIIM for calculation of effective elastic moduli in 3d linear elasticity. Tech. Rep. 93, Berichte des Fraunhofer ITWM 93.
- Saint Raymond, X., 1991. Elementary introduction to the theory of pseudodifferential operators. Vol. 3. CRC Press, Inc., Boca Raton.
- Sato, N., Kurauchi, T., Sato, S., Kamigaito, O., 1991. Microfailure behaviour of randomly dispersed short fibre reinforced thermoplastic composites obtained by direct sem observation. *Journal of materials science* 26 (14), 3891–3898.
- Schnell, J., Kohlmeyer, C., Bayer, D., Müller, F., 2013. Werkstoffgerechtes konstruieren mit hochleistungsbetonen. *Beton-und Stahlbetonbau* 108 (6), 404–413.
- Schrade, D., 2011. Microstructural modeling of ferroelectric material behavior. Techn. Univ. Kaiserslautern, Lehrstuhl für Techn. Mechanik, Kaiserslautern.
- Schwartz, L., 1966. *Théorie des distributions*. Actualités Scientifiques et Industrielles, Institut de Mathématique, Université de Strasbourg 1, 2.
- Sethian, J., 1999. Level set methods and fast marching methods: Evolving interfaces in computational geometry, fluid mechanics, computer vision, and materials science. Vol. 3. Cambridge University Press, Cambridge.
- Simo, J., Hughes, T., 1998. Computational inelasticity. Springer, New York.

- Simo, J., Taylor, R., 1986. A return mapping algorithm for plane stress elastoplasticity. *International Journal for Numerical Methods in Engineering* 22 (3), 649–670.
- Simone, A., Duarte, C., Van der Giessen, E., 2006. A generalized finite element method for polycrystals with discontinuous grain boundaries. *International Journal for Numerical Methods in Engineering* 67 (8), 1122–1145.
- Stolarska, M., Chopp, D., Moës, N., Belytschko, T., 2001. Modelling crack growth by level sets in the extended finite element method. *International Journal for Numerical Methods in Engineering* 51 (8), 943–960.
- Sukumar, N., Chopp, D., Moës, N., Belytschko, T., 2001. Modeling holes and inclusions by level sets in the extended finite-element method. *Computer methods in applied mechanics and engineering* 190 (46), 6183–6200.
- Sukumar, N., Moës, N., Moran, B., Belytschko, T., 2000. Extended finite element method for three-dimensional crack modelling. *International Journal for Numerical Methods in Engineering* 48 (11), 1549–1570.
- Truesdell, C., Noll, W., 2004. *The non-linear field theories of mechanics*. Springer, Berlin, Heidelberg.
- Truesdell, C., Toupin, R., 1960. *The classical field theories*. Springer, Berlin, Heidelberg.
- Vartziotis, D., Wipper, J., Schwald, B., 2009. The geometric element transformation method for tetrahedral mesh smoothing. *Computer Methods in Applied Mechanics and Engineering* 199 (1), 169–182.
- Ventura, G., 2006. On the elimination of quadrature subcells for discontinuous functions in the extended finite-element method. *International Journal for Numerical Methods in Engineering* 66 (5), 761–795.
- Vigneron, L., Verly, J., Warfield, S., 2004. On extended finite element method (xfem) for modelling of organ deformations associated with surgical cuts. In: *Medical Simulation*. Springer, pp. 134–143.
- Vuong, A.-V., Simeon, B., 2012. *Adaptive Hierarchical Isogeometric Finite Element Methods*. Springer, Wiesbaden.
- Wang, C.-C., Truesdell, C., 1973. *Introduction to rational elasticity*. Vol. 1. Springer.

- Wilmanski, K., 2008. Continuum Thermodynamics. Vol. 1. World Scientific, Singapore.
- Wriggers, P., 2001. Nichtlineare Finite-Element-Methoden. Springer, Berlin.
- Zangmeister, T., Andrä, H., Müller, R., 2013. Comparison of XFEM and voxelbased FEM for the approximation of discontinuous stress and strain at material interfaces. *Scientific Journal for Fundamentals and Applications of Engineering Mechanics* 33 (2), 131–141.
- Zhang, X., Zhang, Q., Zangmeister, T., Xiao, B., Andrä, H., Ma, Z., 2014. A three-dimensional realistic microstructure model of particle reinforced metal matrix composites - submitted september 2013. *Modelling and Simulation in Materials Science and Engineering* 22 (3), 035010.
- Zienkiewicz, O., Taylor, R., 2000. The Finite Element Method, 5th Edition. Vol. 1. Butterworth-Heinemann, Oxford.
- Zilian, A., Legay, A., 2008. The enriched space–time finite element method (est) for simultaneous solution of fluid–structure interaction. *International Journal for Numerical Methods in Engineering* 75 (3), 305–334.

Lebenslauf

Tobias Zangmeister

1989 – 1992 Grundschule Joseph-Heckler-Schule in Bensheim

1992 – 1997 Goethe Gymnasium Bensheim

1997 – 2001 Altes Kurfürstliches Gymnasium Bensheim

Schulabschluss Abitur

2001 – 2002 Zivildienst (Sozialstation Pusteblume Bensheim)

2002 – 2005 Studium Mathematical Engineering Bachelor an der Technischen Universität Carolo-Wilhelmina zu Braunschweig

Studienabschluss Bachelor of Science

2005 – 2007 Studium Mathematical Engineering Master an der Technischen Universität Carolo-Wilhelmina zu Braunschweig

Studienabschluss Master of Science

2006 – 2008 Wissenschaftlicher Mitarbeiter an der Technischen Universität Carolo-Wilhelmina zu Braunschweig

2008 – 2012 Promotionsstudent am Fraunhofer-Institut für Technologie und Wirtschaftsmathematik

2012 – 2013 Wissenschaftlicher Mitarbeiter an der Technischen Universität Kaiserslautern